Molecular Beam Epitaxy Growth of Indium Nitride and Indium Gallium Nitride Materials for Photovoltaic Applications

A Ph.D. Dissertation
Presented to
The Academic Faculty

by

Elaissa Trybus

In Partial Fulfillment
of the Requirements for the Degree
Doctor of Philosophy in the
School of Electrical and Computer Engineering

Georgia Institute of Technology
May 2009

Molecular Beam Epitaxy Growth of Indium Nitride and Indium Gallium Nitride Materials for Photovoltaic Applications

Dr. W. Alan Doolittle
School of Electrical and Computer Engineering
Georgia Institute of Technology

Dr. Ian Ferguson
School of Electrical and Computer Engineering
Georgia Institute of Technology

Dr. Ajeet Rohatgi
School of Electrical and Computer Engineering
Georgia Institute of Technology

Dr. Shyh-Chiang Shen
School of Electrical and Computer Engineering
Georgia Institute of Technology

Dr. Samuel Graham
School of Mechanical Engineering
Georgia Institute of Technology

Date Approved: March 2009

To my parents. This would not have been possible without your support.

Go confidently in the direction of your dreams.
Live the life you've imagined.

-Henry David Thoreau

ACKNOWLEDGEMENTS

My interest in math and science was fostered by my Dad, the Physicist. I would not be an Electrical Engineer (AKA an applied Physicist) without his instruction and support. I thank both my parents for their never ending love and support.

My advisor, Dr. W. Alan Doolittle has been very supportive, patient, and provided me with endless knowledge. I am extremely grateful to him. Additionally, the members of his research group have been invaluable to me in friendship and with my education: Walter Henderson, David Pritchett, Alex Carver, Daniel Billingsley, Laws Calley, Michael Moseley, Kyoung Keun Lee, Ann Trippe, Dr. Gon Namkoong, and Dr. Shawn Burnham. I also thank Dr. Doolittle's Accountant Mary Render and Administrative Assistant Linda Newton.

I would like to acknowledge the support and guidance received from my thesis committee and the friendship from their research groups: Dr. Ian Ferguson, Dr. Shyh-Chiang Shen, Dr. Ajeet Rohatgi, and Dr. Samuel Graham. In addition, I would like to thank Dr. Christiana Honsberg of the University of Delaware and her research group, in particular Dr. Omkar Jani and Balakrishnam Jampana. The MiRC staff has been very helpful and accommodating with my research, specifically Gary Spinner, Charlie Suh, Vinh Nguyen, and Dean Sutter.

Throughout my graduate studies at Georgia Tech I have had the support of many friends and family: my sister Brittany, my best friends since high school Emily Gaffney, Emm Starnes, and Keely Hogan-Braker, my extended family of grandparents, aunts, uncles, and cousins – The Trybus, Burton, and Korenkiewicz families, the SwimAtlanta

family at Georgia Tech - Doug Gjersten and Sergey Useinov, Bill and Jenny Eversole, Gus who has been there everyday, Arti who always makes me laugh, and the Hardy family, especially George. Thank-you.

This work was supported by the Defense Advance Research Project Agency, monitored by Dr. Doug Kirpatrick, Dr. Brian Pierce, and Dr. Stefanie Tompkins under the University of Delaware-DuPont Very High Efficiency Solar Cell program monitored by Dr. Dan Laubacher and Dr. Allen Barnett.

TABLE OF CONTENTS

LIST OF TABLES

LIST OF FIGURES

SUMMARY

The objective of the proposed research is to establish the technology for material growth by molecular beam epitaxy (MBE) and fabrication of indium gallium nitride/gallium nitride ($In_xGa_{1-x}N$/GaN) heterojunction solar cells. $In_xGa_{1-x}N$ solar cells have the potential to span 90% of the solar spectrum, however there has been no success with high indium (In) incorporation and only limited success with low In incorporation $In_xGa_{1-x}N$. Therefore, this present work focuses on 15 - 30% In incorporation leading to a bandgap value of 2.3 - 2.8 eV. This work will exploit the revision of the indium nitride (InN) bandgap value of 0.68 eV, which expands the range of the optical emission of nitride-based devices from ultraviolet to near infrared regions, by developing transparent $In_xGa_{1-x}N$ solar cells outside the visible spectrum. Photovoltaic devices with a bandgap greater than 2.0 eV are attractive because over half the available power in the solar spectrum is above the photon energy of 2.0 eV. The ability of $In_xGa_{1-x}N$ materials to optimally span the solar spectrum offers a tantalizing solution for high-efficiency photovoltaics.

This work presents results confirming the revised bandgap of InN grown on germanium (Ge) substrates and the effects of oxygen contamination on the bandgap. This research adds to the historical discussion of the bandgap value of InN.

Using the metal modulated epitaxy (MME) technique in a new, ultra-clean refurbished MBE system, an innovative growth regime is established where In and Ga phase separation is diminished by increasing the growth rate for $In_xGa_{1-x}N$. The MME technique modulates the metal shutters with a fixed duty cycle while maintaining a

constant nitrogen flux and proves effective for improving crystal quality and p-type doping.

$In_xGa_{1-x}N$/GaN heterojunction solar cells require p-type doping to create the p-n sub-cell collecting junction, which facilitates current collection through the electrostatic field created by spatially separated ionized donors and acceptors. Magnesium (Mg) has been proven to be the most successful p-type dopant. We demonstrate the ability to repeatedly grow high hole concentration Mg-doped GaN films using the MME technique. The highest hole concentration obtained is equal to 4.26×10^{19} cm^{-3}, resistivity of 0.5 Ω-cm, and mobility of 0.28 cm^2/V-s. We have achieved hole concentrations significantly higher than recorded in the literature, proving that our growth parameters and the MME technique is feasible, repeatable, and beneficial to p-GaN devices.

The solar cell structures were modeled with software, to design an optimal heterojunction solar cell. Using the modeling results and optimized growth parameters, four solar cell devices were grown, fabricated, and underwent extensive device testing. The device testing determined that there was no photovoltaic response from the devices, resulting from the lack of high doping in the p-GaN emitter.

CHAPTER 1: Introduction

"The conversion of sunlight directly into electricity using the photovoltaic properties of suitable materials is the most elegant energy conversion process," said Hans Joachim Möller [1]. Current technology has proven that solar cells are a viable solution as an alternative energy source. Additionally, the realization that traditional fossil energy resources - coal, oil, and gas - are limited and may contribute to unpredictable, possibly irreversible climate changes in the near future has increased the market for solar cell technology. This work investigates a new material system for second-generation solar cell technology, specifically, the indium gallium nitride ($In_xGa_{1-x}N$) material system grown in an ultra-high vacuum environment by molecular beam epitaxy (MBE). $In_xGa_{1-x}N$ materials are able to span the electromagnetic spectrum from the ultraviolet to near infrared. Nitride based solar cells are alluring because over half the available power in the solar spectrum is above 2.0 eV photon energy. Additionally, given the bandgap limitations of previously available semiconductors, power above 2.0 eV is normally collected in a less than optimally efficient manner.

1.1. Solar Cells

In 1839, Alexandre-Edmond Becquerel first recognized the photovoltaic effect, the ability of certain materials to convert light energy into electrical energy. Becquerel observed that when metal plates immersed in a suitable electrolyte were exposed to sunlight, a small voltage and current were produced [1]. The first large-area solar cell was a piece of selenium semiconductor thinly coated with gold, built by Charles Fritts in

1894 [2]. 1954 welcomed the modern age of solar cell technology with Bell Laboratories discovering that silicon doped with certain impurities was sensitive to light. Research on solar cells continued and in May 1958, Russian Sputnik 3 was the first satellite to use solar arrays.

Since that time, the solar cell community has designated four generations of solar cells. The first-generation solar cells are large-area, single-layer p-n junctions that are predominately made of silicon. The second-generation is based on thin-film semiconductors, that are designed to be high-efficient multiple junction devices. In 2007, King et al. at Spectrolab set the world record for second-generation solar cells with an efficiency of 40.7% on a metamorphic three junction GaInP/GaInAs/Ge device [3]. The GaInP/GaInAs/Ge device is also known at a tandem device, where each material in itself has a p-n junction and is a solar cell. The devices are then connected in series through tunnel junctions to create the metamorphic three junction device. Tunnel junctions will be described in more detail in Chapter 2. The current world record second-generation solar cell is an inverted $Ga_{0.51}In_{0.49}P$ top junction lattice matched to a GaAs substrate, followed by a metamorphic $In_{0.04}Ga_{0.96}As$ middle junction, and a metamorphic $In_{0.37}Ga_{0.63}As$ bottom junction with an efficiency of 40.8% developed at the National Renewable Energy Laboratory (NREL) [4].

Third-generation solar cells do not use a traditional p-n junction to separate photogenerated charge carriers. They consist of photoelectrochemical cells, polymer cells, and nanocrystal solar cells. Fourth-generation solar cells use a composite photovoltaic technology where polymers and nano particles are mixed together to make a single multi-spectrum layer. All of the described generation solar cells are shown in

Figure 1.1, a graph from the NREL depicting the growth of the solar cell research industry and the increase in efficiency of different device technologies.

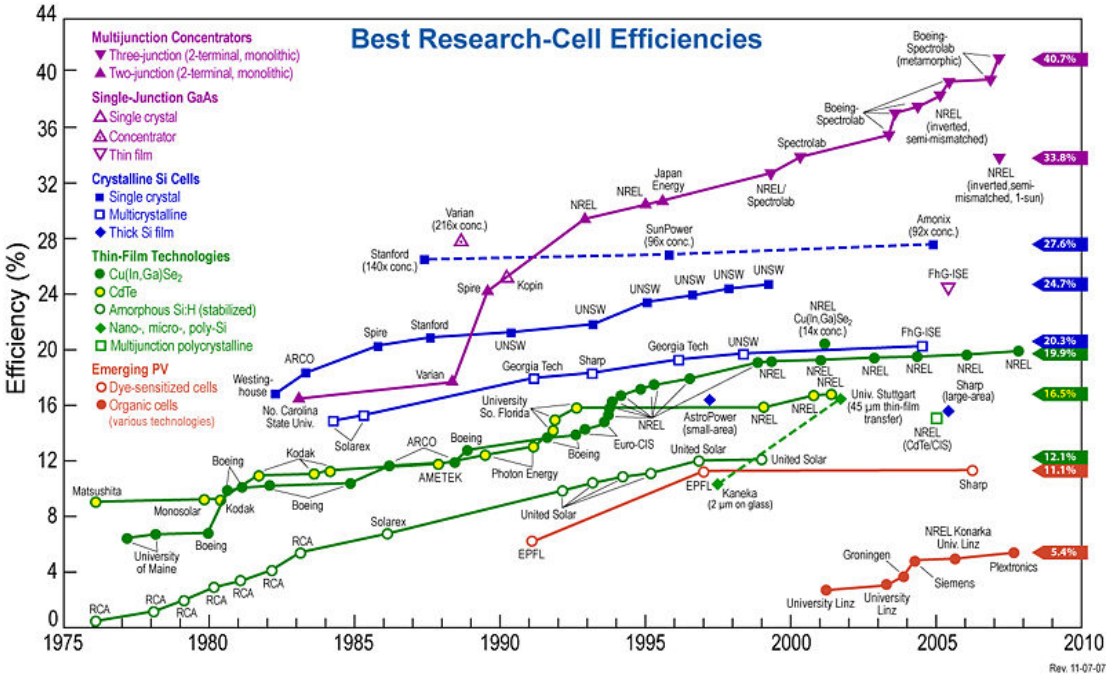

Figure 1.1 – Best research solar cell efficiencies using various technologies, courtesy of L.L. Kazmerski at NREL [5].

The multi-junction concentrator devices have shown a dramatic increase in efficiency compared to other technologies (shown in purple in Figure 1.1). Multi-junction concentrator devices are considered a second-generation technology with devices usually consisting of two ternary lattice matched III-V materials matched to a semiconductor substrate such as Ge or GaAs. These devices are also primarily current matched, which provides another layer of difficulty to the engineering design.

Figure 1.2 is a simplified block diagram of the photovoltaic effect. Incident light on the solar cell is absorbed, excites electrons, which creates electron-hole pairs (EHPs) in the device. The EHPs diffuse (or in some cases drift) into a region having an internal electric field, which separates the carriers, creating output current and voltage.

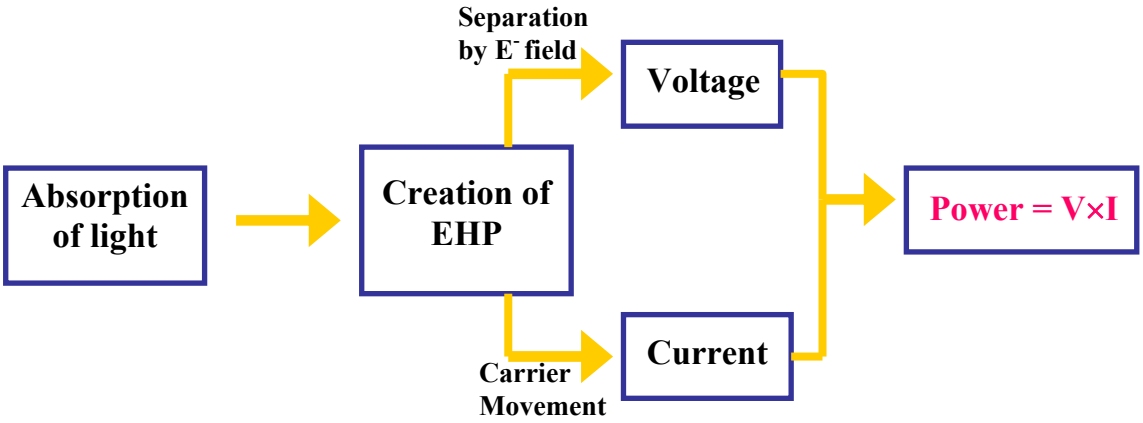

Figure 1.2 – Block diagram of photovoltaic effect, where the solar cell absorbs the sun spectrum, creates electron hole pairs (EHP) which interact with an internal electric field creating voltage and current.

The amount of incident light utilized by the solar cell is based on the semiconductor material's bandgap. Photons with energy less than the bandgap pass through the device, not contributing to the output. Photons with energy equal to the bandgap are absorbed and the EHPs are photogenerated. Lastly, photons with energy much greater than the bandgap are absorbed and the excess energy is lost as heat. Therefore, a small amount of photons contribute to the output of the device. The physics of solar cells is discussed in more detail in Appendix A.

1.1.1. Test Procedures

In 1975, it was decided that a standard test procedure for terrestrial solar cells was necessary. The procedure aimed to provide a common basis for comparing solar cells and provide data for the design of large arrays. The resultant test manual was based on results from workshops held by the National Aeronautics and Space Administration (NASA) and the Energy Research and Development Administration (ERDA). They detailed procedures for obtaining cell and array current-voltage measurements both outdoors in natural sunlight and indoors in simulated sunlight, a description of the

necessary apparatus and equipment, the calibration and use of reference solar cells, some comments relating to concentrator cell measurements, and a terrestrial solar spectrum for use in theoretical calculations [6].

The need for standard test procedures also developed from the non-standard irradiance spectrum of sunlight. Figure 1.3 shows the solar irradiance spectrum above the atmosphere, at sea level, and a blackbody spectrum. The spectral distribution of emitted radiation from the sun can be determined by the temperature of the sun's surface. The wavelength distribution of the sunlight follows approximately the radiation distribution of a blackbody at the temperature of the sun's surface [1]. Light in the visible range, equivalent to ~ 400 – 650 nm (equal to 1.91 – 3.10 eV), has the highest intensity, providing the most available power for a solar cell.

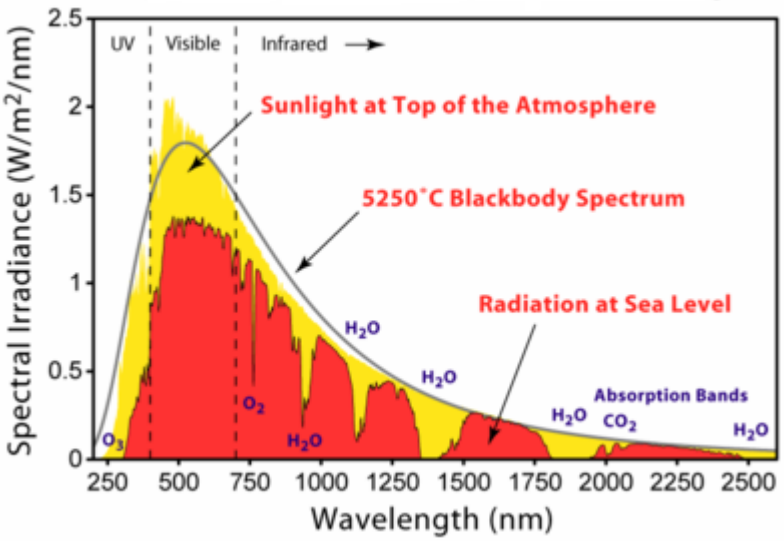

Figure 1.3 – Solar irradiance spectrum above the atmosphere and at the surface [7].

Additionally, standard measurements are complicated by the highly variable degree of attenuation of the radiant power, because of the sun's constant changing position and changing path length through the atmosphere [7]. This constant change has been accounted for by the following: the ratio of the actual path length of the sun to the

minimum path length has been defined when the sun is directly overhead as optical air mass (AM) and the corresponding radiation as air mass one (AM1). Mathematically, AM is defined as

$$AM = \frac{1}{\cos\theta}. \tag{1}$$

θ is the angle of the sun to overhead and is shown in Figure 1.4. This definition quantifies the reduced power as it passes through the atmosphere.

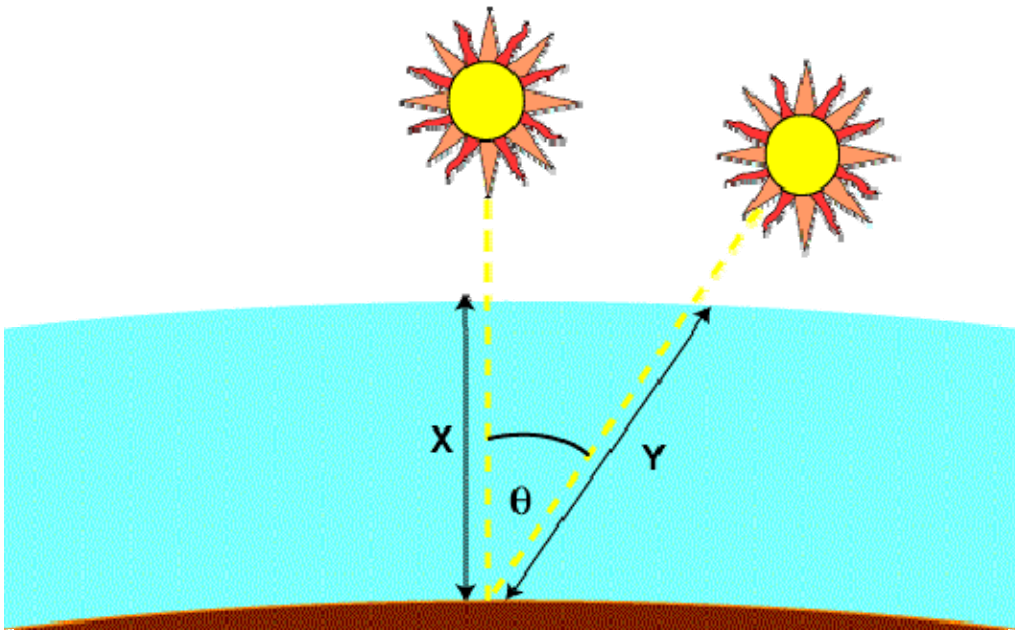

Figure 1.4 – The air mass represents the proportion of atmosphere that the light must pass through before striking the Earth relative to its overhead path length [8].

AM0 is the standard spectrum outside the Earth's atmosphere and is used for measuring the performance of solar cells in space. AM1.5G (global) is the standard spectrum at Earth's surface and includes direct and diffused radiation. AM1.5D (direct) includes only direct radiation on the Earth's surface. Concentrator solar cells also use low aerosol depth spectrum, low AOD. Low AOD is an adaptation of AM1.5D that includes the ratio of low- to high-energy light and is lower than the standard AM1.5D.

This standard was adopted because of the current limit in the third or fourth junction of a multijunction device is much more pronounced in low-AOD spectrum as compared to AM1.5D [9].

As presented here, solar cells are complicated structures with many design parameters. The science of properly measuring terrestrial solar cells is also a complicated matter and because of this, published and world record results are measured and qualified at four designated laboratories. In this work the devices were tested in-house with four-point measurements with a Keithley 2410 source meter. The light measurements used a SoLux lamp, operating at 4.0 A and 11.0 V replicating natural daylight. The measurements were calibrated with a GaInP (1.9 eV) device provided by NREL. The NREL sample had an unofficial short-circuit current of 1.19 mA at AM 1.5G. Based on this result, our measurements were conducted at approximately 4× concentration at AM 1.5G.

1.2. III-N Materials

Gallium Nitride (GaN) and related III-V materials have attracted a great deal of attention because of their use in short-wavelength optical devices, as well as in high-power and high-temperature electronic devices [10, 11, 12]. In 2002, the bandgap value of Indium Nitride (InN) was discovered to be lower than previously recorded. This was in part related to the ability to produce high-quality, single crystalline material. Previously recorded bandgap values of 1.8 eV and 2.1 eV were estimated from absorption spectra obtained on polycrystalline and nanocrystalline wurtzite InN prepared by electron beam plasma [13], reactive dc planar magnetron sputtering [14], and radio frequency (RF) reactive magnetron sputtering [15]. In 2002, Davydov et al. [16] and Wu et al. [17] determined that the bandgap of InN is 0.65 - 0.8 eV from transmission spectra,

photoluminescence, and photomodulated reflectance techniques. However, there still remains a debate about the bandgap value, specifically the origin of the larger bandgap values [18, 19] and the relation to oxygen-compound and bandfilling effects [20, 21]. For the purpose of this research, the bandgap value of 0.65 – 0.8 eV is adopted and is confirmed in Chapter 2.

1.2.1. Bandgap Values

The lower bandgap value of InN expands the range of the optical emission of direct bandgap nitride-based devices from ultraviolet to near infrared regions, InN to AlN, ~ 0.7 – 6.2 eV, as shown in Figure 1.5.

InN-based devices are promising because of their outstanding material properties such as small effective mass, large electrical mobility, and high peak and saturation velocities [22]. Unfortunately, InN has a low dissociation temperature at high equilibrium vapor pressure of nitrogen, which makes it less suitable to be grown by vapor deposition [23]. Therefore, RF-plasma molecular beam epitaxy (MBE) is an essential technology for obtaining high-quality InN films and In-rich $In_xGa_{1-x}N$ ($x \geq 0.25$), because of the facilitation of low growth temperatures compared with other deposition techniques [23].

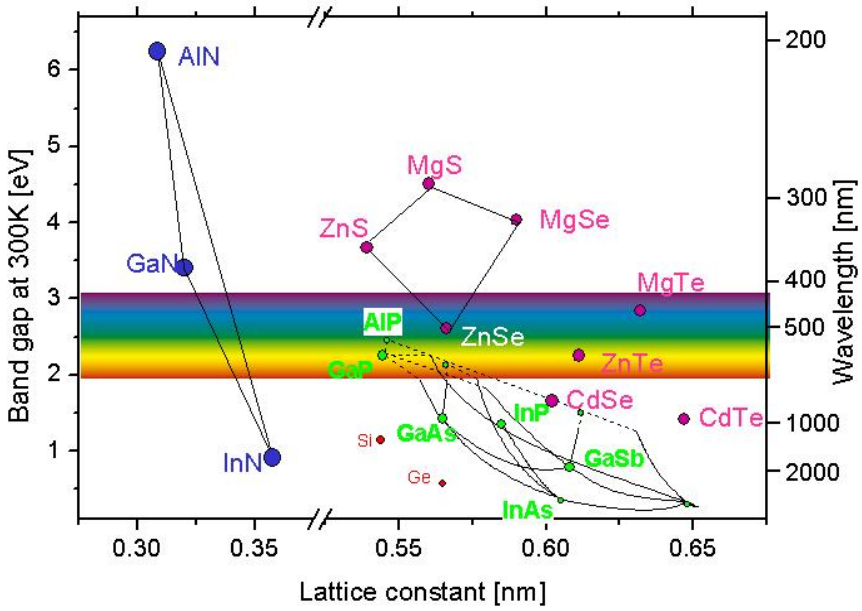

Figure 1.5 – Room temperature bandgap energy versus lattice constant of III-N semiconductors and other common semiconductors [24].

The $In_xGa_{1-x}N$ material system is a ternary system where the bandgap of the system is determined by the composition ratio of In to Ga:

$$E_G(x) = E_G(InN)x + E_G(GaN)(1-x) - x(1-x)b. \quad (2)$$

$E_G(InN)$ is equal to 0.7 eV, $E_G(GaN)$ is equal to 3.4 eV, and b is the bowing parameter, which accounts for the non-linear fit of bandgap energies, and is equal to 1.43 eV [25].

The $Al_xGa_{1-x}N$ material system is defined in a similar equation:

$$E_G(x) = E_G(AlN)x + E_G(GaN)(1-x) - x(1-x)b. \quad (3)$$

$E_G(AlN)$ is equal to 6.2 eV, $E_G(GaN)$ is equal to 3.4 eV, and b is equal to 0.7 eV [26].

1.2.2. InN and GaN Phase Separation

Unfortunately, all $In_xGa_{1-x}N$ materials must overcome a well documented phase separation in $In_xGa_{1-x}N$ films with high In composition because of the low miscibility of InN in GaN. Elyukhin et al. [27] used theoretical calculations based on the valence-force-field (VFF) model [28, 29] to predict that phase separation in $In_xGa_{1-x}N$ strongly

depends on temperature and In composition. As an example, at a growth temperature of 800 °C, the predicted In composition is less than 6% [28] because of the In loss dissociation temperature. However, biaxial strain [30] can suppress In phase separation and acts as a driving force to form ordered structures. Spinodal decomposition occurs below a critical temperature for relaxed films and for a range of alloy compositions. This decomposition defines the miscibility gap of the alloy composition at a given temperature [30]. However, it has been shown that the critical temperature lowers significantly because of biaxial strain, which suppresses the miscibility gap [31, 32]. Therefore, In phase separation can be controlled by managing biaxial strain using a strained system of InGaN/GaN [30]. Chapter 3 contains details on the growth of $In_xGa_{1-x}N$ films with increased growth rate leading to diminished phase separation.

1.2.3. Polarization and Piezoelectric Effects

A unique feature inherent in III-nitrides is the strong polarization [33, 34]. Polarization is present along the wurtzite c-axis as a consequence of the non-centrosymmetry of the wurtzite structure and the large ionicity of the metal-nitrogen bonds. The net polarization is composed of two parts: (1) spontaneous, which is inherent to the material and (2) strain-induced piezoelectricity; both are determined by the polarity of the III-nitride. Spontaneous and piezoelectric polarization, present in wurtzite III-nitrides, influences the optical and electrical properties of the material. Ambacher et al. [35] reported ~ 1 MV/cm values for sheet charges and electric fields induced by polarizations in III-nitrides.

As mentioned previously, the direction of spontaneous polarization in the III-nitrides is along the c-axis, typically a growth direction for MBE and metalorganic chemical

vapor deposition (MOCVD). The c-axis direction consists of two opposite stacking sequences of atomic layering, resulting in either cation-face (metal) or anion-face (nitrogen) epitaxy. Figure 1.6 shows the schematics for a GaN and an InN film, showing the direction of polarity. Ga- and In- polarity is in the [0001] direction and N-polarity is in the [000-1] direction.

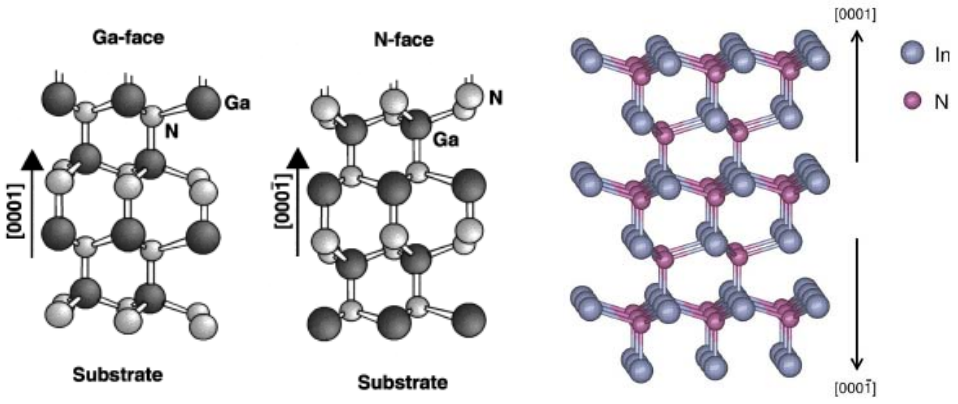

Figure 1.6 – Ball and stick model illustrating the crystal structure of (a) wurtize Ga-polarity and N-polarity GaN [35] and (b) In-polarity [0001] and N-polarity [000-1] directions of wurtzite InN. The surfaces of the In- and N- polarity faces of InN are both shown with In termination [36].

All growths conducted in this research were grown metal-polar. The AlN buffers used were grown with thicknesses greater than 100 nm, insuring that the film was Al-polar and the following films were either Ga- or In-polar. For GaN growth, Ga-polar films are smooth, single-crystalline, whereas N-polar films have rough faceted surfaces [37]. For InN growth, the polarity of the film can significantly affect the growth temperature. In-polar InN have limited growth temperatures, ~ 350 – 500 °C, while N-polar InN can be grown almost 100 °C hotter [38]. In-polar InN growth difficulties will be discussed in more detail in Chapters 2 and 5.

The direction of piezoelectric polarization is dependent on the polarity of the material as well as strain in the material. Spontaneous and piezoelectric polarizations are parallel

and add together (↓↓) when planar strain is tensile and are anti-parallel (↑↓) when planar strain is compressive. Strain in the epitaxial layers is primarily caused by the lattice mismatch and thermal expansion coefficients with the substrate during growth. The epi-layer may relax at the heterointerface depending on growth conditions and film thickness relative to the "critical thickness," required for dislocation generation. Layers that are thinner than the critical thickness have their mismatch partially accommodated by elastic strain. Layers thicker than the critical thickness, predominately accommodate the lattice mismatch by combinations of residual strain, dislocations, and three-dimensional growth. AlN films have an approximated critical thickness of 4.48 ± 0.14 Å [39] on sapphire (Al_2O_3), GaN has a critical thickness of 29 ± 4 Å [40] on AlN, and InN films on c-plane GaN have a critical thickness of approximately one monolayer. The piezoelectric polarization in the material can be determined by the strain-relaxation profile along the thickness of the epi-layer. The strain state and degree of structural perfection of the material influence the electrical and optical performance of the devices [41].

Polarization can be used constructively in solar cell design to enhance carrier collection, reducing ohmic resistances, and band bending to reduce surface recombination. Unfortunately, polarization can also generate electric fields and energy spikes in the bands, which are detrimental for carrier collection, and creates potential wells that can act as recombination centers. Therefore, III-nitride solar cell designs must consider polarization effects.

1.3. Molecular Beam Epitaxy

The term MBE was first used in 1970 by Alfred Y. Cho at Bell Telephone Laboratories [42] after extensive work on epitaxial films by Davey and Pankey [43], Shelton and Cho [44], and Arthur [45]. MBE growth is characterized by the interaction of a single or multiple molecular or atomic beams at the surface of a heated crystalline substrate. This interaction occurs in an ultra-high vacuum chamber (~10^{-9} torr). At this pressure the mean free path of a gas particle is approximately 40 km; therefore the gas molecules will collide with the chamber walls many times before colliding with each other. The low background pressure also provides the best available purity, because the arrival rates of contaminants are significant orders of magnitude less than typical chemical vapor deposition conditions. Unlike other deposition techniques, MBE growth is able to grow impurity-free, quality films with abrupt layers. Figure 1.7 is a schematic of a typical MBE system [46]. The chamber is cryogenically cooled with liquid nitrogen (LN_2), which prevents spurious atoms from bouncing off of the chamber walls, therefore acting as a cryopump during growth.

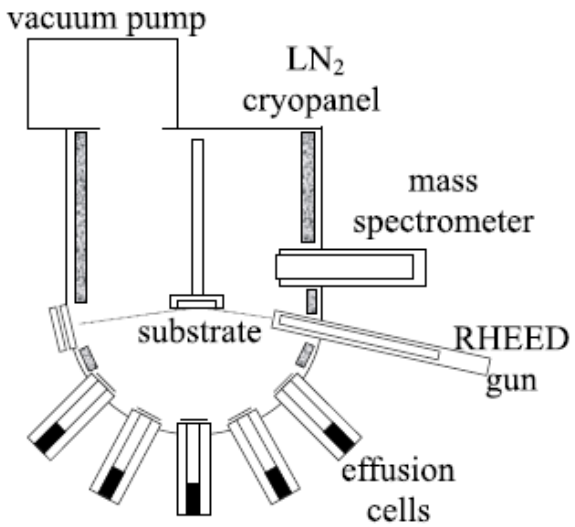

Figure 1.7 – Typical schematic of a MBE system [46].

The group III-metal sources and dopant materials are introduced through an effusion cell, where a solid material is placed in a crucible, typically made of pyrolytic boron nitride (PBN) and heated until the material sublimates or evaporates. The temperature of the effusion cells is controlled by proportional-integral-derivative (PID) control parameters, where the flux intensity can be maintained to better than 1%. The group-V source is delivered by different methods. Traditionally, arsenide and phosphide materials use either a traditional effusion cell, hydride gas sources or a valved cracker effusion cell. III-Nitride films use a nitrogen RF plasma source, where purified N_2 is converted into a more active atomic and molecular species. Shutters placed in front of the III-V sources permit direct control of the epitaxial growth surface at a monolayer level by changing the incoming beam with the opening and closing of the shutter.

1.3.1. In-Situ Characterization Techniques

As mentioned previously, MBE systems maintain a base pressure less than 10^{-9} torr. This base pressure allows for sophisticated *in-situ* growth analysis such as reflection high-energy electron diffraction (RHEED) and residual gas analysis (RGA). A RHEED system uses an electron gun that generates a beam of electrons that strike the epitaxial surface at a small angle. The incident electrons diffract from the atoms at the surface of the sample and a fraction of the diffracted electrons interfere constructively at specific angles to form regular patterns on the detector. The electrons interfere according to the position of the atoms on the sample surface, giving an indication of the growth surface. RHEED analysis is only a surface technique. It is not able to determine the bulk quality. Oscillations of the RHEED intensity (RHEED transients) can also provide information about the time needed to grow a monolayer of material. However, RHEED transients are

rarely observed on III-Nitrides, because layer by layer growth does not normally occur. Burnham et al. [47] created a closed-loop system using the RHEED oscillations and shutter modulation to reliably reproduce quality AlN and p-type GaN. Chapter 4 will discuss more details of RHEED and p-type GaN.

An RGA is a mass spectrometer and an electron multiplier that creates and quantifies the ion content in the chamber. During the growth the RGA will monitor the excess III-V fluxes in the chamber, atoms that have not incorporated in the epitaxial film or are desorbed. Similar to RHEED oscillations, RGA oscillations can be used during shutter modulation to determine the amount of material not incorporated into the film. Additionally, an RGA is also used to detect any impurities in the chamber or in conjunction with helium to detect leaks in the vacuum system.

The substrates used in this work were either Ga-doped Germanium (Ge) oriented (111) or c-plane oriented Al_2O_3 with a polished growth side and rough backside. The Al_2O_3 had refractory metals deposited on the rough backside to promote thermal absorption. Details on the cleaning procedure, backside metallization, and nitridation/AlN buffer conditions are detailed in Appendix B.

CHAPTER 2: Growth of InN

Until recently, InN has been less studied compared to other (AlGa)N-related materials because of a low dissociation temperature at high equilibrium vapor pressure of nitrogen, which makes it less suitable to be grown by vapor deposition [23]. Therefore, RF-plasma MBE is an essential technology of obtaining high-quality InN films because of the facilitation of low growth temperatures compared with MOCVD [23]. The following chapter will explore the growth and crystalline characteristics of InN.

2.1. Growth of InN on Germanium Substrates

InN epitaxial layers have been extensively grown on Al_2O_3 substrates. InN films have a large lattice mismatch of ~25% with Al_2O_3, which creates an extremely high density of structural defects [22, 48]. As an alternative, (111)-oriented Si substrates, which have a smaller lattice mismatch of 8%, have been used unsuccessfully because of the formation of SiN_x layers on the substrate face resulting from unintentional nitridation [22, 49].

In the absence of a lattice matched choice for a substrate, an alternative criterion for the substrate selection might be based on the energy band suitable for vertical conduction devices. The first criterion for such a selection is a substrate with a comparable bandgap. Germanium has such a bandgap, being within 40 meV of the bandgap of InN [50]. The second criterion is for a suitable and small band offset. Currently, these values are unknown, as the bandgap of InN is in theoretical dispute. A (111)-oriented Ge substrate has a smaller lattice mismatch with InN of approximately 11.3%. Although the expected

dislocation density is still quite large, the use of Ge for vertical conduction devices may be a practical alternative. Future devices such as multi-junction tandem solar cells, heterojunction bipolar transistors, or photodetectors could benefit from the use of an optimally selected vertically conducting substrate.

2.1.1. Growth Conditions and Analysis

The (111)-oriented Ge substrates were solvent cleaned, outgassed, and loaded into the growth chamber. A substrate temperature of 475 °C was maintained with an In flux varied from 1.0 - 1.4 × 10^{-7} torr beam equivalent pressure (BEP). An EPI-unibulb nitrogen source operated at 350 W and a flow rate of 0.34 sccm was used. The film thickness was measured at 0.4 μm.

The crystallographic structure was studied by double-crystal X-ray diffraction (XRD) using a Philips X'Pert diffraction system. Figure 2.1 shows the ω-2θ XRD scan for the InN grown on Ge. Both (0002) InN and (111) Ge diffraction peaks are clearly observed. The (111) and (0002) peak positions were θ = 13.581 ° and θ = 15.768 ° for Ge and InN, respectively. This result indicates the epitaxial relationship of $[0001]_{InN} \parallel [111]_{Ge}$.

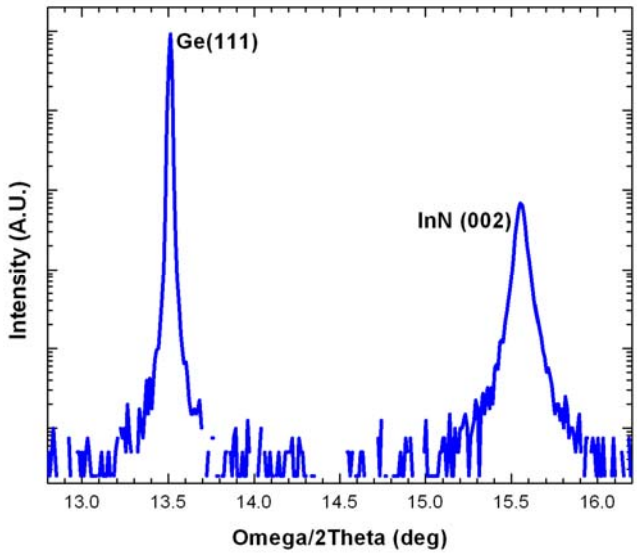

Figure 2.1 – ω-2θ of InN/Ge showing a (111) Ge peak at 13.581° and an InN peak at 15.768°.

The best (0002) ω-2θ full-width half-maximum (FWHM) value was ~144 arcsec. Further characterization of the film was done with XRD pole-figure measurements. The pole-figure shows peaks with six-fold symmetry, which confirms the presence of wurtzite InN. Wurtzite epitaxial InN has previously been demonstrated on (111)-orientated Si substrates [22], with the best (0002) rocking curve measurement of ~2597 arcsec FWHM, indicating significant tilt and mosaic grain structure.

The microstructure of the InN film was characterized by transmission electron microscopy (TEM) and again confirmed that the InN film is wurtzite. The diffraction pattern in Figure 2.2 was taken at the InN/Ge interface along the $[110]_{Ge}$ zone axis.

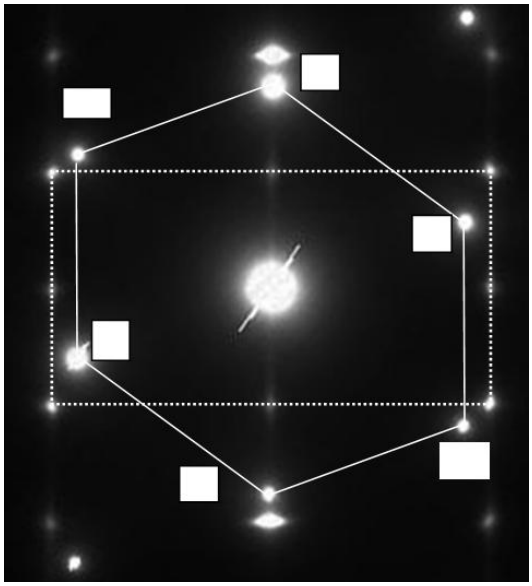

Figure 2.2 – Selective electron diffraction pattern taken at the interfacial region on InN/Ge along $[110]_{Ge}$ zone-axis, which is parallel to $[11\text{-}20]_{InN}$.

The pattern with bright dots connected by solid lines is ascribed to the Ge substrate and the weak spots connected by dotted lines are from the InN film. The orientation relationship between InN and the Ge substrate, as shown in Figure 2.2, can be described as follows: $[110]_{Ge} \| [11\text{-}20]_{InN}$ and $(111)_{Ge} \| (0001)_{InN}$. This epitaxial relationship between the InN and the Ge substrate is similar to that of InN on Si substrates [22].

TEM images were used to analyze structural qualities such as stacking faults and threading, screw, and edge dislocations. Analysis by diffraction contrast microscopy shows that the InN film contains a high density of threading dislocation as well as grain boundaries, as shown in Figure 2.3.

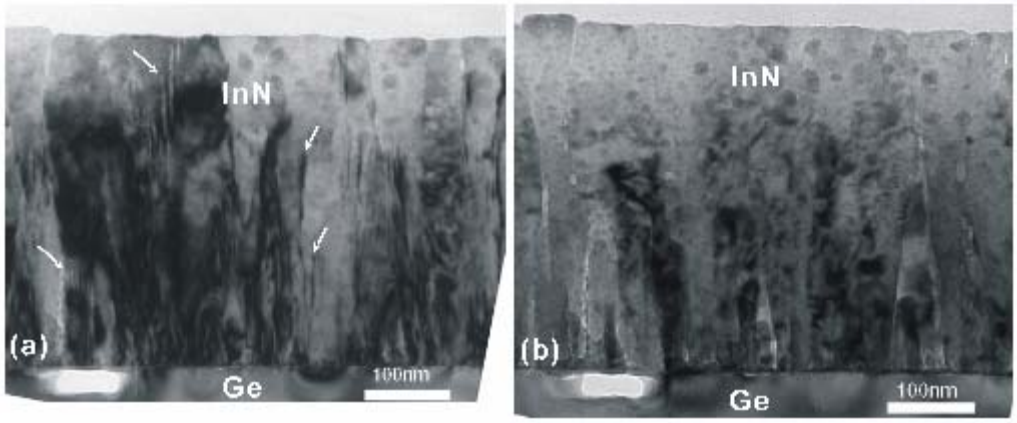

Figure 2.3 – Bright field diffraction contrast TEM images taken under different conditions to view threading dislocations of (a) screw type, g = 0002 and (b) edge type g = 1-100.

The dislocations were predominately screw type, with densities on the order of 10^{10} cm^{-2}. The high dislocation density was generated to accommodate misfit strain in the basal planes between the InN film and the Ge substrate. At the early stage of growth, the film consists of nanoscale columnar crystallites. These crystallites subsequently coalesce into larger crystallites. Figure 2.3(a) shows a high threading dislocation density near the interface, which reduces with increasing thickness, similar to that commonly found in GaN epitaxial layers [51].

The cross-sectional TEM images show an intermediate layer between the InN and the Ge substrate. This boundary region can be interpreted as an amorphous interlayer of unknown origin or perhaps a low symmetry monoclinic phase possibly resulting from the nitridation of Ge to form β-Ge_3N_4 [52, 53]. Alternatively, In-Ge compounds have a well-documented eutectic of 156.634 °C, well below the growth temperature of 475 °C used in these experiments [54]. The intermediate layer may be a result of the formation of an In-Ge-N alloy. Further evidence of the formation of a eutectic is given by the occasional observation of etch pits in the Ge substrate shown in Figure 2.3. These pits suggest that a

reaction is occurring between the Ge and a species present during the growth to form a compound with a lower melting temperature.

The optical properties of the InN film were investigated using photoluminescence (PL) measurements at 15 K. Details of the PL setup can be found in Ref. [55]. Figure 2.4 shows the PL of the InN/Ge sample and a Ge control sample.

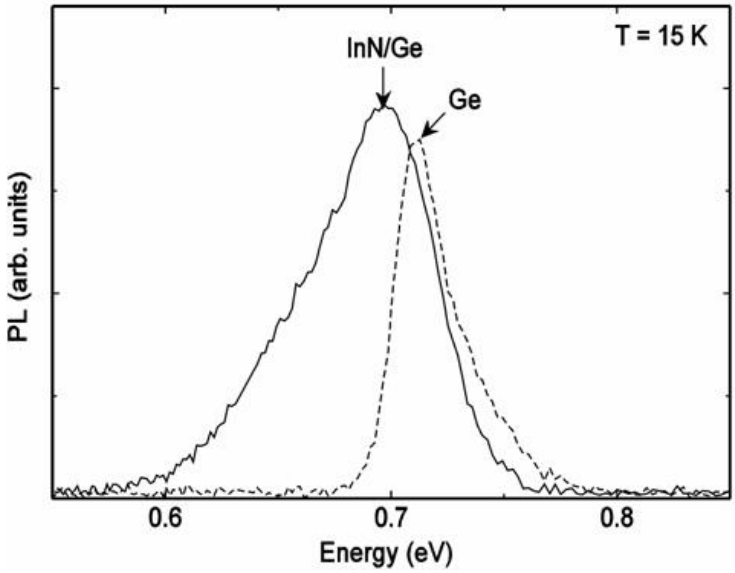

Figure 2.4 – PL of the InN/Ge sample (solid) curve and the Ge control sample similar to the substrate (dashed curve) taken at 15K. The PL of the Ge was obtained by excitation 10× that of the InN/Ge sample. The peak of the InN/Ge is near 0.69 eV, while the peak for the Ge sample is approximately at 0.71 eV.

Strong luminescence was observed at ~0.69 eV for the InN epitaxial layer grown on Ge. This value is close to reports of a bandgap near 0.7 eV [16, 17]. The PL peak has a characteristic low-energy tail, which is most likely a result of defects in the InN film or possibly related to a graded bandgap resulting from the presence of an In-Ge-N alloy. In contrast, the Ge standard sample requires 10× the excitation to show a comparable luminescence at 0.72 eV, which corresponds to the Ge bandgap at this temperature range [56]. Collectively, the difference of PL peak energy, PL line shape, and PL intensity

between the two materials at 15 K allows differentiation of the InN film from the Ge substrate.

This investigation of InN grown on a Ge substrate found that wurtzite InN has been grown with the polar axis parallel to the (111)-oriented Ge substrate and has a lattice mismatch of 11.3% between the InN film and the Ge substrate. TEM shows that the dominant structural defects are threading dislocations, stacking faults, and a disordered intermediate layer existing at the interface between the InN film and the Ge substrate. The threading dislocation density decreased with increasing thickness of the InN epitaxial layers. PL at 15K shows that the InN has a strong luminescence peak at the reported 0.68 eV bandgap. Along with the recently reported bandgap of InN in the proximity of the bandgap of Ge, InN/Ge is a promising candidate for vertical conduction devices, such as solar cells.

2.1.2. Epitaxial Al Interconnect Layer

A current challenge of InN photovoltaic (PV) devices is a strong band bending [57, 58, 59] at the surface/heterointerface, which results in the inability to form rectifying solid-state junctions. Specifically, the strong band bending at the collecting junction prevents the collection of minority carriers, leading to ohmic junctions through a tunneling mechanism. If the background doping in InN could be substantially lowered, such band bending near the surfaces could be used beneficially as an efficient means of reducing surface recombination by redirecting minority carriers away from the defective surface.

Another challenge InN PV-based devices face is the demonstration of p-type doping. P-type doping is needed to create the p-n sub-cell collecting junction and for the

degenerately doped interconnect regions. The p-n collecting junction facilitates current collection through the electrostatic field created by the spatially separated ionized donors and acceptors. Without such p-n junctions, photogenerated EHPs cannot be separated; therefore no photocurrent is produced. Additionally, traditional tandem solar cells use degenerately doped materials at the sub-cell junctions to facilitate tunnel junctions. In the tunnel junction, the conduction and valence bands of the two sub-cells overlap, allowing the electrons collected at the p-n junction to tunnel from the n-type emitter of one sub-cell into the neighboring holes in the adjacent sub-cell base. Without the p-InN, an InN PV tandem device will need a substantially different means of current collection, such as an internal Schottky barrier or heterojunction for current collection. Otherwise, the photogenerated EHPs will not result in current in the external circuit.

One approach to eliminate the need for degenerate p-type doping and exploit the ohmic behavior of InN/Ge is the use of an epitaxial layer of Al as a sub-cell interconnect. The epitaxial Al is analogous to a wire used to connect a series of diodes. This epitaxial Al layer also isolates the Ge from the InN, therefore avoiding the eutectic reaction of In-Ge as mentioned in Chapter 2.1.1 [54].

Figure 2.5 shows the RHEED images of the crystalline Al deposited on (111)-oriented Ge at different temperatures. Figure 2.5(a) is an image taken of the crystalline Al after 60 seconds of deposition at a substrate temperature of 100 °C. The RHEED image is spotty, indicating a rough surface.

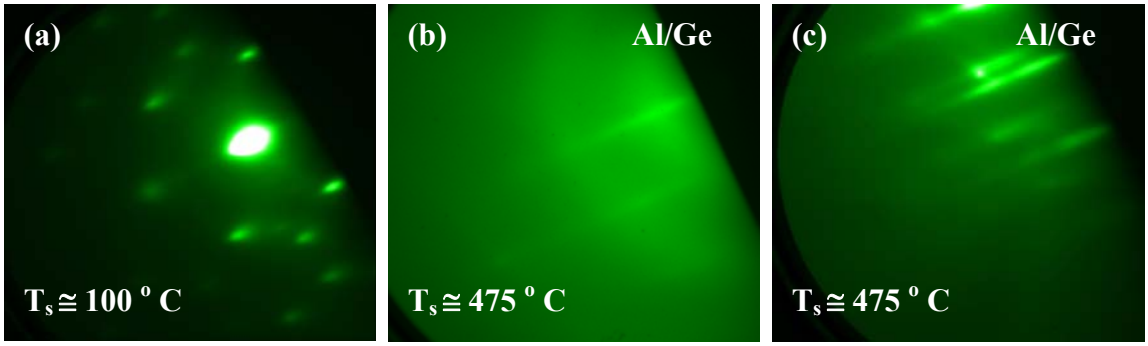

Figure 2.5 – RHEED images of Al/Ge. (a) Crystalline Al after 60 seconds on Ge at 100 °C; (b) Al on Ge after substrate temperature increased from 100 to 475 °C; (c) Crystalline Al after 60 seconds on Ge at 475 °C.

The spotty RHEED pattern became streaky post-deposition at an increased substrate temperature of 475 °C, indicating a smooth Al/Ge surface, as shown in Figure 2.5(b). However, other attempts at depositing Al directly at a substrate temperature of 475 °C for 60 seconds resulted in the persistence of both Al RHEED spots and Ge RHEED streaks, shown in Figure 2.5(c). The Al RHEED spots indicate Al-droplets, not epitaxial Al. Al-droplets on the higher temperature deposition samples were confirmed post-growth using optical microscopy as shown in Figure 2.6.

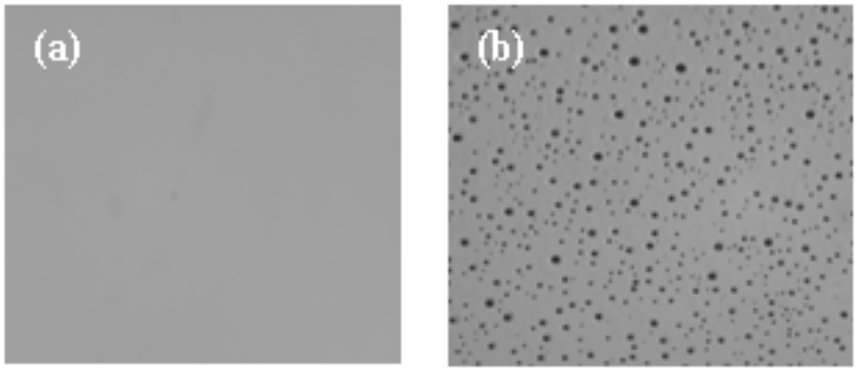

Figure 2.6 – Microscopic image of (a) Al/Ge deposited at 100 °C and (b) Al/Ge deposited at 475 °C.

As mentioned previously, the epitaxial Al can act as a collecting junction for tandem solar cells between the different tandem stacks. However, the epitaxial Al does not

completely remove the need for p-type doping of InN, which is required to create the sub-cell p-n junctions. Epitaxial Al also has the additional benefit that it may provide domain matching in the Ge-Al-InN interface. Figure 2.7 shows the crystallographic alignment of Ge on Al and InN on Al.

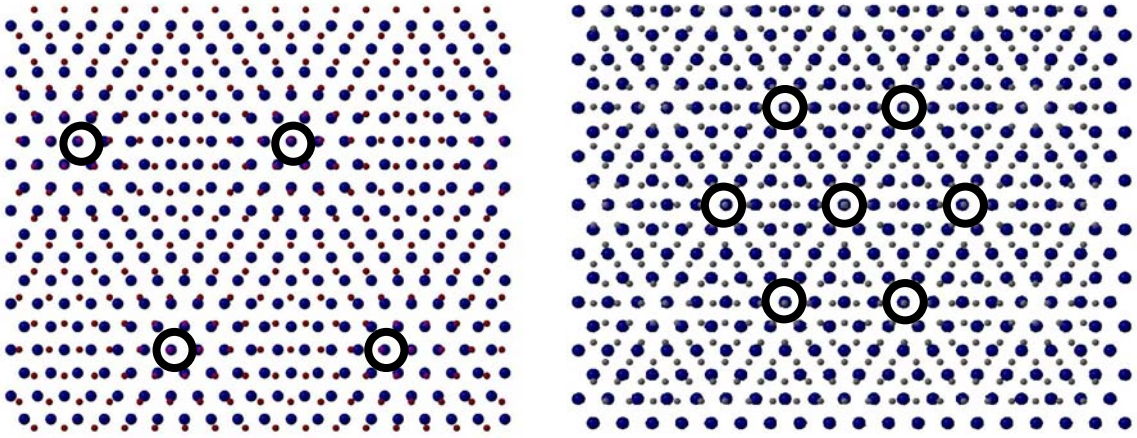

Figure 2.7 – Crystallographic alignment of (a) Ge (large dots) and Al (small dots) and (b) InN (large dots) and Al (small dots). The circles indicate domain matching.

Every 7th unit cell of Al aligns to within 0.21 % to every 8th unit cell of Ge. Every 4th unit cell of InN aligns to every 5th unit cell of Al to within 1%. Therefore, the Al buffer layer, while still resulting in highly columnar growth of InN, may result in reduced grain tilt of the film. The ability of the film to align based on domain matching is a controversial and possibly incorrect model, accounting for the previously demonstrated [55] improved grain alignment as evidenced by XRD. It is included here for the sake of completeness.

2.2. The Bandgap Value of InN

The recent discovery of a lower bandgap of InN has sparked a debate about the origin of the higher quoted bandgap value. It is believed that the higher value is related to the presence of oxygen, previously thought to be present as an alloy, although more recently it has been suggested that a discrete oxynitride compound is a better interpretation than that of an alloy [20, 60, 61, 62].

2.2.1. Growth Conditions and Analysis

During a series of experiments, a vacuum window was slightly breeched in the MBE system, resulting in a miniscule leak that raised the MBE base pressure from $\sim 1\times10^{-10}$ to $\sim 1\times10^{-9}$ torr over the course of several growths. This minute level of leak would not be detectable in growth technologies where ultra-high vacuum conditions are not used. Therefore, the following results emphasize the sensitivity of InN to extremely low levels of oxygen contamination. In these series of samples, it was determined that there was unintentional *in-situ* oxygen incorporation in the InN films of increasing magnitude as the leak worsened. Evidence of oxygen was found while studying the crystallographic structure of the InN/AlN/ Al_2O_3 sample by XRD. Figure 2.8 shows the 2θ-ω scan of this sample with peaks observed at $2\theta = 30.874°$ and $31.158°$.

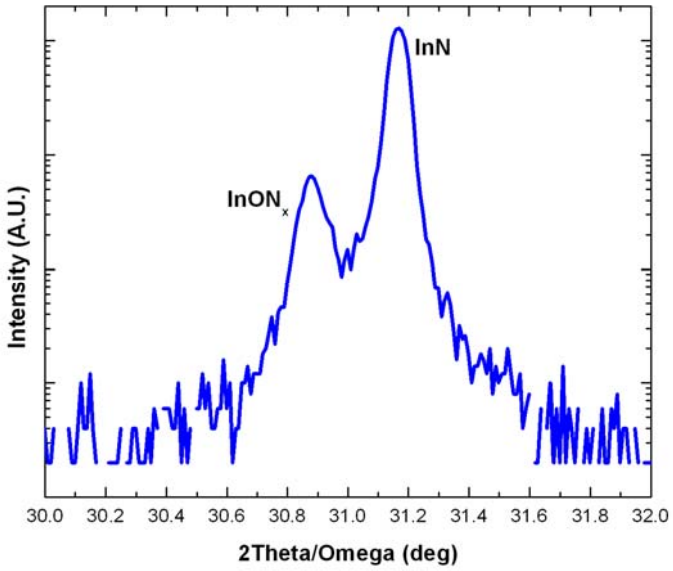

Figure 2.8 – 2θ-ω XRD scan of InN/AlN/Al_2O_3 showing an $InON_x$ peak at 2θ = 30.874° and an InN peak at 31.158°.

The higher angle peak clearly matches wurtzite InN, but the lower angle peak does not match zinc-blende InN, zinc-blende In_2O_3, or metallic In; those peaks are located at 2θ = 31.389°, 30.585°, and 36.304°, respectively. The lower angle peak was only found in material grown when the leak was present in the MBE system. As this new peak is between zinc-blende InN and zinc-blende In_2O_3 peak, it will be described as $InON_x$. Figure 2.9 shows the pole-figure of this sample showing evidence of wurtzite {10-12} InN (labeled B) that is 30° rotated with respect to the {11-23} Al_2O_3 substrate (labeled A) and the presence of a zinc-blende material {422} $InON_x$, 90° symmetric peak (labeled C.)

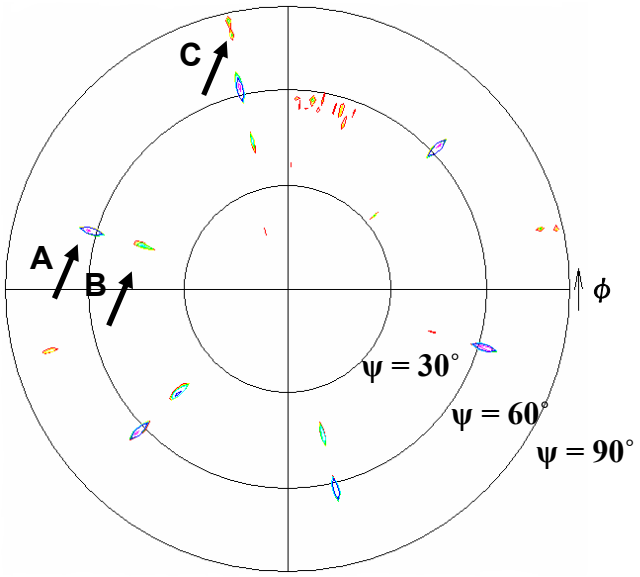

Figure 2.9 – Pole-figure of InN/AlN/Al_2O_3 showing wurtzite Al_2O_3 peaks {11-23}, wurtzite InN peaks {10-12}, and zinc-blende $InON_x$ {422}, labeled A, B, and C, respectively. ψ is the angle relative to the normal surface.

Upon examination of previous samples grown under conditions of higher than normal base pressure, indicative of an increasing magnitude leak, 2θ-ω scans did not show any indication of peaks related to $InON_x$. However, these same samples without 2θ-ω indium oxynitride peaks did show zinc-blende $InON_x$ {422} diffraction peaks when a pole-figure was measured, indicating that the {422} reflection is a sensitive measure of the existence of mixed indium oxynitrides.

The PL spectrum of an InN epitaxial layer grown on an AlN buffer layer on a Al_2O_3 substrate and a reference sample of an epitaxial AlN layer grown on a Al_2O_3 substrate is shown in Figure 2.10. Note, that the PL of InN/AlN/Al_2O_3 sample did have an $InON_x$ peak as evidenced in XRD measurements.

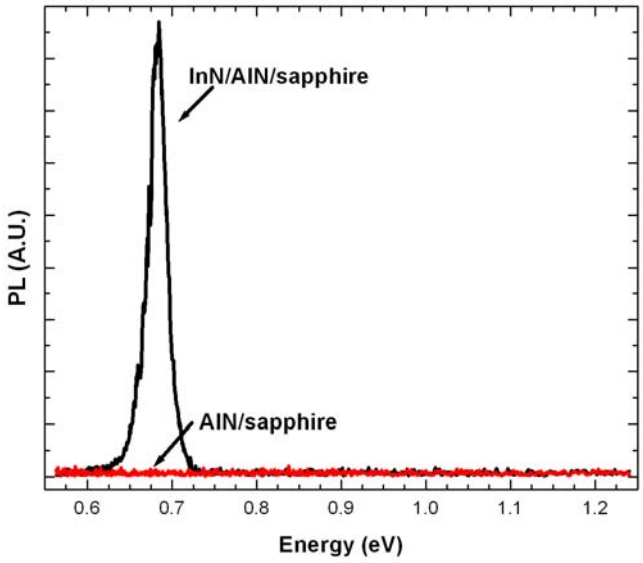

Figure 2.10 – PL on InN/AlN/Al_2O_3 (black line) and AlN/Al_2O_3 (red line) taken at 12K with peak intensity at ~ 0.7eV.

PL was observed at a peak centered at 1771 nm, corresponding to approximately 0.7 eV for the InN/AlN/Al_2O_3 sample and no contribution from the AlN/Al_2O_3 reference sample. Figure 2.11 also shows the PL spectrum of the previously mentioned InN/AlN/Al_2O_3 and reference AlN/Al_2O_3, along with InN/Ge and a bare Ge wafer. The InN/AlN/Al_2O_3 and the AlN/Al_2O_3 sample have an observed narrow peak at 700 nm, corresponding to approximately 1.77 eV. This PL energy is thought to be consistent with emission from the Al_2O_3 substrate [63] and should not be confused with the reported PL from the InN, as the AlN/Al_2O_3 sample contains no InN. Additionally, the InN/Ge sample shows no PL peak in this range.

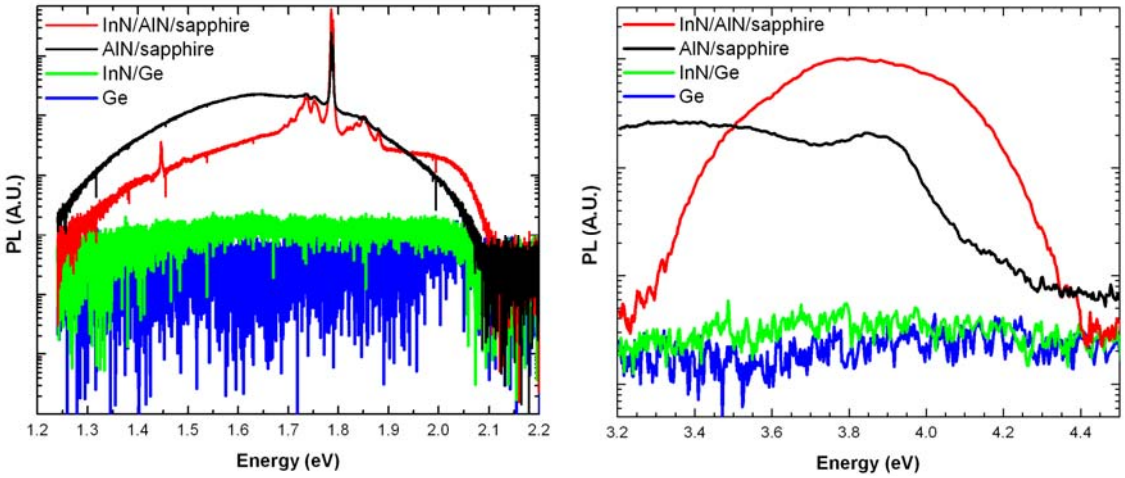

Figure 2.11 – PL of InN/AlN/Al_2O_3, AlN/Al_2O_3, InN/Ge, and bare Ge wafer taken at room temperature with (a) peak intensities at ~1.77eV and (b) peak intensity at ~3.8 eV. The peaks in visible, IR, and UV range used different optical configurations. Therefore, the output data was multiplied to achieve a comparable intensity leading to arbitrary units for PL intensity.

Figure 2.11(b) shows the ultra-violet (UV) PL spectrum for the same set of samples used in Figure 2.11(a). As shown in Figure 2.11(a), the InN/AlN/Al_2O_3 has a peak intensity measured at 330 nm, corresponding to approximately 3.8 eV. As previously mentioned, the InN/AlN/Al_2O_3 was grown under a leaky MBE environment and from XRD 2θ-ω, an $InON_x$ peak was found. It is thought that the $InON_x$ film is the cause of the 3.8 eV PL peak. From the literature, In_2O_3 has a known bandgap of 3.75 eV [64]. Also, Figure 2.11 shows that there is no significant emission from the AlN/Al_2O_3 sample, the InN/Ge sample, or the bare Ge wafer. Additionally, the peaks in the visible, infrared, and UV range used different optical configurations. Therefore, the output data was multiplied to achieve a comparable intensity leading, to arbitrary units for the PL intensity.

The results in Figure 2.11 provide insight into the argument of the bandgap value of InN and the origin of the 1.7 - 1.9 eV bandgap. The peak found on the InN/AlN/Al_2O_3 at ~1.7 eV is related to emission from the Al_2O_3 substrate [63]. A similar 1.7 eV PL peak

was not found on the InN/Ge samples or on the bare Ge wafers. Although PL is not a definitive measure of bandgap, as emission can result from multiple sources including deep levels, a possible explanation for the origin of the higher InN bandgap could be the contribution from the Al_2O_3 substrate from pump absorption or merely Al_2O_3 emission. Further research into this matter is required.

It was also found from annealing pure InN films in oxygen that high-quality wurtzite InN films have a strong affinity for incorporating oxygen into the crystal structure [60, 62]. Moreover, Davydov et al. [20] state that samples saturated partially with oxygen show a shift toward higher bandgap energies than those of untreated InN. It is believed that the incorporation of oxygen may play a key role in determining the apparent properties of InN, including the bandgap and the lattice constant. The results presented herein add to this data, indicating that small oxygen exposure during growth does not shift the PL peak from approximately 0.68 eV. However, there is evidence of an oxynitride related phase as determined from XRD.

The bandgap of InN was determined to be approximately 0.7 eV. However, an additional higher energy PL emission of ~ 1.7 eV and 3.8 eV was observed for InN material grown on an Al_2O_3 substrate and under a leaky MBE environment. The 1.7 eV PL emission is possibly caused by the pump absorption or Al_2O_3 emission from the Al_2O_3 substrate. Based on XRD results, the 3.8 eV bandgap energy is possibly related to $InON_x$ or a highly degenerate surface layer. Further research continues on p-type doping InN and $In_xGa_{1-x}N$, along with current technical issues related to implementing $In_xGa_{1-x}N$ solar cell devices.

2.3. Summary

Several InN experiments have been conducted to prove that InN has the potential to become a promising material for solar applications. InN was epitaxially grown on (111)-oriented, Ga-doped germanium substrates by MBE. XRD and TEM investigations have shown that the InN epitaxial layers consist of a wurtzite structure, which has the epitaxial relationship of $(0001)_{InN} \| (111)_{Ge}$. Consistent with recent reports implying a narrow bandgap of InN, a strong PL peak with energy of 0.69 eV was observed for InN/Ge, as well as for InN/AlN/Al_2O_3. Epitaxial Al was deposited on a Ge substrate with InN grown on this epitaxial Al layer. The use of an epitaxial Al provides an efficient sub-cell interconnect mechanism for series connection of tandem solar cells. Chapter 3 will explore the viability of an $In_xGa_{1-x}N$ alloy for future solar devices.

CHAPTER 3: Growth and Characteristics of $In_xGa_{1-x}N$ Epitaxial Layers

The recent revision of the bandgap valve of InN has given the III-nitride alloy system an extended range of direct bandgaps from InN to AlN (0.68 – 6.2 eV) [16, 17, 65]. However, it is challenging to develop $In_xGa_{1-x}N$ materials which can span energy bandgaps from 0.7 to 3.4eV, for high efficiency solar cells by MBE or metalorganic chemical vapor deposition (MOCVD). Successful development of high efficiency solar cells currently requires two technical challenges in $In_xGa_{1-x}N$: control phase separation, normally observed in $In_xGa_{1-x}N$ materials and obtaining p-type conductivity in high In composition of $In_xGa_{1-x}N$ materials. Additionally, with the revision of the bandgap of InN, there is limited material property information, specifically absorption coefficients. Transmission and PL measurements are used to determine the absorption coefficient of the $In_xGa_{1-x}N$ materials. The absorption coefficient will be used to determine the maximum thickness required for complete absorption in the $In_xGa_{1-x}N$ solar cell.

This present work has determined that two types of phase separation exist and have been classified into two categories: compositional and structural. Phase separation causes fluctuation of the energy bandgap, which will be detrimental to current collection in solar cell devices. Compositional phase separation is caused by the immiscibility of InN in GaN and structural phase separation is defined as the mixture of zinc-blende and wurtzite material in the epitaxial film. The following chapter will explore the growth and crystalline characteristics of $In_xGa_{1-x}N$.

3.1. Characteristics of $In_xGa_{1-x}N$ Epitaxial Layers

One specific device of interest is an $In_xGa_{1-x}N$ solar cell with a targeted bandgap of 2.4 eV, equivalent to 27% In incorporation. Previously, record high open circuit voltages have been demonstrated [66] for $In_xGa_{1-x}N$ photovoltaic devices. These devices are attractive because over half the available power in the solar spectrum is above 2.0 eV photon energy, as was seen in Figure 1.3. The following sections will detail the elimination of compositional phase separation with increased growth rate and determine the absorption coefficient for an $In_xGa_{1-x}N$ film with a bandgap of 2.4 eV from PL and transmission measurements.

3.1.1. Growth Conditions and Analysis

Two different substrates were used in this study: the phase separation study used c-plane Al_2O_3 substrates and the absorption study used hydride vapor phase epitaxy (HVPE) GaN templates. All samples were solvent cleaned and outgassed following the procedure outlined in Appendix B.

The HVPE samples were loaded into the growth chamber, where a 0.6 μm-thick GaN:Si was grown with a substrate temperature of 600 °C, a Ga flux of $4 - 5.8 \times 10^{-7}$ torr BEP, and the Si cell temperature was maintained at 1020 °C, leading to an electron concentration of $\sim 10^{18}$ cm^{-3}. A modulation technique (10 seconds of Ga and Si shutters open followed by 10 seconds of Ga and Si shutters closed) referred to as Metal Modulated Epitaxy (MME) [47] was used to maintain a streaky RHEED pattern, and in some cases achieved a 2×2 reconstruction pattern. Details of MME are presented in Chapter 4. The $In_xGa_{1-x}N$ was grown at a substrate temperature of 515 – 550 °C with an

In flux of $9.2 \times 10^{-8} - 1.7 \times 10^{-7}$ torr BEP, a Ga flux of $8.7 \times 10^{-8} - 1.6 \times 10^{-7}$ torr BEP, and a plasma power of 350 W with a nitrogen flow rate of 0.5 sccm.

The Al_2O_3 samples were loaded into the growth chamber and then nitrided for 30 minutes with a substrate temperature of 200 °C. The AlN buffer was grown at a constant substrate temperature of 800 °C with an Al flux of 1.45×10^{-7} torr BEP, a plasma power of 350 W, and nitrogen flow rate of 1.2 sccm. The Al shutter was modulated during growth (10 seconds of shutter open followed by 10 seconds of shutter closed). The $In_xGa_{1-x}N$:Si was grown at a constant substrate temperature of 500 °C with and In flux of $4.0 \times 10^{-8} - 1.2 \times 10^{-7}$ torr BEP, a Ga flux of $2.0 - 6.0 \times 10^{-7}$ torr BEP, a plasma power of 350 W, and nitrogen flow rate of 1.2 sccm. Si doping was maintained at a cell temperature of 1050 °C, leading to an electron concentration of $\sim 10^{18}$ cm^{-3}.

3.1.1.1. Compositional Phase Separation

The growth of high In composition $In_xGa_{1-x}N$ films is well known to exhibit several problems. InN films must be grown at low temperatures, such as 360-550 °C because of the low dissociation temperature of InN. Despite the recent popularity of the nanostructured solar cells, similar to those resulting from phase separated material, such localization of the electron and hole wave functions makes current collection more difficult and to date has led to decreased conversion efficiency.

Compositional phase separation can be suppressed by increasing the growth rate, as was initially observed in a ~0.6 μm thick $In_{0.32}Ga_{0.68}N$ film. Figure 3.1 shows the XRD ω-2θ scan, indicating that the film had negligible compositional phase separation, 32% In incorporation, and crystalline quality figures of merit better than 190 arcsec for ω-2θ

FWHM. At the time of publication this sample was the first report of 32 % In incorporation in $In_xGa_{1-x}N$, with high quality crystallinity, and with negligible compositional phase separation [65].

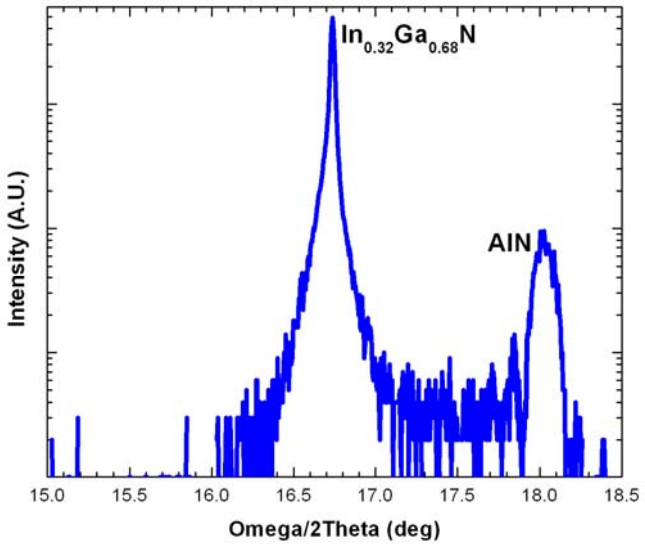

Figure 3.1– MBE growth of 32% In incorporation with negligible phase separation and growth rate in excess of 0.6-1.0μm.

This study was continued, focusing on the relationship of the III/V ratio, growth rate, and the elimination of compositional phase separation. Figure 3.2 shows XRD from five different growths, with the lowest III/V ratio resulting in the largest compositionally phase separation material - multiple phases of In incorporation at 4 and 22 % and the lowest growth rate of 0.3 μm/hr. As the III/V ratio increased, the growth rate increased, and compositional phase separation is eliminated. As the III-metal flux increased the ratio of In flux to (In + Ga) flux was kept constant. Overall the In incorporation varied from 4 – 22 % and growth rate increased from 0.3 to 0.95 μm/hr, with diminishing compositional phase separation as the growth rate increased. These results indicated that compositional phase separation can be controlled by kinetically limiting the phase

separation, using the inherent high growth rates in MBE. Therefore, high-efficiency $In_xGa_{1-x}N$ solar cells should be achievable.

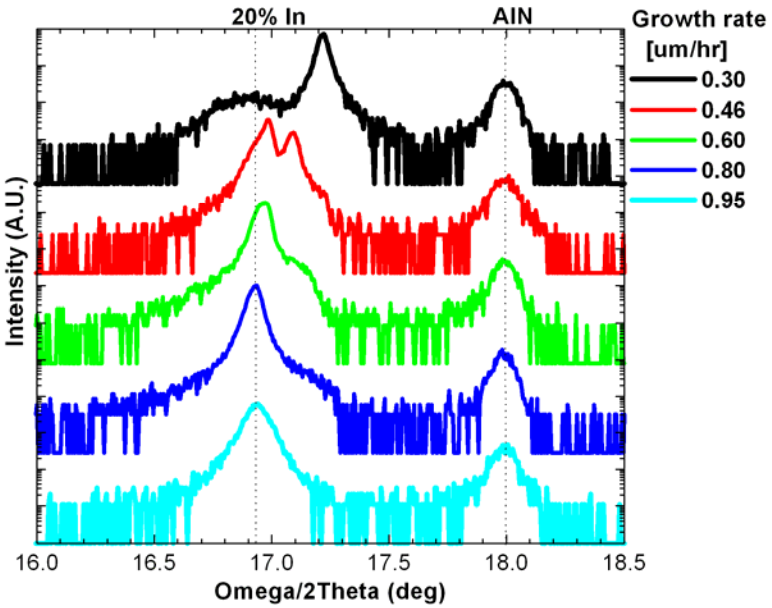

Figure 3.2 – X-ray diffraction data for MBE grown Si-doped $In_xGa_{1-x}N$ with compositional phase separation minimized with increasing growth rate.

3.1.1.2. Optical Measurements to Determine Absorption Coefficients

Originally it was speculated that thicker (> 1μm) $In_xGa_{1-x}N$, films similar to GaAs devices, would be desirable for $In_xGa_{1-x}N$ based solar cells. In principle, a thicker film would have a larger depletion volume, which would result in efficient drift field collection of current, reducing the impact of defects in the thin film. The absorption coefficient of the material determines the depth below the surface a photon can be absorbed and is one aspect of the needed depletion volume. Nanishi et al. [67] presented results from absorption and PL spectra on $In_xGa_{1-x}N$ samples varying in alloy composition from x = 0 to x = 1.0. The luminescence peak position and absorption edge roughly agree for all the samples over the entire alloy composition range. As was stated previously, for this work the $In_xGa_{1-x}N$ targeted a bandgap of 2.4 eV, equivalent to 27 % In incorporation, resulting in an approximate absorption coefficient of $< 0.5 \times 10^5$ cm^{-1}

based on the measurements by Nanishi et al. [67]. The following will present our results for the absorption coefficient for an $In_xGa_{1-x}N$ film with a bandgap of 2.4 eV.

PL and optical transmission measurements of four $In_xGa_{1-x}N$ grown samples on HVPE GaN templates, with film thickness of ~1 μm are shown in Figure 3.3. The PL measurements were taken at room temperature and the films were found to have single optical transition from ~ 2.1 – 2.9 eV for various In compositions. The In compositions were determined from XRD as 6, 23, 32, and 9 % for samples N2091, N2100, N2149, and N2154, respectively. Figure 3.3(b) shows the normalized optical transmission with a relatively sharp transition for lower In composition materials (N2091 and N2154) but slightly less sharp transition for higher In composition $In_xGa_{1-x}N$ (N2100 and N2149). The flat transition is caused by slight compositional phase separation related to the slow growth rate (~ 0.5 μm/hr) conditions used in these samples. The slow growth rate was used to amplify the impact of compositional phase separation on the optical absorption. The absorption edge becomes significantly less abrupt as compositional phase separation increases, which will impact the amount of photons absorbed in the material.

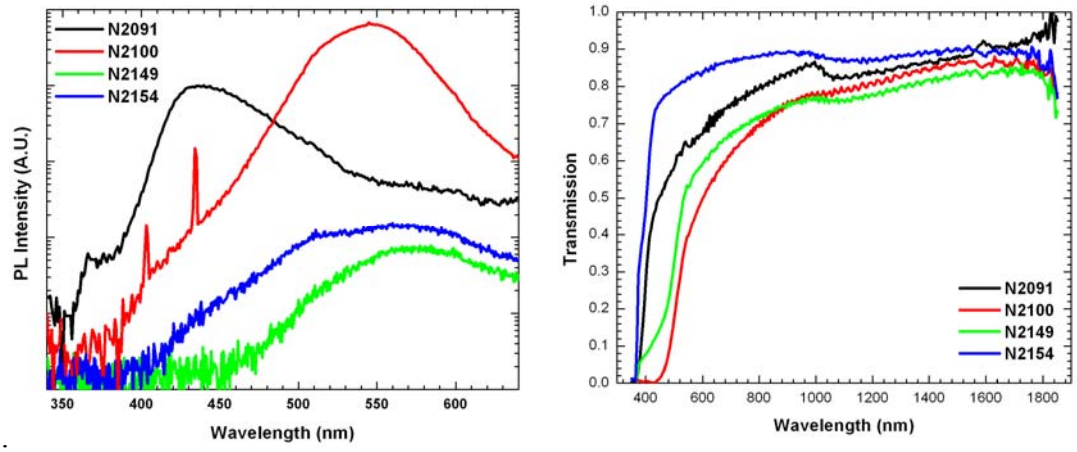

(a) **(b)**

Figure 3.3 – (a) Room temperature PL and (b) optical transmission of $In_xGa_{1-x}N$ samples for various In compositions. The In compositions are 6, 23, 32, and 9 % for samples N2091, N2100, N2149, and N2154, respectively. Note that samples N2091, N2100, and N2149 had slight compositional phase separation as measured in XRD.

The PL peak and the location of the optical transmission transition can be correlated to determine the approximate bandgap of the material. The transmission data is used to determine the absorption coefficient of $In_xGa_{1-x}N$ at 2.4 eV: $\alpha \cong 2 \times 10^5$ cm^{-1}, near the band edge. From these combined measurements and calculations, a net thickness of 100 nm will absorb 63 % of the 2.4 eV light at its band edge and a 500 nm thick $In_xGa_{1-x}N$ material will absorb 98 % of the same light. These high absorption characteristics make $In_xGa_{1-x}N$ a promising candidate for photovoltaics, even if long minority carrier diffusion lengths are not achieved. Additionally, this structure may result in higher open circuit voltages and reduced overall cost of the solar cell.

3.2. P-type $In_xGa_{1-x}N$ Limitations

As-grown InN has an exceptional propensity for n-type conductivity, because of native point defects in the film which act as donors. The native defects have been attributed to nitrogen vacancies in the InN lattice [22, 68]. The nitrogen vacancies compensate the material, which makes p-type doping extremely difficult. InN films also have an extreme electron accumulation at the surface which causes an inversion layer to form at the surface of the sample [58,69], making accurate conductivity measurements difficult.

The ability to dope a semiconductor material depends on the location of the conduction band and the valence band edges relative to the Fermi level stabilization energy (E_{FS}) [70]. The difficulties of efficient p-type doping in other III-N films is related to the low position of the valence band edge with respect to E_{FS}. InN and high In composition $In_xGa_{1-x}N$ p-type doping is exceedingly more difficult because the conduction band edge lies below E_{FS}. Figure 3.4 shows the bandgap diagram for the

complete $In_xGa_{1-x}N$ alloy composition showing the conduction band minimum (E_C), valence band maximum (E_V), and the mid-gap position (E_{mid}) [71]. The position of E_{FS} was determined from photoemission results for both undoped and Mg-doped alloys [Figure 3.4]. On the right-hand side of the diagram (InN), the conduction band is below the undoped and Mg-doped E_{FS}. Conversely, on the left-hand side of the diagram (GaN), the Mg-doped E_{FS} is located below the E_{mid} position.

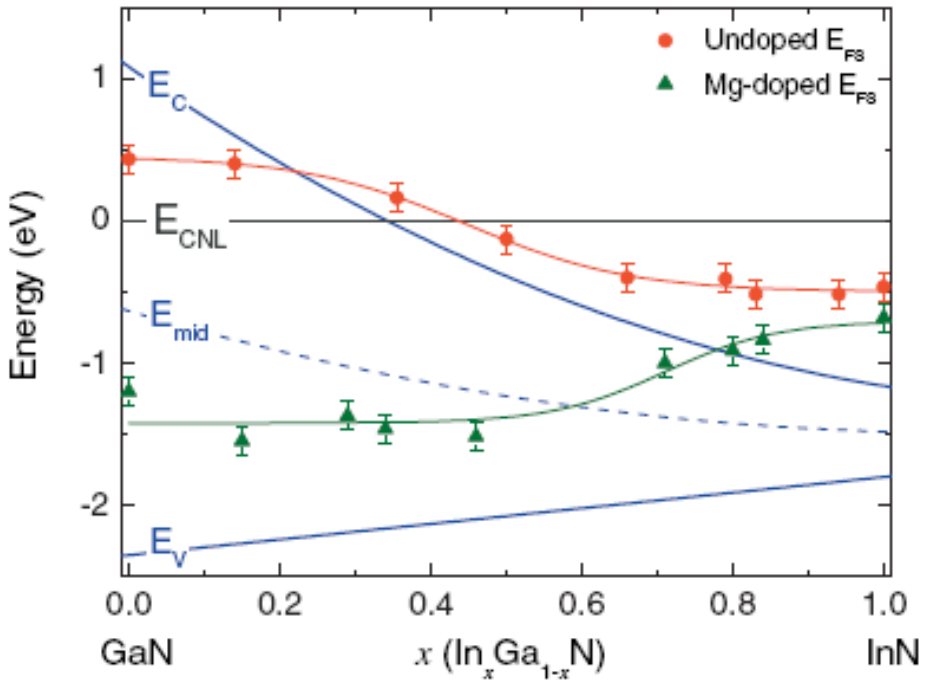

Figure 3.4 – Derived band diagram with respect to the charge neutrality level (E_{CNL}) as a function of $In_xGa_{1-x}N$ alloy composition [71].

The pinning of the surface Fermi level for the Mg-doped and undoped materials diverges with increasing Ga-content because of the different nature of the surface space charge regions for the different alloy and doping configurations [72]. Therefore, In-lean $In_xGa_{1-x}N$ will be easier to dope p-type [73]. Recently, p-type In-rich $In_xGa_{1-x}N$, up to 50% has been demonstrated for MOVPE grown films upon *ex-situ* annealing with hole concentrations in the range of $5 - 10 \times 10^{18}$ cm^{-3} and mobility of 1 -2 cm^2/Vs [74].

Initial research into $In_xGa_{1-x}N$ solar cells focused on $In_{0.30}Ga_{0.70}N$-GaN heterojunctions (P-n structures), primarily because of the limited ability to form p-type $In_xGa_{1-x}N$. Unfortunately, in this case, a polarization-induced discontinuity in the conduction-band edge and valance-band edge form, which negatively affects the photocurrent of the device by preventing minority carrier collection. Figure 3.5 shows an n-$In_{0.3}Ga_{0.7}N$/p-GaN device with discontinuities in the conduction and valence bands between the n-$In_xGa_{1-x}N$ and the p-GaN. The discontinuity prevents the collection of carriers (particularly holes) and negatively impact the device. The details of the device simulation and software used to create the band diagram are discussed in detail in Chapter 6.

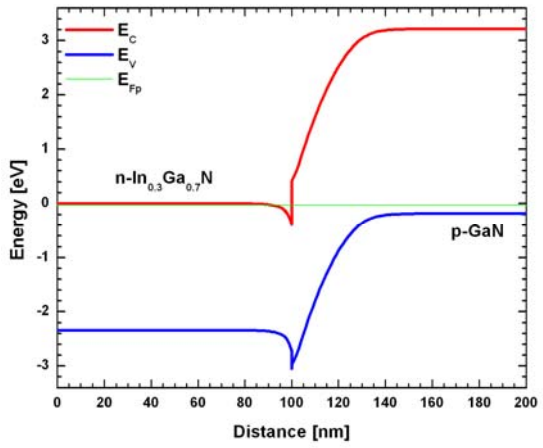

Figure 3.5 – Simulated band diagrams corresponding to a n-$In_{0.30}Ga_{0.70}N$/p-GaN solar cell.

Additionally, a heterojunction device will have defects arising from lattice mismatch, directly at the collection junction – the most sensitive region of the device. These solar results resulted in no photovoltaic response. P-type $In_xGa_{1-x}N$/n-type $In_xGa_{1-x}N$ homojunctions are therefore an attractive alternative. However, there currently remains a demonstrated limitation on p-type doping of $In_xGa_{1-x}N$ with high In composition.

Therefore, with present technology, an $In_xGa_{1-x}N$ homojunction solar cell has a limited bandgap range of just over 2.0 eV, until a breakthrough in p-type $In_xGa_{1-x}N$ is achieved.

The following section details two systematic studies of MME grown $In_xGa_{1-x}N$. Both studies included Mg doping and average N-rich growth conditions. The targeted In composition was 20 %, based on the band diagram in Figure 3.4, where the E_{FS} is below the E_{mid} position, $In_{0.2}Ga_{0.8}N$ should be able to be doped p-type. Section 3.3 details the effects of large Mg flux (10^{-8} torr BEP), conversely Section 3.4 investigates low Mg flux (10^{-10} torr BEP).

3.3. Effects of Large Mg flux in Mg-doped $In_xGa_{1-x}N$

This section presents *in-situ* development of zinc-blende phase Mg-doped $In_xGa_{1-x}N$ by MBE. The films were grown using an RF-plasma nitrogen source and characterized by *in-situ* RHEED and *ex-situ* XRD. The presence of Mg dopant during growth leads to the crystallization of zinc-blende $In_xG_{1-x}N$, whereas similar undoped and Si-doped $In_xG_{1-x}N$ remains wurtzite.

3.3.1. Crystallographic Structure

III-nitrides have been predominately grown in a thermodynamic stable wurtzite crystal configuration. They have also been grown as a metastable zinc-blende crystal structure albeit on zinc-blende substrates such as GaAs (001) and 3C-SiC (001). The predominate difference between wurtzite and zinc-blende phase materials is a 120° rotation in the stacking sequence, which can be induced by impurities [75, 76, 77]. Zinc-blende nitrides have a lower energy bandgap (200meV) then their wurtzite complement, are expected to have better electrical properties [78] because of reduced phonon scattering in the higher crystallographic symmetry case, and have smaller effective masses [79].

The crystallographic structure of zinc-blende and wurtzite GaN structures vary in an altered stacking sequence of identical closely packed atomic planes. As an example, zinc-blende GaN stacking sequence is ABCABC and wurtzite stacking sequence is ABAB. Studies have shown that mixed phase zinc-blende/wurtzite material is related to three possible mechanisms: defects in the material predominately from crystal lattice mismatch between the epilayer and the substrate [80], impurity induced stacking faults [75, 76], and low growth temperatures [81]. Munkholm et al.[80] found that the

predominant crystal defects were in-plane stacking faults, resulting in a mixed zinc-blende/wurtzite. Additionally, the presence of Mg may induce the transition from wurtzite to zinc-blende phase material as described by Sarigiannidou et al. [82]. The authors found that Mg incorporates substitutionally into the GaN lattice inhibiting the formation of the Ga bilayer. For N-face GaN the presence of Mg atoms induces the synthesis of zinc-blende GaN as shown in TEM images of a Mg-doped GaN growth on 4H-SiC.

3.3.2. Growth Conditions and Analysis

The $In_xG_{1-x}N$ films were heteroepitaxially grown on 3 – 12 μm-thick HVPE grown GaN:Si/Al_2O_3 in a Riber 32 MBE system. The substrate temperature ranged from 515 to 550 °C. An EPI-unibulb nitrogen plasma source operated at 350 W and a flow rate of 0.50 sccm was used. Mg doping was delivered by a valved Mg cracker set to 65 mils, with bulk and cracker temperatures of 360 °C and 900 °C, respectively, resulting in a flux of ~ 3×10^{-8} torr. Si doping was obtained at a cell temperature of 1020 °C, leading to an electron concentration of 10^{20} cm^{-3}.

Prior to the $In_xG_{1-x}N$ growth, a 0.6 μm-thick GaN:Si buffer was grown at a substrate temperature of 600 °C using a modulation technique (10 seconds of Ga and Si shutters open followed by 10 seconds of Ga and Si shutters closed [83]) to maintain a streaky RHEED pattern, and in some cases achieving a 2×2 reconstruction pattern, indicative of an atomically smooth surface rarely observed in GaN growth

Figure 3.6 shows the progression of RHEED (bare wafer, one hour into $In_xGa_{1-x}N$, and at the end of $In_xGa_{1-x}N$) during Mg-doped and Si-doped growths. It can clearly be

seen in Figure 3.6(a) that the HVPE GaN:Si substrate has a single phase pattern, indicative of wurtzite GaN. Figure 3.6(b) is a spotty pattern of Mg-doped $In_xGa_{1-x}N$ one hour into the growth, showing the transition from streaky to spotty and indicating three-dimensional growth. Finally in Figure 3.6(c), at the end of a two hour growth, there is a mixture of bright crystalline equally spaced wurtzite spots and dim zinc-blende spots. These images of mixed zinc-blende and wurtzite phases are in agreement with the conclusion that wurtzite and zinc-blende phases of GaN can coexist on the surface, as observed by Kuznetsov et al. [84] and Namkoong et al. [75, 76].

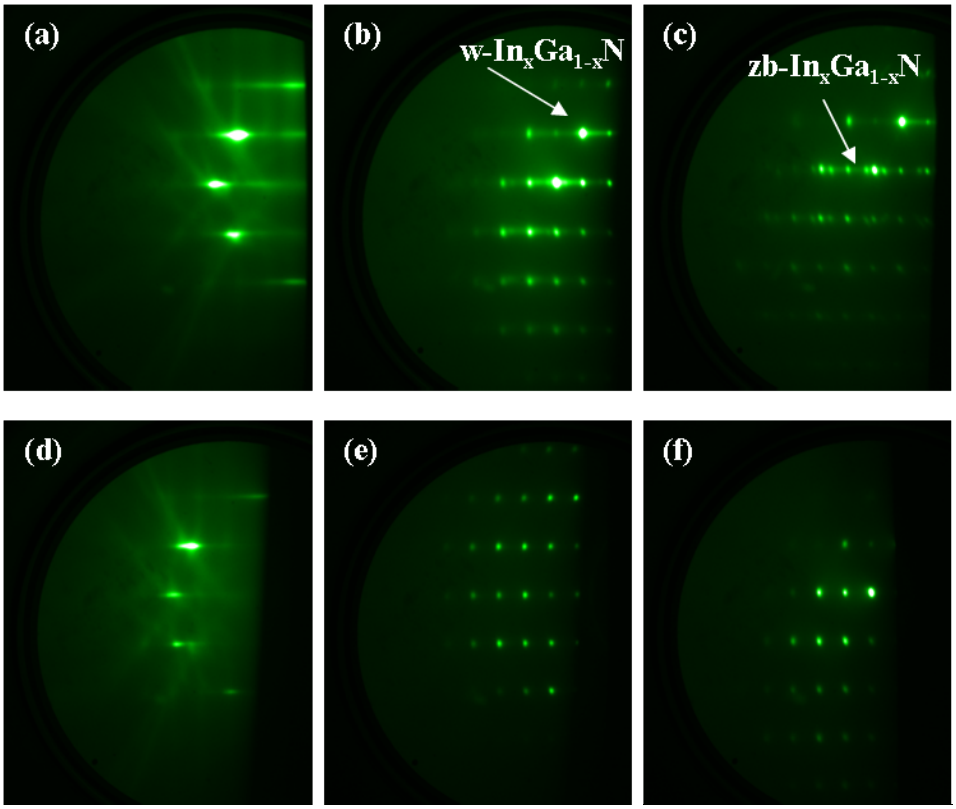

Figure 3.6 – RHEEID of $In_xGa_{1-x}N$: (a) Mg at the beginning of growth, (b) Mg-doped half-way into growth, (c) Mg-doped at the end of growth, (d) Si-doped at the beginning of growth, (e) Si-doped half-way into growth, and (f) Si-doped at the end of growth.

Similarly, in Figure 3.6(d) – (f), the HVPE GaN:Si is streaky, one hour into Si-doped $In_xG_{1-x}N$ the pattern is spotty, and the end of the two hour Si-doped $In_xGa_{1-x}N$ growth

shows single phase spots. The single phase spots indicate a nonplanar growth surface of single phase material.

XRD pole-figures were measured to confirm the results from the RHEED images on Mg- and Si-doped $In_xGa_{1-x}N$ as shown in Figure 3.7(a) and (b), respectively. The peaks labeled "I" are associated with the combination of the Al_2O_3 substrate peak and {20-21} wurtzite $In_xGa_{1-x}N$, the peaks "II" are{11-22} wurtzite $In_xGa_{1-x}N$, and the peaks "III" are the zinc-blende {311} $In_xGa_{1-x}N$. In the Mg-doped pole-figure the {11-22} and {311} $In_xGa_{1-x}N$ are rotationally in phase. The {11-22} $In_xGa_{1-x}N$ is rotated 30° out of phase with the combination of the Al_2O_3 substrate and {20-21} $In_xGa_{1-x}N$ and {311} $In_xGa_{1-x}N$. For the Si-doped pole-figure, the {11-22} $In_xGa_{1-x}N$ is also rotated 30° out of phase with the combination of Al_2O_3 substrate and {20-21} $In_xGa_{1-x}N$. The contribution from {311} zinc-blende phase material was not found for Si-doped $In_xGa_{1-x}N$. The pole-figures confirm the results from *in-situ* RHEED growth monitoring showing Mg-doped $In_xGa_{1-x}N$ has a mixed zinc-blende/wurtzite crystalline structure, whereas Si-doped $In_xGa_{1-x}N$ is only wurtzite phase. The pole-figure of a bare GaN:Si HVPE substrate did not show evidence of zinc-blende material.

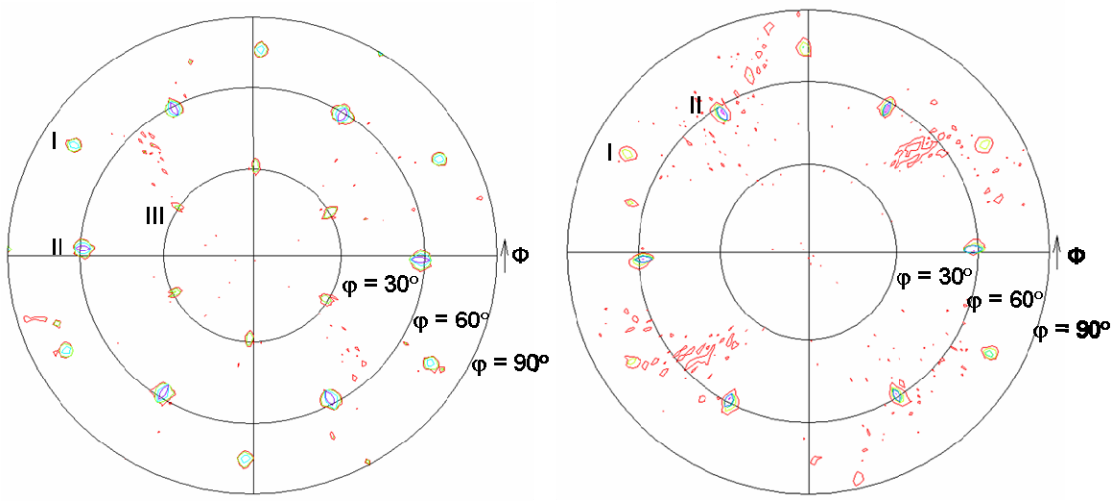

Figure 3.7 – Pole-figure of (a) $In_xGa_{1-x}N$:Mg/GaN:Si/Al_2O_3 and (b) $In_xGa_{1-x}N$:Si/GaN:Si/Al_2O_3 with peaks labeled : I – mixture of wurtzite {20-21} $In_xGa_{1-x}N$ and the Al_2O_3 substrate peaks, II – wurtzite {11-22} $In_xGa_{1-x}N$ peaks, and III – zinc-blende {311} $In_xGa_{1-x}N$. ϕ is the angle relative to the normal surface.

A possible cause for the appearance of zinc-blende phase material in Mg-doped $In_xGa_{1-x}N$ is the presence of stacking faults in the wurtzite lattice. The stacking faults are most likely caused by an impurity present on the growing surface, likely Mg, which is known to segregate to the surface [84]. It has also been shown that excessive Mg present during Mg-doped GaN growth, is associated with the formation of extended defects as evidenced by TEM micrographs [85, 86, 87]. Any defects in the epitaxial material can deteriorate the electronic and structural properties of the material. Therefore, the mixed phases found in our Mg-doped material may have been the cause of previous poor electrical results (not presented here).

ω-2θ XRD of the samples presented in Figure 3.7 is shown in Figure 3.8, with the Mg-doped sample in blue and undoped in red. The Mg-doped sample shows two different In compositions determined from Vegard's law as 11 % and 18 % and the undoped sample shows a single In compositions of 8 %. The growth conditions were

kept constant, therefore the multiple $In_xGa_{1-x}N$ peaks in the Mg-doped sample can be attributed to structural phase separation caused by the presence of the large (3×10^{-8} torr BEP) Mg flux.

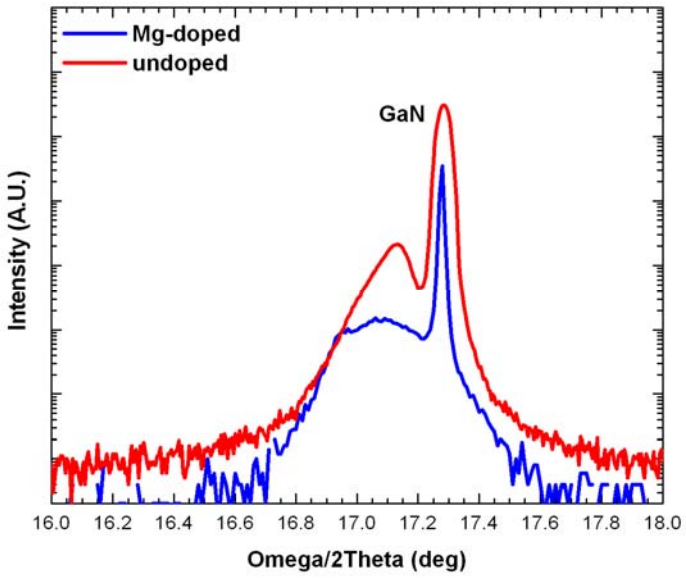

Figure 3.8 – ω-2θ XRD of $In_xGa_{1-x}N$ with x = 11% and 18% located at ω = 17.09° and 16.97° for Mg-doped (blue line), respectively. x = 8% located at ω = 17.14° for undoped (red line), respectively.

We have observed the mixture of zinc-blende and wurtzite crystalline structures for Mg-doped $In_xGa_{1-x}N$ where the zinc-blende material induces structural phase separation. Similar growth conditions for unintentionally doped and Si-doped $In_xGa_{1-x}N$ remained wurtzite. *In-situ* RHEED images show the mixture of zinc-blende and wurtzite phase material and XRD pole-figures and reciprocal space maps confirm the presences of zinc-blende material in Mg-doped $In_xGa_{1-x}N$. Further Mg-doped $In_xGa_{1-x}N$ will use RHEED analysis as a guide to eliminate the zinc-blende inclusions by reducing the Mg flux.

3.4. Effects of Low Mg Flux in Mg-doped $In_xGa_{1-x}N$

The previous section proved that large Mg flux of ~ 3×10^{-8} torr BEP resulted in structural phase separation evidenced in RHEED images and XRD pole-figure scans. In the following section, the effects of various low Mg fluxes (10^{-10} torr BEP range) at a targeted In composition of 20 % are studied.

3.4.1. Growth Conditions and Structural Analysis

A Riber 32 system with standard effusion cells for Ga, Al, In, and Mg was used with the substrate maintained at 450 °C, Ga flux of $1.86 – 3.72 \times 10^{-7}$ torr BEP, In flux of $8.0 \times 10^{-8} – 1.6 \times 10^{-7}$ torr BEP, and Mg flux of $0.5 – 4.0 \times 10^{-10}$ torr BEP (Note that for this study, a standard effusion cell was used for the Mg dopant and was set to 135 – 165 °C to achieve the fluxes previously mentioned). MME was used for all epitaxial layers, with constant 10 seconds shutter open / 10 seconds shutter closed cycles. All samples were grown on Al_2O_3 substrates with GaN/AlN buffer layers; details of the buffer layers can be found in Appendix B.

Figure 3.9 shows pole-figures from a Mg-doped (Mg flux equal to 2×10^{-10} torr BEP) $In_xGa_{1-x}N$ and an undoped $In_xGa_{1-x}N$ sample. Both samples have the same four peaks, two of which are the same peaks in Figure 3.7: the combination of the Al_2O_3 substrate peaks and {20-21} wurtzite $In_xGa_{1-x}N$ peaks and {11-22} wurtzite $In_xGa_{1-x}N$ peaks, labeled "I" and "II," respectively. The peaks labeled "V" are the {21-34} Al_2O_3 substrate peaks. The peaks labeled "IV" have six fold symmetry and are located at $\psi \cong 34$ °. The {311} zinc-blend peaks found in Figure 3.7 are located at $\psi \cong 29$ °, therefore there is a

$\Delta\psi \cong 5\ °$ between the "high" Mg flux study in Section 3.3 and the "low" Mg flux study in this section.

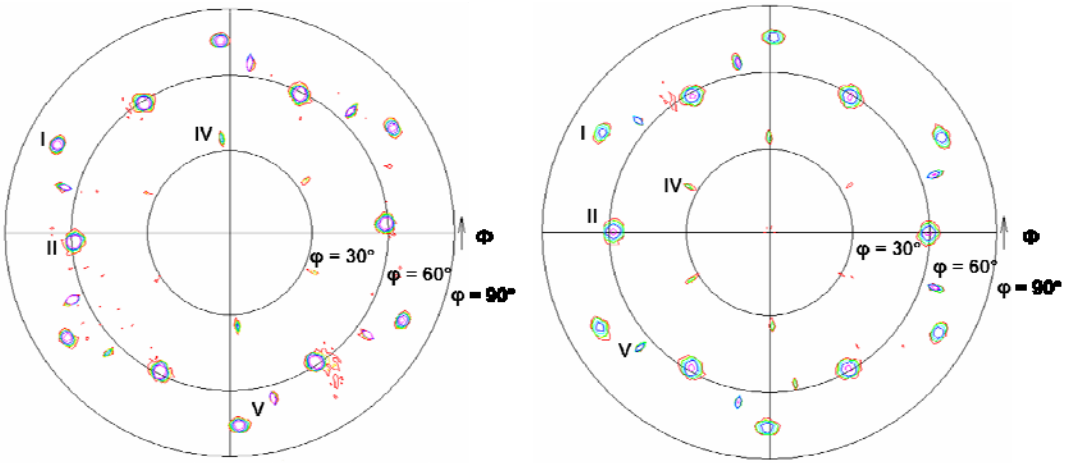

(a) **(b)**

Figure 3.9 – Pole-figure of (a) Mg-doped $In_xGa_{1-x}N$ with flux Mg flux equal to 2×10^{-10} torr BEP and (b) an undoped $In_xGa_{1-x}N$. Both samples have the mixture of wurtzite {20-21} $In_xGa_{1-x}N$ and the Al_2O_3 substrate peaks and wurtzite {11-22} $In_xGa_{1-x}N$ peaks and, labeled I and II, respectively. The {21-34} Al_2O_3 substrate peak is labeled V. Both samples also have peaks with six fold symmetry located at $\psi = 34°$ IV. ϕ is the angle relative to the normal surface.

The peaks labeled IV were found in multiple $In_xGa_{1-x}N$ samples regardless of doping and all samples had a $\psi \cong 34\ °$. A deformation in ψ would affect all the zinc-blende and wurtzite material, shifting peaks I, II, and V in ψ. This is not the case, as the mixture of wurtzite of {20-21} $In_xGa_{1-x}N$ and the Al_2O_3 substrate peak labeled I in Figure 3.7 and Figure 3.9 all have the same $\psi \cong 74\ °$. Therefore, it was concluded that the peaks at $\psi \cong 34\ °$ are related to the {10-13} wurtzite reflection in the crystal, as proven below.

Figure 3.10 shows the ω-2θ scan optimized on the {11-29} Al_2O_3 reflection for various $In_xGa_{1-x}N$ growth conditions: high Mg flux (10^{-8} torr BEP) in black (sample shown in Figure 3.7(a)) , Si-doped in red (sample shown in Figure 3.7(b)), and low Mg flux (10^{-10} torr BEP) in green (sample shown in Figure 3.9(a). The dotted lines indicate the position of the {311} zinc-blende GaN, the {10-13} wurtzite AlN, and the {10-13}

wurtzite GaN. In Figure 3.10(a), the high Mg doping case shows a zinc-blende $In_xGa_{1-x}N$ peak centered at ω = 34.50 ° (just to the left of the zinc-blende GaN label) and no zinc-blende peaks for the Si-doped or low Mg-doped. The wurtzite {10-13} and zinc-blende {311} have similar ψ position, ~ 32 ° and ~ 29 °.

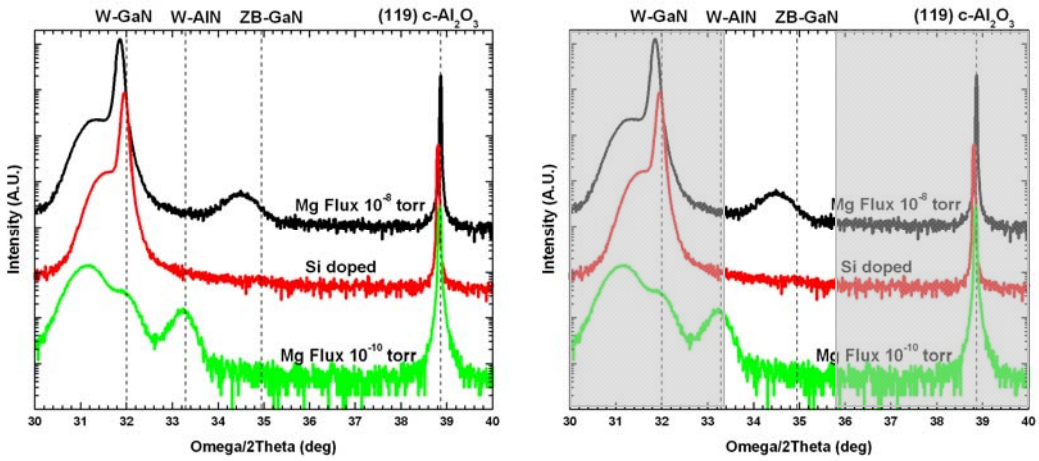

Figure 3.10 – (a) XRD ω-2θ scan optimized on the {11-29} Al_2O_3 peak for various $In_xGa_{1-x}N$ growth conditions: high Mg flux (10^{-8} torr BEP) in black, Si-doped in red, and low Mg flux (10^{-10} torr BEP) in green. The dotted lines indicate the position of {311} zinc-blende GaN, the {10-13} wurtzite AlN, and {10-13} wurtzite GaN. (b) is the ω-2θ window used in the pole-figure in Figure 3.9, showing that part of the {10-13} wurtzite AlN peak was sampled.

Figure 3.10(b) shows the ω-2θ sampling window (highlighted area) used in the pole-figures. The high Mg flux sample has a broad {311} zinc-blende $In_xGa_{1-x}N$ peak and no zinc-blende contribution in the Si-doped and low Mg flux sample. The sample space in the low Mg flux sample has partial contribution from the {10-13} wurtzite AlN peak. Therefore, the peaks at ψ ≅ 34 ° in Figure 3.9 are related to the {10-13} wurtzite AlN peak and not a zinc-blende material. Therefore, the low Mg flux does not create zinc-blende material. Furthermore, we have identified a routine methodology for detecting zinc-blende materials using widely available XRD tools. Details of XRD procedure used in this experiment can be found in Appendix C.

3.4.2. Electrical Analysis

As was stated previously, InN and high In content $In_xGa_{1-x}N$ have high surface charge density that complicates electrical measurements of the underlying bulk layers, obscuring p-type conductivity [88]. $In_xGa_{1-x}N$ grown with the MME technique targeting 20 % In, did result in all the samples having p-type conductivity as measured by thermal probe, but because of the high surface charge density only one sample measured p-type conductivity by Hall effect measurements (denoted by a *). The resistivity results are shown in Figure 3.11. The p-type $In_xGa_{1-x}N$ had a hole concentration of 2.07×10^{16} cm^{-3}, resistivity of 138 Ω-cm, and mobility of 2.94 cm^2/Vs. The dotted lines are only to guide the eye.

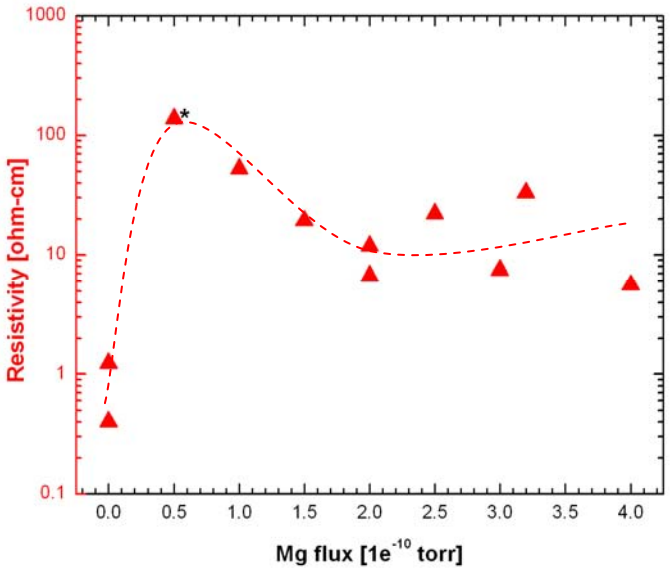

Figure 3.11 – Results from MME Mg-doped $In_xGa_{1-x}N$ with a fixed duty cycle of 10 seconds open / 10 seconds closed. (a) All samples measured p-type by thermal probe, but the only sample with p-type conductivity from Hall measurements is labeled with a *. All other samples had mixed conductivity. Dotted lines are to guide the eye.

Ideally, the resistivity starts at a nominally low value for n-type material and as the Mg flux increases, the resistivity will increase, become partially compensated (remaining n-type). The resistivity reaches a maximum and then decreases becoming more

conductive (becoming p-type) with increasing Mg flux. As the Mg flux continues to increase the resistivity will increase again, becoming overly compensated (the dopant creates defects in the material.) This general behavior is visualized in the resistivity data in Figure 3.11(a), where the maximum resistivity sample is the only sample that measured p-type by Hall effect measurements.

The outstanding hole concentration results that will be presented in Chapter 4 for p-GaN and device simulation results in Chapter 6, prove that further investigations into p-type doping of $In_xGa_{1-x}N$ is unnecessary for this work and will be left for the future work section of Chapter 8.

3.5. Summary

A successfully $In_xGa_{1-x}N$ solar cell requires the understanding of various growth parameters and knowledge of specific material properties, such as absorption coefficients. Using high growth rates, $In_xGa_{1-x}N$ films with In compositions ranging from 1 to 32 % have been grown by MBE with negligible compositional phase separation according to XRD analysis, and better than 190 arcsec ω-2θ FWHM for a ~0.6 μm thick $In_{0.32}Ga_{0.68}N$ film. Using measured transmission data, the absorption coefficient of $In_xGa_{1-x}N$ at 2.4 eV was calculated as $\alpha \cong 2 \times 10^5$ cm^{-1} near the band edge. This absorption coefficient limits the optimal solar cell thickness to less than a micron and may lead to high open circuit voltage while reducing the constraints on limited minority carrier lifetimes.

$In_xGa_{1-x}N$ epitaxial growth on HVPE GaN:Si substrates found that high levels of Mg-doping leads to the formation of zinc-blende phase material for Mg flux equal to $\sim 3 \times 10^{-8}$ torr BEP. Mg-doped $In_xGa_{1-x}N$ films grown on Al_2O_3 substrates with a lower Mg flux of $\sim 10^{-10}$ torr BEP did not show the same zinc-blende phase material. Si-doped and

undoped $In_xGa_{1-x}N$ also did not show this zinc-blende transition. A Mg flux of 0.5×10^{-10} torr BEP resulted in a p-type $In_xGa_{1-x}N$ sample, with a hole concentration of 2.07×10^{16} cm^{-3}, resistivity of 138 Ω-cm, and mobility of 2.94 cm^2/Vs.

CHAPTER 4: Metal Modulation Epitaxy Growth of Doped GaN

The ability to achieve high quality repeatable p-type GaN films is necessary for the continued advancement of III-Nitride based devices, such as light emitting diodes (LEDs), lasers, heterojunction bipolar transistors (HBTs), and solar cells. Mg has proven to be the most successful p-type dopant. Unfortunately, Mg-doped nitride based devices have had limited performance in part because of highly resistive p-type layers resulting from low hole mobilities, hole concentrations limited to ~10^{18} cm^{-3}, and the large acceptor activation energy of Mg atoms ~ 160 – 170 meV [89, 90, 91]. Specifically, HBTs are presently not viable in part because of these limitations while others, such as LEDs and lasers have reduced performance because of reduced hole injection. III-N solar cells are presently limited to single junctions because of the unavailability of tunnel junctions which necessitate degenerate p-type doping. The goal of this work is to demonstrate that by addressing all of these factors simultaneously, improvements in hole concentration in GaN can be achieved.

Recently, Metal Modulation Epitaxy (MME) [83] was introduced as a new growth technique wherein only the metal fluxes (Al, Ga, In, Si, and Mg) are modulated in a short periodic fashion in a plasma-assisted MBE system, while maintaining a continuous nitrogen plasma flux. This lead to dramatic improvements in grain size and demonstrated hole concentrations in excess of 4.5×10^{18} cm^{-3} [83, 92, 93, 94] for Mg-doped GaN.

GaN growth has a well documented surface phase diagram for a range of growth conditions [95] with three distinct growth regimes: Ga-droplet formation, N-rich, and an

intermediate regime. Figure 4.1 shows an adapted GaN surface phase diagram, extrapolated to the lower temperatures used in this work. Predominately, growth is conducted in Ga-droplet or intermediate regime where a constant metal bilayer prevents the formation of pits resultant from threading dislocations. The MME approach, when applied to higher temperatures or in a predominantly droplet rich regime, results in atomically smooth surfaces normally only found when growing in the Ga-droplet regime. However, MME does not allow droplets to accumulate, making it viable for devices that traditionally depend on smooth droplet free interfaces. The influence of growth regimes on electron and hole concentrations will be discussed in the sections that follow.

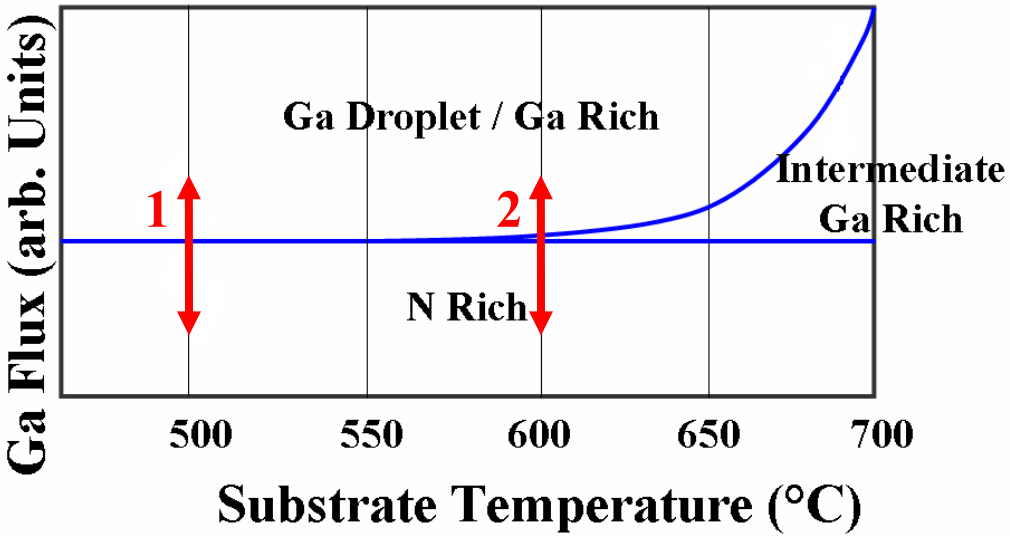

Figure 4.1 – Adapted GaN surface phase diagram, extrapolated to lower temperatures. The red arrow labeled 1 indicates the growth regime used in Study A and B. The red arrow labeled 2 indicated the growth regime used in Study C [95].

4.1. Systematic Study of Mg-doped GaN

Additional challenges that Mg-doped GaN faces include incorporation that is strongly dependent on III-V ratio, compensation of acceptors by defects, polarity inversion domains that limit the upper solubility of Mg, and reactor memory and high diffusivity, resulting in diffused profiles of Mg that facilitates surface segregation.

Bhattacharyya et al. [96] obtained hole concentrations on *c*-plane GaN of 3×10^{18} cm^{-3} and resistivity of 0.3 Ω-cm with high Ga fluxes (1.3×10^{-6} torr BEP), high substrate temperatures (~770 °C), and high Mg fluxes (1.5×10^{-8} - 1.5×10^{-7} torr BEP). The authors state that Mg incorporates more effectively with extreme Ga-rich conditions resulting from the dissolution of Mg in the Ga film which increases Mg sticking coefficient. *m*-plane oriented Mg-doped GaN has achieved hole concentrations of ~7.51×10^{18} cm^{-3}, because of the absence of inversion domains normally observed in highly doped Mg-doped *c*-plane films [97].

Recently, Burnham et al. [47, 83] reported an increase of Mg doping concentration and repeatability in GaN films using the MME technique. The authors modulate the Ga and Mg shutters with a constant duty cycle, achieving hole concentrations of 2.2×10^{17} to 4.6×10^{18} cm^{-3} and Hall mobilities of 9.7 and 1.1 cm^2/V-s, respectively. Simon et al. [98] also recently studied the effect of III/V ratio as related to resistivity of Mg-doped GaN using substrate temperatures of 600 °C and Ga flux ranging from $1.30 – 1.71 \times 10^{-7}$ torr BEP, which corresponded to a change from N-rich conditions to Ga-rich conditions. They discovered that Ga-rich conditions are necessary for highly conductive p-type layers, but Ga-rich conditions may lead to higher leakage current, detrimental to vertically conducting devices. It was recommended that vertical devices employ a modulation of Ga and or N_2 fluxes to prevent leakage while maintaining high p-type conductivity. Enforcing the idea, that MME will be a beneficial technique for nitride based devices.

Another key aspect of the MME approach for Mg-doping is the use of sufficiently low substrate temperatures where an abrupt transition is available between Ga-droplet

and N-rich conditions without an intermediate phase. The low substrate temperature insures that transitions from Ga-rich/droplet to N-rich phases are abrupt and the bilayer/monolayer phase is thermodynamically unstable. Under these conditions, the Ga bilayer is either in the process of building up or depleting and cannot be sustained without the addition of droplets. At the low substrate temperatures, the consumption of the Mg-saturated Ga bilayers and droplets only occurs through growth of the GaN film as Ga desorption is minimized. Desorption mass spectroscopy analysis verifies this feature [102].

This work reports on the repeatability of high hole concentration Mg-doped GaN films, using the MME technique developed at Georgia Institute of Technology [99] and in an uncommon growth regime. A comprehensive, systematic, and repeatable study was conducted to determine how variations in the III/V ratio with constant modulation duty cycle, constant Mg fluxes, and growth temperature effect the hole carrier concentration, resistivity, and film quality. Conversely, the effects of the modulation scheme on the hole carrier concentration, resistivity, and film quality was conducted.

4.1.1. Growth Conditions and Analysis

All samples used in this study were grown on c-plane Al_2O_3 substrates prepared using the techniques outlined in Appendix B. The samples were loaded into the introductory chamber of a Riber 32 MBE system and outgassed for one hour at 300 °C. The samples then under went a nitridation process at 300 °C for 30 minutes, followed by a low temperature AlN buffer at 700 °C, Al flux of 4.9×10^{-7} torr BEP, with a fixed MME scheme of 10 seconds open / 10 seconds closed. A Veeco-unibulb nitrogen source operated at 350 W and a flow rate of 1.2 – 1.3 sccm was used throughout the growth.

Study A was conducted in a Riber 32 system with standard effusion cells for Ga, Al, and Mg. The substrate was maintained at 500 °C, Ga flux of $4.5 – 6.0 \times 10^{-7}$ torr BEP, and Mg flux of $1.0 – 3.2 \times 10^{-10}$ torr BEP were used. Using the MME technique, the Ga and Mg shutters were modulated with a fixed duty cycle of 10 seconds open followed by 10 seconds closed while maintaining a constant nitrogen flux.

Study B and C were conducted in a similar Riber 32 system with a standard effusion cell for Al, a SUMO effusion cell for Ga, and a Veeco corrosive series valved cracker for Mg [100]. The substrate was maintained at 500 and 600 °C and Ga flux varied from $3.0 \times 10^{-7} – 1.0 \times 10^{-6}$ torr BEP. The Mg cracker bulk and tip were maintained at 300 °C and 900 °C, respectively with the valve position set open at 120 mils. Again the MME technique was used in Study B and C, with various modulation schemes.

All of the as-grown layers were characterized by room temperature Hall measurements with Van der Pauw geometry using In ohmic contacts and by X-ray diffraction (XRD) using a Philips X'Pert MRD. The samples were grown in a random matrix to rule out memory effects related to residual Mg in the growth chamber [101].

During the Mg-doped GaN growth, the Ga and Mg shutters were modulated with a fix duty cycle alternating between Ga-droplet and N-rich conditions. As mentioned previously, low substrate temperatures were used in all studies (500 – 600 °C) where there is no intermediate regime. Growth conducted in the intermediate regime results in atomically smooth surface regions, but normally has deep pits, where the density of pits is inversely related to how close the growth parameters are to the droplet regime. Growth in the intermediate regime prevents the accumulation of droplets, making it a viable

growth regime for devices that depend on smooth droplet free interfaces. In our study, along with low substrate temperatures of 500 - 600 °C, the Ga flux was sufficiently large (up to 3× the stoichiometric Ga flux) that droplets rapidly form when the shutter was opened and are subsequently consumed upon shutter closed. When the metal shutters are closed, leading to N-rich conditions, the Mg atoms preferentially incorporate on the desired Ga substitutional site, but faceting can result. Oscillating to Ga-rich conditions, smoothes the surface and eliminates faceting. As will be demonstrated, this growth technique has lead to the highest hole concentration values in the literature.

RHEED images during growth show elongated streaky spots, confirming a net N-rich average growth condition, as shown in Figure 4.2.

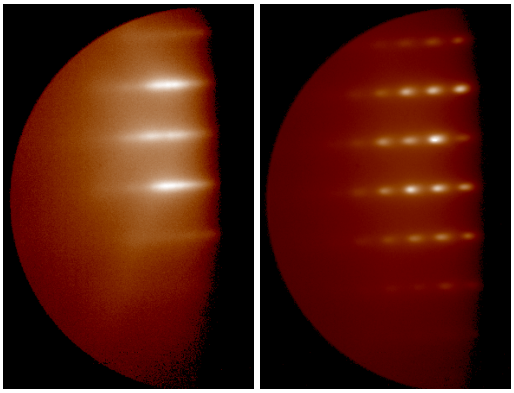

(a) **(b)**

Figure 4.2 – RHEED of: (a) AlN buffer immediately before the Mg-GaN growth and (b) Mg-doped GaN at the end of growth.

Figure 4.2(a) shows a the streaky surface of the AlN buffer, immediately before the start of Mg-doped GaN growth, while Figure 4.2(b) is at the end of the 40 minute Mg-doped GaN growth, showing elongated streaky spots. Unlike traditional N-rich growth, the RHEED spots are still connected by faint streaks, indicative of a minimally faceted surface. These streaks connecting the spots remain even though the N-rich average Ga dose growths are relatively thick, 0.46 μm, and therefore would normally have ample

time to completely facet. Therefore, the Ga-droplet rich part of the MME cycle is effective in minimizing the faceting, normally occurring in N-rich GaN growth. Since Mg incorporates on Ga sites most effectively on N-rich surfaces, the hole concentration increases for N-rich growth, but the Ga-rich MME cycle reduces the compensating defect density.

Study A initially looked at the effects of various Mg fluxes as related to different Ga fluxes. Communications with Simon et al. [98] suggested that the Mg flux should be significantly lower, 10^{-10} torr BEP as opposed to $10^{-7} – 10^{-8}$ torr BEP used in the literature [47, 83, 96]. Chapter 3, also demonstrated the beneficial effects of the lower Mg flux for $In_xGa_{1-x}N$. In this case, the modulation was kept constant at 10 second shutter open / 10 seconds shutter closed. The results of Study A are shown in Figure 4.3(a) with the square shapes indicating Hall concentration and triangle shapes indicating film resistivity. The dotted lines are only to guide the eye.

The left most point in Figure 4.3(a) indicates the normal doping range found in the literature, hole concentration in the high 10^{17} cm^{-3} range and resistivity ~ 1 Ω-cm. As the Mg flux increases beyond 2.4×10^{-10} torr, in the present case, the resistivity initially increases then decreases, indicating the onset of defect creation while the Hall mobility only increases [100]. We were able to achieve hole carrier concentration of 5.1×10^{18} cm^{-3}, with corresponding resistivity of 4.2 Ω-cm and mobility of 0.33 cm^2/V-s, slightly larger than what was reported by Burnham et al. [47].

Figure 4.3(b) includes the crystalline quality of the film by looking at the XRD ω (0002) and ω (10-2) full width half maximum (FWHM). As the Mg flux increases, the film quality degrades, resulting in higher FWHM values. Demonstrating, that the Mg

dopant is creating compensated defects in the film. Also, for each of the three Ga fluxes investigated, once the Mg flux exceeded 3.2×10^{-10} torr BEP, the conductivity of the film became mixed (denoted by *) as evidenced by room temperature Hall measurements. All of the samples did measured p-type by thermal probe.

Based on these initial results, we concluded that the Mg flux does impact the hole concentration, Mg flux of $\sim 2.5 \times 10^{-10}$ torr BEP leads to higher hole concentration Mg-doped GaN. This information was used as a starting point for the following studies (B and C) where a Mg valve cracker was implemented in a different MBE system.

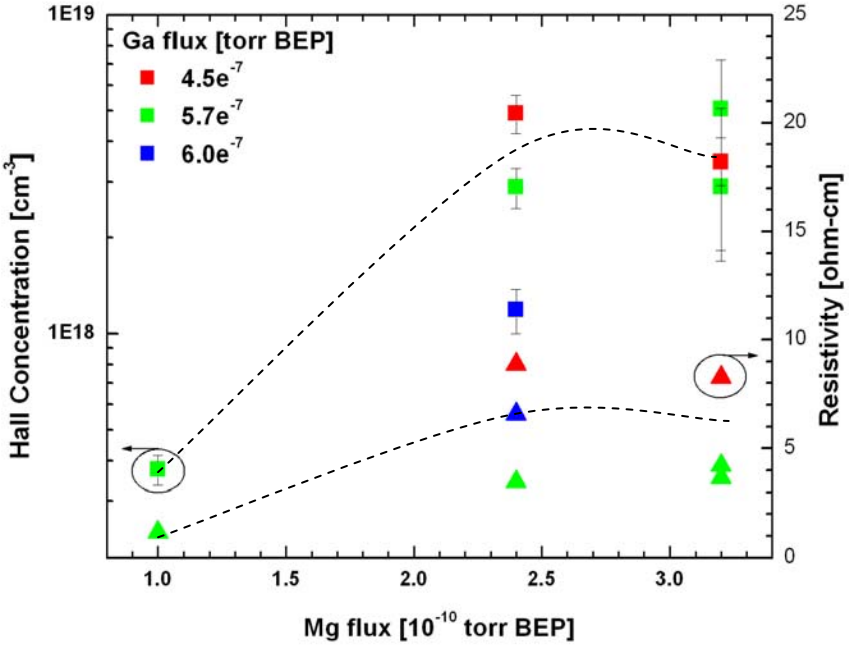

(a)

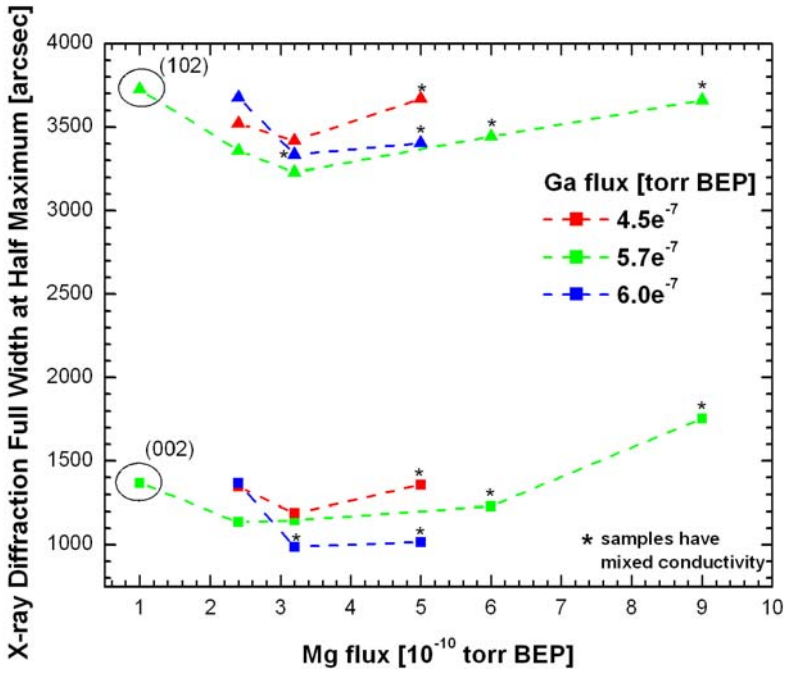

(b)

Figure 4.3 – Results from Study A of Mg-doped GaN for a fixed duty cycle of 10 seconds open/10 seconds closed with various Ga and Mg fluxes. (a) Hall concentration is denoted by squares and resistivity is denoted by triangles. (b) XRD FWHM film quality for symmetric ω (0002) and asymmetric ω (10-2) reflections denoted by squares and triangles, respectively. The * denotes films that measured p-type on thermal probe, but had mixed Hall conductivity

4.1.1.1.Hall and XRD Results

Study B focused on varying the Ga flux and modulation scheme while maintaining a constant Mg flux ~ 4×10^{-10} torr BEP. Note that Study B and C were conducted in a different MBE system with a Mg valved cracker, as such the optimal Mg flux is slightly larger than the optimal value found in Study A. Figure 4.4(a) shows the results of Study B1 where a constant modulation scheme (5 seconds open / 10 seconds closed) with various Ga fluxes was used. Initially, the hole concentration is 1.58×10^{18} cm^{-3} for a Ga flux of 3.0×10^{-7} torr BEP. As the Ga flux increases (becoming less N-rich), the hole concentration continues to increase, reaches a plateau, and then decreases at extremely Ga-rich conditions. At the maximum Ga flux point, the Ga-rich conditions are such that the Ga coverage slightly exceeds the N_2 coverage, therefore more Mg accumulates on the surface because of the limited availability of Ga substitutional sites, leading to less Mg incorporation [102].

Additionally, the resistivity falls off and settles at ~ 1 Ω-cm, as the growth conditions shift from N-rich to Ga-rich. Ideally, resistivity should increase with increasing Mg concentration, leading to partially compensated material (the material is n-type), if initially compared to an unintentionally doped material. The resistivity continues to increase until a maximum point is achieved and then decreases, once the Mg concentration is such that the material starts to become compensated (the material is p-type). At a maximum Mg concentration, the resistivity will increase again, as higher Mg concentration causes defects and the film becomes overly compensating. In our study, the resistivity initially decreases and remains nominally flat. It does not experience a second increase; the Mg is not creating self compensating defects. Therefore, based on

the analysis of the resistivity, it may be possible to Mg-doped GaN beyond the 1.38 × 10^{19} cm^{-3} hole concentration achieved in this study.

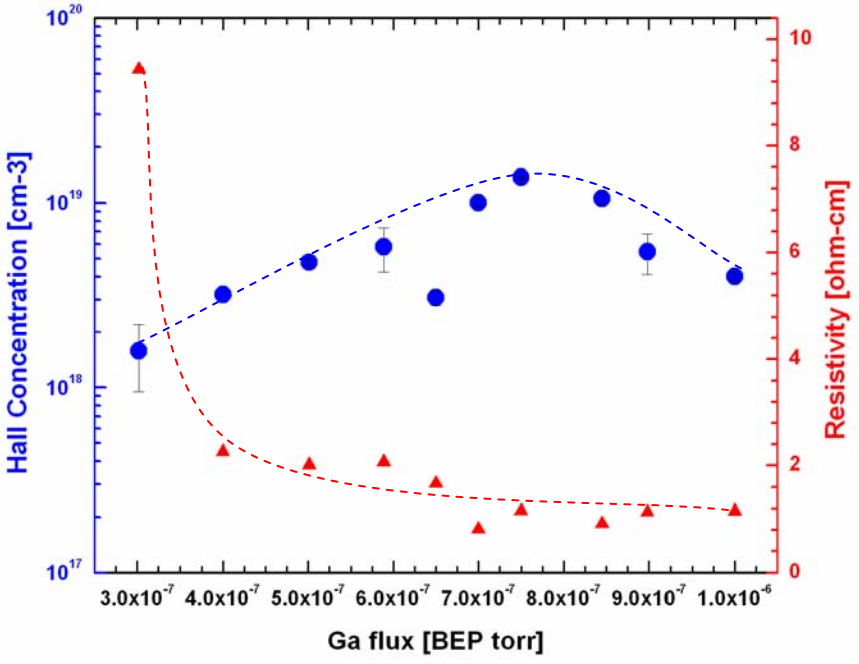

(a)

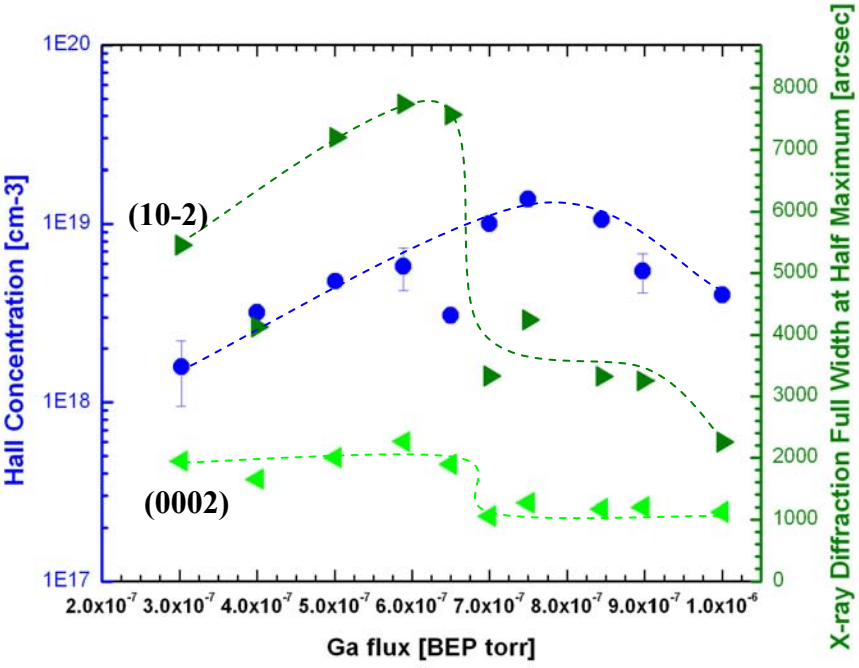

(b)

Figure 4.4 – Results from Study B1 of Mg-doped GaN with a substrate temperature of 500 °C for a fixed duty cycle of 5 seconds open/10 seconds closed. (a) Hall data with hole concentration in blue and resistivity in red. (b) XRD FWHM film quality for symmetric ω (0002) and asymmetric ω (10-2) reflections in green. Dotted lines are to guide the eye.

The crystal quality was investigated with XRD ω (0002) and ω (10-2) full width half maximum (FWHM) as shown in Figure 4.4(b), showing the effect of Ga surface coverage. When high Ga fluxes are used that approach the condition needed to get droplets (rightmost values in Figure 4.4(b)), hole concentrations are reduced resulting from non-optimal site incorporation and enhanced compensation of N-vacancies, but the material has a smooth non-faceted surface. When the average Ga flux moves toward more N-rich conditions, initially the crystal quality, as evidenced by the (0002) rocking curve in Figure 4.4(b) remains nearly constant but the hole concentration increases dramatically because of proper Mg site incorporation and reduced N-vacancy compensation.

To verify and prove the repeatability of our results, we kept a constant Ga flux and varied the modulation open time in Study B2. In Study B2, the shutter closed time was kept constant at 10 seconds. The shutter open time was varied at 1, 2, 5, 10, 30, and 60 seconds, with the 30 seconds open, resulting in highest hole concentration (10× greater than current literature values) of 2.04×10^{19} cm^{-3}. Again the results follow the same trend as in Study B1 for hole concentration and film quality, as shown in Figure 4.5. In this study the resistivity does increase with the longest open modulation time. This is caused by the increased Ga-rich conditions where the Ga coverage dramatically exceeds the N coverage and the Mg is not able to incorporate onto the Ga substitutional sites. Upon shutter close the Ga is not completely consumed and the original surface is not recovered.

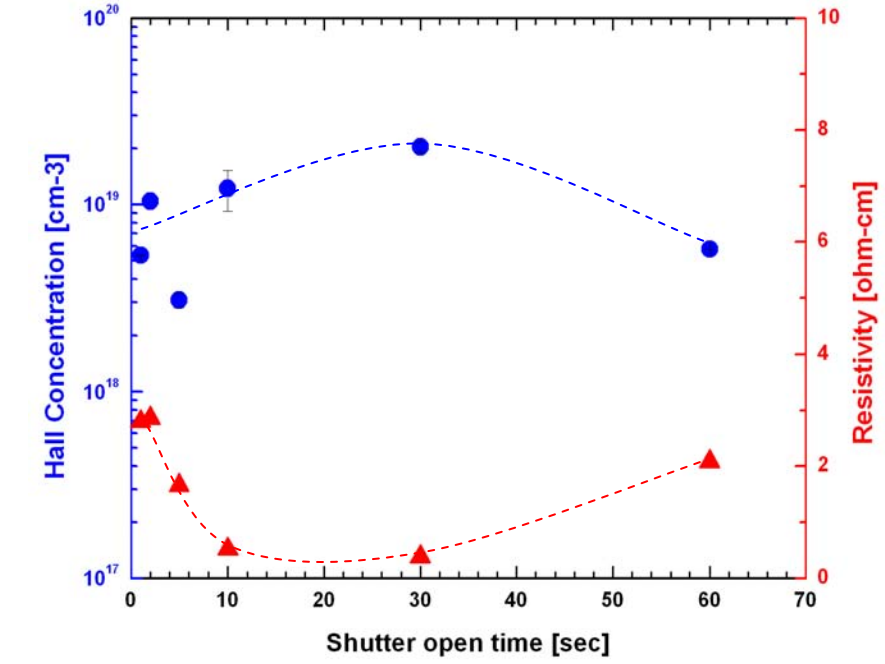

(a)

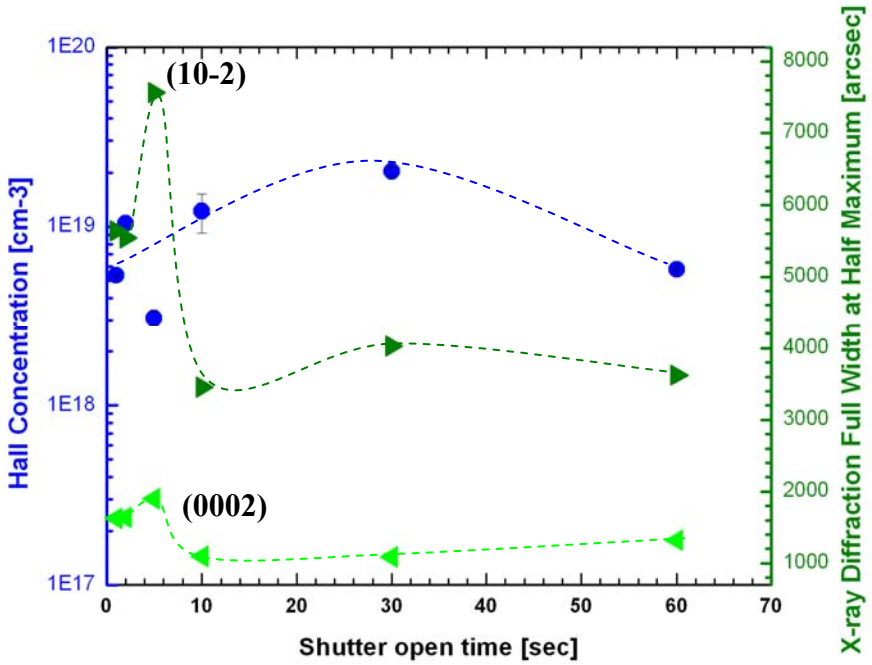

(b)

Figure 4.5 – Results from Study B2 of Mg-doped GaN for a substrate temperature of 500 °C, a fixed Ga flux of 6.5×10^{-7} torr BEP, with various modulation open time, and constant 10 second closed time. (a) Hall data with hole concentration in blue and resistivity in red. (b) X-ray diffraction full width at half maximum film quality for symmetric (0002) and asymmetric (10-2) reflections in green. Dotted lines are to guide the eye.

The film quality does show a sharp decrease in FWHM with shutter open times greater than 10 seconds as shown in Figure 4.5(b). During the shorter modulation times, Ga is unable to accumulate on the surface, resulting in N-rich growth conditions. N-rich conditions result in the degradation of the crystal quality and the subsequent reduction of effective hole concentration, because of bulk defect compensation, resulting from a faceted/columnar crystal. During longer modulation times, approaching the condition needed to accumulate droplets (right most value in Figure 4.5), the hole concentration is reduced and the material has smooth non-faceted surfaces, but suffer from non-optimal site incorporation and enhanced compensation by N-vacancies. As the modulation duty cycle becomes 1, the crystal quality as evidenced by the (0002) rocking curve in Figure 4.5 remains nearly constant and hole concentration increases because of proper Mg site incorporation and reduced N-vacancy compensation [103]. The net trade-offs, result in the best growth conditions being the periodic oscillation between Ga-rich and N-rich conditions, which has resulted in hole concentrations in excess of 1×10^{19} cm^{-3}.

Finally, Study C was conducted at a higher substrate temperature, 600 °C. The surface phase diagram in Figure 4.1 shows that at 600 °C, no intermediate regime exist and by using the MME technique, the growth will still oscillate between Ga-rich and N-rich conditions. Note that the low temperature growth is vital for preventing Mg surface segregation and therefore eliminating the resultant inversion domains which can act as compensating defects. The goal of the higher temperature is to improve surface smoothness and improve the structural quality of the p-type GaN.

Figure 4.6(a) shows the Hall concentration and resistivity follow the same trend regardless of substrate temperature. The solid symbols represent a substrate temperature

of 500 °C and the open symbols represent a substrate temperature of 600 °C. However, the Hall concentration is 2× greater than what was found in Study B2. The highest hole concentration, to date is 4.26×10^{19} cm^{-3} (20× larger than current literature values) with resistivity and mobility equal to 0.5 Ω-cm and 0.28 cm^2/Vs, respectively. Additionally, Figure 4.6(b) shows the crystalline film quality by XRD rocking curves. The symmetric values remain fairly constant in all three studies. However, the asymmetric values are reduced for a substrate temperature of 600 °C compared to those at 500 °C, indicating that the 600 °C sample is grown in a less columnar manner compared the 500 °C case. Therefore, the higher temperature growth resulted in fewer bulk compensating defects as well as higher hole concentration.

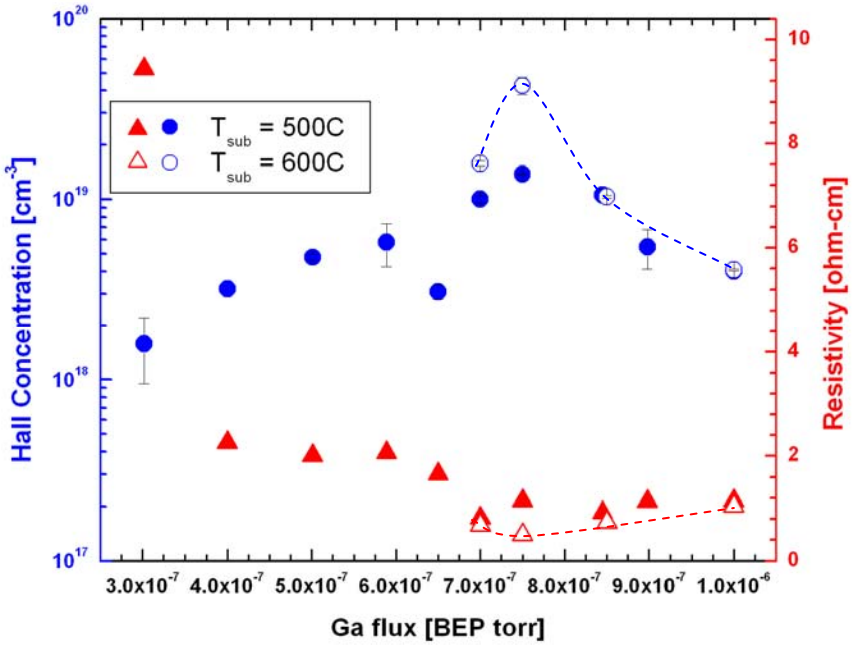

(a)

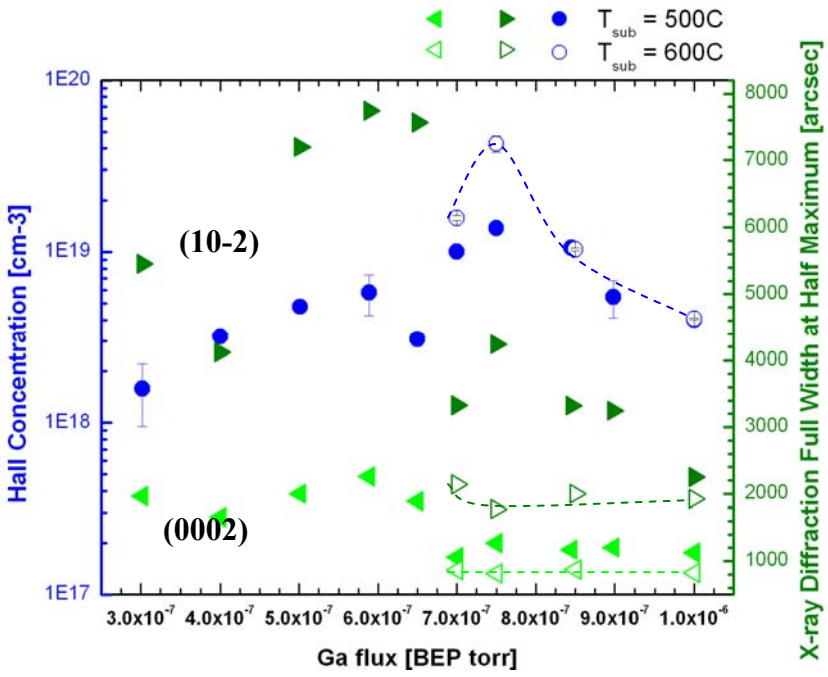

(b)

Figure 4.6 – Results from Study C of Mg-doped GaN with a substrate temperature of 600 °C, a fixed duty cycle of 5 seconds open/10 seconds closed. Open symbols represent samples grown at 600 °C and solid symbols represent samples grown at 500°C. (a) Hall data with hole concentration in blue and resistivity in red. (b) XRD FWHM film quality for symmetric ω (0002) and asymmetric ω (10-2) reflections in green. Dotted lines are to guide the eye.

4.1.1.2.Atomic Force Microscopy Results

Figure 4.7 shows atomic force microscopy (AFM) images of the epilayer surfaces from three Mg-doped GaN samples, representing the highest hole concentration achieved in Study B1, B2, and C, respectively. Table 4.1 shows the growth parameters, Hall concentration, and surface roughness root mean square (RMS) values for the samples. As the Hall concentration increases the RMS values also increase, which is counterintuitive based on the decrease in asymmetric FWHM values with increasing hole concentration.

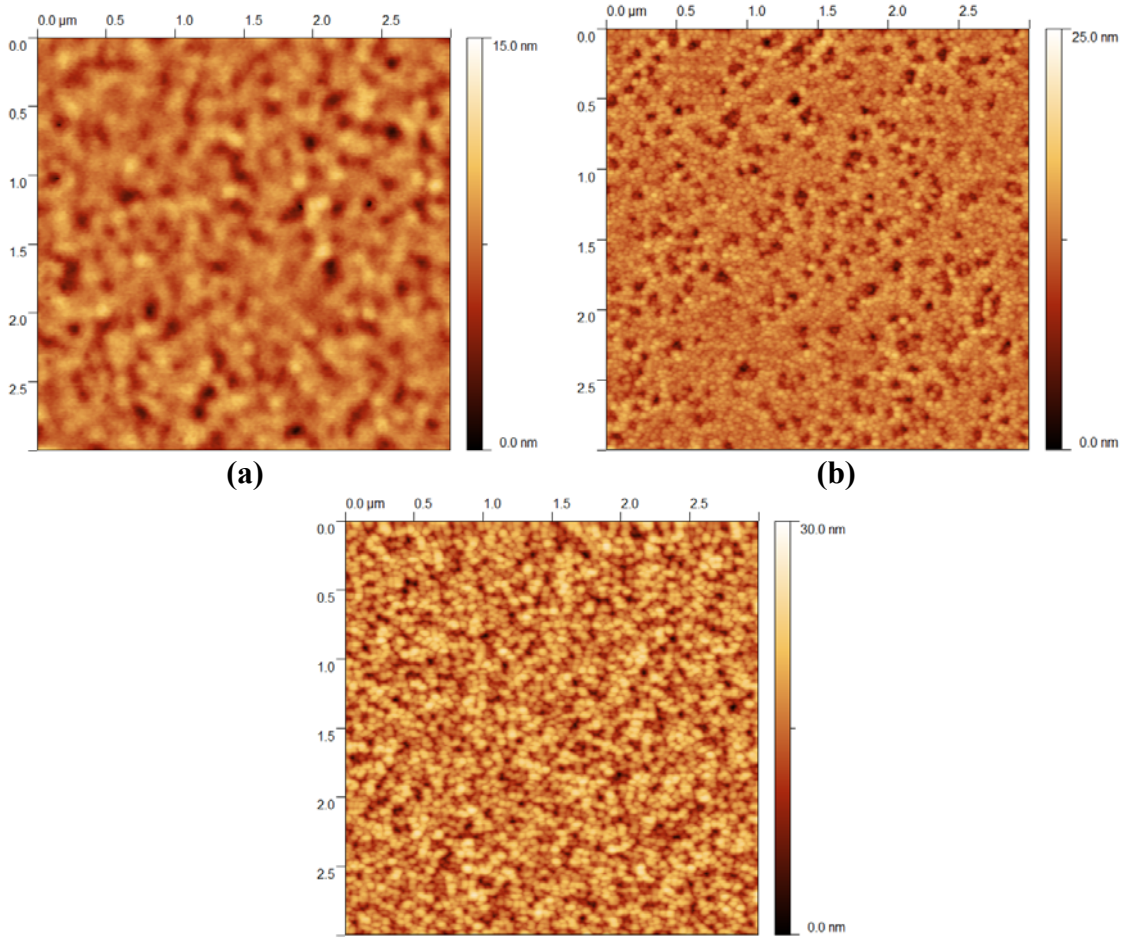

Figure 4.7 – AFM images of the highest hole concentration p-GaN samples from Study B1, B2, and C grown at (a) 500 °C with rms of 1.28 nm, (b) 500 °C with rms of 2.02 nm and (c) 600 °C with rms of 3.56 nm, respectively.[*]

[*] AFM images were done by M. Moseley and will be published in a literature paper based on this chapter.

Table 4.1 – Growth parameters, Hall results, and AFM surface roughness from the highest hole concentration samples presented in Study B1, B2, and C.

	Substrate Temperature [°C]	Ga Flux [torr BEP]	Modulation [open/close sec]	Hall Concentration [cm^{-3}]	RMS [nm]
Study B1	500	7.5E-07	5/10	1.38E+19	1.28
Study B2	500	6.5E-07	30/10	2.04E+19	2.02
Study C	600	7.5E-07	5/10	4.26E+19	3.56

As was stated before, a beneficial technique of MME is the use of Ga-rich conditions, to smooth the surface and prevent compensating extended defects resulting from faceting. This is followed by N-rich conditions to promote Mg incorporation onto the Ga-substitutional site without the production of compensating N-vacancies [102]. Note that Study B1 and C had identical growth conditions (Ga flux and modulation duty cycle), except for the substrate temperature. In general, an increase in substrate temperature results in an increase of III-metal desorption for MBE growth, however minuscule it may be (traditionally, as one increases the substrate temperature, one also increases the metal flux). The growth rate was reduced in Study C to 0.55 μm/hr compared to 0.63 μm/hr for study B1. Therefore, the substrate temperature difference between Study B1 and C resulted in more Ga-rich conditions for Study B1 (lower Mg incorporation and smoothing of the films) and slightly Ga-lean (N-rich) conditions for Study C (higher Mg incorporation and slightly rougher films), which is evident in the increased RMS values.

MME has been shown to be a powerful technique capable of growing p-type GaN with nearly 20× improvement in hole concentrations compared to the commonly accepted norm. Compromises in the Ga surface dose are made to accomplish the high hole concentrations and are attributed to the competition between improved Mg site selection and reduced N-vacancy compensation at moderate N-rich average Ga dose, verses the formation of extended defects.

4.2. Annealing Study of High Hole Concentration Mg-doped GaN

The previous sections presented results on high hole concentration Mg-doped GaN that will be used as the p-type contact layer in our $In_xGa_{1-x}N$/GaN heterojunction solar cells. During the solar cell fabrication, the sample will be annealed at 550 °C in a rapid thermal annealer (see Appendix D for details of the fabrication steps). The annealing step is required to alloy the contact metal and create ohmic contacts. Given that previous reports of high hole concentration resulted in metastable hole concentrations that reduced by ~50% upon annealing [104], it is imperative to prove that the present high hole concentration results are stable throughout the fabrication cycle including contact annealing.

A high hole concentration p-type GaN sample presented in Figure 4.4 for a Ga flux of 8.45×10^{-7} torr BEP was annealed at 550 °C for 30 seconds. Table 4.2 shows the results from the sample initially grown for the Mg-doped MME study. Before annealing the sample, the sample was p-type with an average hole concentration of 1×10^{19} cm^{-3}. After annealing the sample, the Hall effect measurement indicate that material remained p-type with an average hole concentration of 1.18×10^{19} cm^{-3} (measurements repeated three times to check for consistency). Therefore, it is concluded that the p-GaN films are robust and annealing the material will not effect the hole concentration of the p-GaN emitter.

Table 4.2 – Hall effect results of p-GaN sample initially presented in Figure 4.4. All measurements found that the material has p-type conductivity.

	Input Current [A]	Resistivity [Ωcm]	Hall Concentration [cm^{-3}]	Mobility [cm^2/Vs]
N2680	5.00E-05	0.9187	1.11E+19	0.612
	5.00E-05	0.9187	1.00E+19	0.57
N2680	1.00E-04	1.087	1.24E+19	0.46
annealed	2.00E-04	1.0859	1.31E+19	0.44
	5.00E-05	1.0903	9.96E+18	0.58

4.3. Systematic Study of Si-doped GaN

As a comparison for n-type GaN, specifically Si-doped GaN, a similar MME study was conducted to determine the electrical characteristics of Si-doped GaN. The samples were grown on c-plane Al_2O_3 wafers with a 140 nm thick AlN buffer layer. The n-GaN epilayer and subsequent n-GaN device layers used the MME technique with a 10 sec open / 10 sec closed duty cycle, while varying the Si cell temperature. The Ga flux was maintained at 1.0×10^{-6} torr BEP, resulting in Ga-rich conditions. The Si shutter was not modulated, because of persistent motor errors and the fact that unlike Mg, Si does not segregate to the surface. Therefore, if Si shutter modulation had occurred, the material grown during the shutter closed cycle would have been undoped.

The electrical results are shown in Figure 4.8 with the highest electron concentration achieved at a Si cell temperature of 1220 °C, equal to 3.91×10^{20} cm^{-3}. The resistivity and mobility were equal to 3.87×10^{-4} Ω-cm and 41.29 cm^2/Vs, respectively. The crystalline quality of the films, as evidenced by XRD rocking curves, found 600 – 800 arcsec and 1500 – 2200 arcsec for ω(0002) and ω(10-2), respectively. All subsequent n-GaN device layers will use the results achieved with a Si cell temperature of 1220 °C.

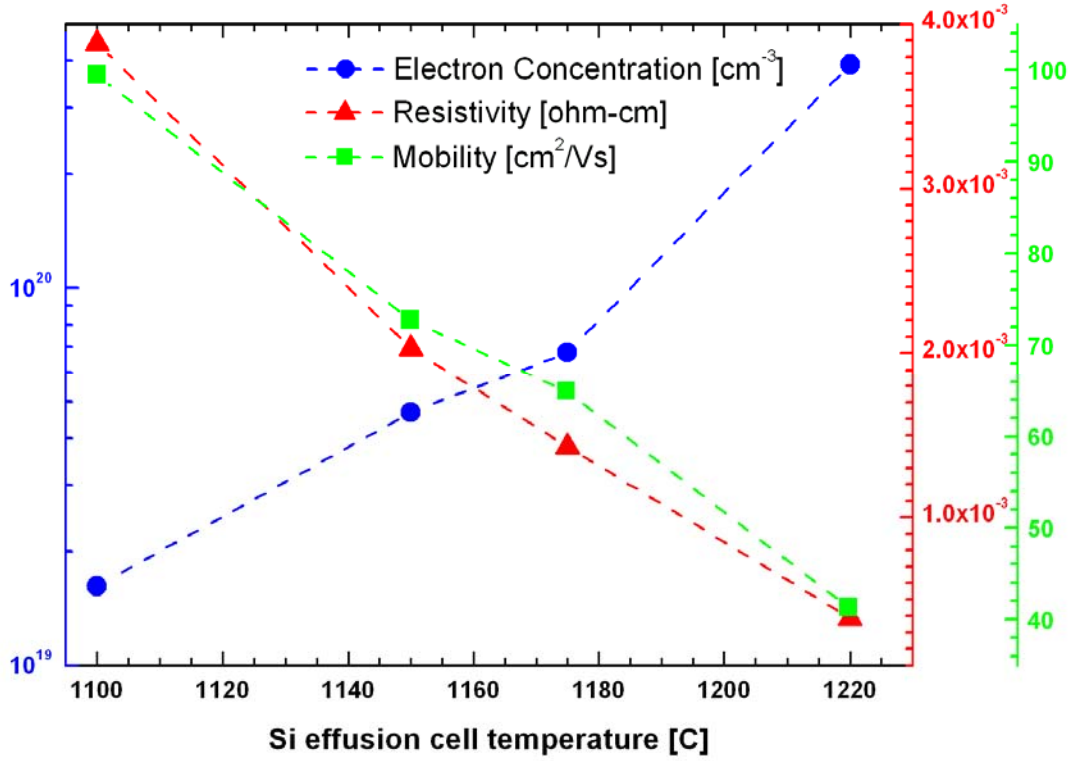

Figure 4.8 – Electrical characteristics of Si-doped GaN using MME for different Si cell temperatures.

4.4. Summary

A doping growth technique has been developed by effectively establishing the periodic buildup and depletion process of Ga atoms, which facilitates the incorporation of Mg dopants into Ga substitutional sites while suppressing the formation of compensating defects. MME has been shown to be a feasible, repeatable, beneficial, and powerful technique capable of growing p-type GaN with nearly 20× improvement in hole concentrations compared to literature standards; hole concentrations as high as 4.26 × 10^{19} cm^{-3} and resistivity of 0.5 Ω-cm were produced at substrate temperature of 600 °C. Compromises in the Ga surface dose are made to accomplish the high hole concentrations. RHEED images clearly show the retardation of faceting by the droplet rich half cycle of MME. The demonstrated capability of high hole concentrations in p-type GaN will

expedite the development of future nitride based electronic and optical devices where carrier concentration is correlated with light output. The peak hole concentration achieved herein is the first demonstration of degenerate p-type doping that is required for a tunnel junction for a tandem solar cell interconnect.

CHAPTER 5: Metal Modulated Epitaxy Growth of InN and $In_xGa_{1-x}N$

The MME technique has proved useful for AlN and GaN growth where surface phase diagrams have a metal-rich regime, a N-rich regime, and an intermediate regime, as shown in Figure 4.1. The smoothest, droplet free film morphology is found by growing in the intermediate regime for AlN and GaN [99]. Galliant et al. developed an In-polar InN growth diagram which is shown in Figure 5.1, where there is no intermediate regime and a growth window is strongly dependent on the substrate temperature. The lack of an intermediate regime is related to the low dissociation temperature at high equilibrium vapor pressure of nitrogen [23].

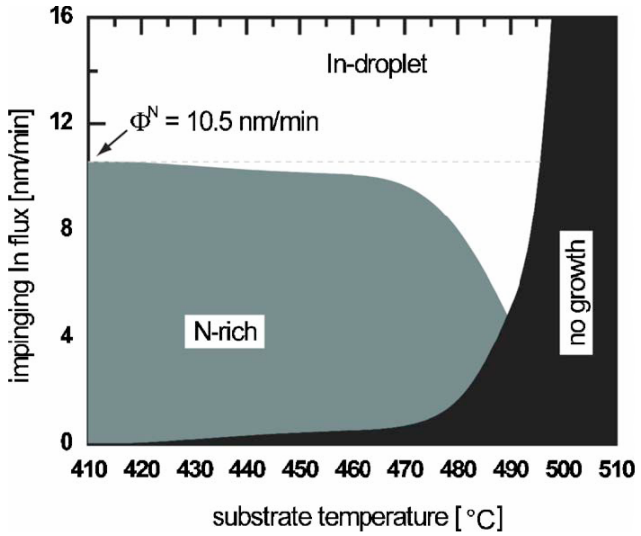

Figure 5.1 – In-polar InN MBE growth surface phase diagram with a limited parameter space and no intermediate regime [105].

InN films grown in the N-rich regime exhibited rough surface morphologies and the loss of step-flow growth features. Conversely, growth in the In-droplet regime resulted in relatively smooth, spiral hillock rich morphology, typically found in dislocation pinned

step-flow growth of GaN. Attempts to deposit InN in the "no growth" regime resulted in the accumulation of In droplets and the lack of an InN film [105].

The surface phase diagram for InN is comparable to the portion of GaN surface phase diagram used in the Mg-doped GaN study, where there is a lack of an intermediate regime. Modulating between metal-rich conditions and N-rich conditions allows Mg to incorporate on Ga sites more effectively on N-rich surfaces, and oscillating to metal rich conditions reduces the compensating defect density. The low growth temperatures used are vital for preventing Mg surface segregation, which induces compensating defects. Therefore, the low growth temperatures required for InN growth, along with the MME technique should be an effective approach for producing p-type Mg-doped InN films.

5.1 Mg-doped InN

As-grown InN has high n-type carrier concentrations resulting from native defects, which have been attributed to nitrogen vacancies in the InN lattice [22, 106]. The nitrogen vacancies compensate the material, which makes p-type doping extremely difficult. This situation is exactly analogous to the GaN situation where N-vacancies are the primary n-type compensating defect. Additionally, it has been well documented in the literature that InN films exhibit electron accumulation at the surface, with the surface Fermi level lying far above the conduction band edge [58, 107, 108]. The accumulation layer is strongly localized within the first 5 nm of the film surface with a local carrier concentration as high as 1×10^{21} cm^{-3} in this region [58, 107]. The highly conductive surface layer in InN films is an added difficulty in determining p-type conduction in Mg-doped films.

As was presented in Chapter 4, the use of the MME growth technique was extremely successful for Mg-doped GaN. The MME technique was attempted with undoped InN growth with limited success, which prevented a complete study into Mg-doped InN. The lack of success is in part related to the difficult growth parameters needed for InN growth and inconsistent *in-situ* RHEED analysis. The intensity of the RHEED beam has been shown in previous studies to create streaks on the wafer surface, as shown in Figure 5.2.

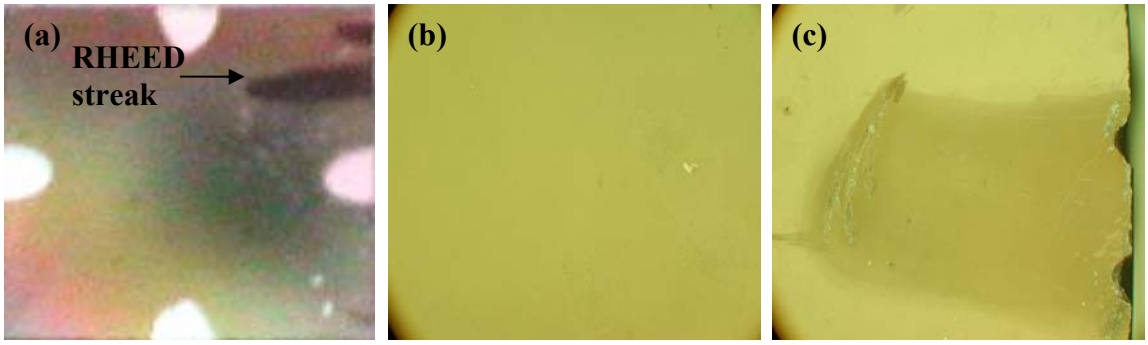

Figure 5.2 – Images of an InN growth with RHEED monitoring throughout the growth: (a) sample after growth, (b) microscope image in the middle of the wafer, and (c) microscope image inside the RHEED streak.

Figure 5.2(a) is an image of an InN sample after growth with a visible RHEED streak in the right-hand corner. Figure 5.2(b) and (c) are microscope images in the middle of the wafer and inside the RHEED streaky, respectively, showing that there is a significant change in film morphology caused by the RHEED beam. It is surmised that the RHEED beam creates either localized heating causing the film to decompose or the electron beam causes electrons stimulated desorption [109, 110]. Therefore, RHEED analysis during InN growth provides inaccurate results and transient responses making the development of MME for InN an unguided study. One way to overcome localized heating from the RHEED beam, would include equipment modification where the RHEED beam is pulsed, lowering the thermal decomposition. At the time this InN modulated study was

conducted, the RHEED gun had not been modified, resulting in difficult RHEED analysis for the MME growth technique.

5.1.1 Growth Conditions and Analysis

The Ga fluxes used in MME are exceedingly large, such that without modulating the shutter, Ga-droplets would accumulate. Modulation to N-rich conditions in MME allows the excess Ga to be consumed. In this initial modulation study of InN, In was found to buildup on the surface, but was not completely consumed when oscillating to N-rich conditions. InN can form on top of these droplets creating InN capped In droplets. Therefore, the growth continues to accumulate In-droplets, preventing further growth of InN.

Figure 5.3 show microscope images of four MME InN growths where the substrate was maintained at 450 °C, In flux of 2.0×10^{-7} torr BEP, with various modulation schemes: 4 seconds open / 2 seconds closed, 4 seconds open / 4 seconds closed, 2 seconds open / 4 seconds closed, and 1 seconds open / 3 seconds closed, respectively. For reference, at this substrate temperature, an In flux of ~ 8×10^{-8} torr BEP would normally result in stoichiometric InN growth without shuttering. The growth rate was ~ 0.18 – 0.23 μm/hr, significantly lower than the growth rate of ~ 0.6 μm/hr and ~ 1.1 μm/hr for Mg-doped GaN and Si-doped GaN, respectively.

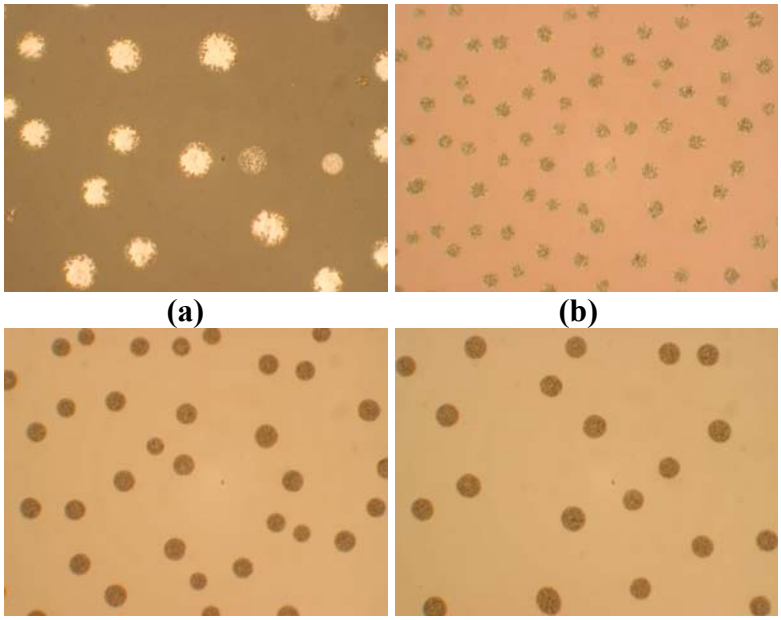

Figure 5.3 – Optical microscope images of InN films grown with the MME technique. Duty cycles equal to (a) 2.0, (b) 1.0, (c) 0.5, and (d) 0.33.

The buildup of droplets is evidenced in Figure 5.3(a) with shinny droplets and from a sharp In droplet peak located at $\omega = 16.473\ ^\circ$ evidenced in XRD ω-2θ scans in Figure 5.4(a). Figure 5.4(a) also shows the other three samples using the various modulation schemes. Reducing the duty cycle did eliminate the In droplet peak in the ω-2θ scan, but decreased the crystalline quality, as evidenced in Figure 5.4(b). The duty cycle is defined as the shutter open time divided by the shutter closed time.

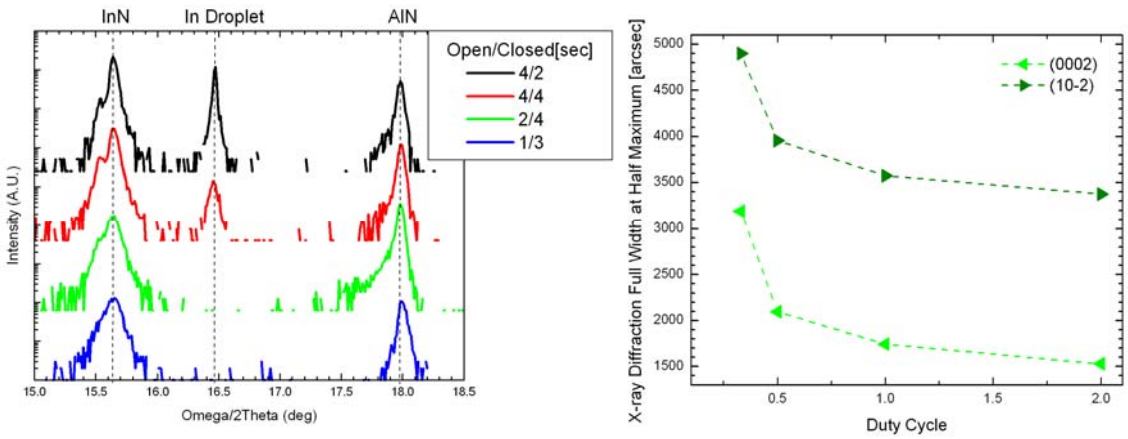

Figure 5.4 – XRD results of MME grown InN (a) ω-2θ scans with peaks at InN, In droplets, and the AlN buffer. (b) FWHM film quality versus duty cycle.

The other images in Figure 5.3 show circular brown drops and further SEM images found that the drops are regions where InN formed on top of In droplets that subsequently dried out, possibly during cool down after growth, as shown in the upper image of Figure 5.5(a). These collapsed bubbles of InN reduce the film quality, which is shown in the broadening of the ω-2θ InN peak in Figure 5.4(a) and by the increase in symmetric ω (0002) and asymmetric ω (10-2) FWHM values shown in Figure 5.4(b). As mentioned previously, the samples were grown on AlN buffer layers with growth rates of ~ 0.18 – 0.23 μm/hr. The slow growth rate and buildup of In droplets is attributed to inappropriate nucleation. A low temperature InN buffer layer was implemented to improve the nucleation. The low temperature buffer did improve the growth rate to ~ 0.75 μm/hr, however the films still show partial coalescences as evidences in SEM images.

Figure 5.5(b) shows partial coalescences of a 70nm InN film grown on GaN (0001) by MBE at 370 °C [37]. Lebedev et al. state that for their film, the coalescence is not completed and the surface structure is dominated by large wurtzite domains; further increasing the film thickness resulted in slow improvements of material quality. In our

MME study, various growth times, In fluxes, substrate temperatures, and growth time were investigated, with marginal improvement in coalescences. The lower image in Figure 5.5(a) shows the partial coalescences of the film at the edge of the collapsed bubble. Improved film quality requires appropriate nucleation and complete coalescences of the InN film.

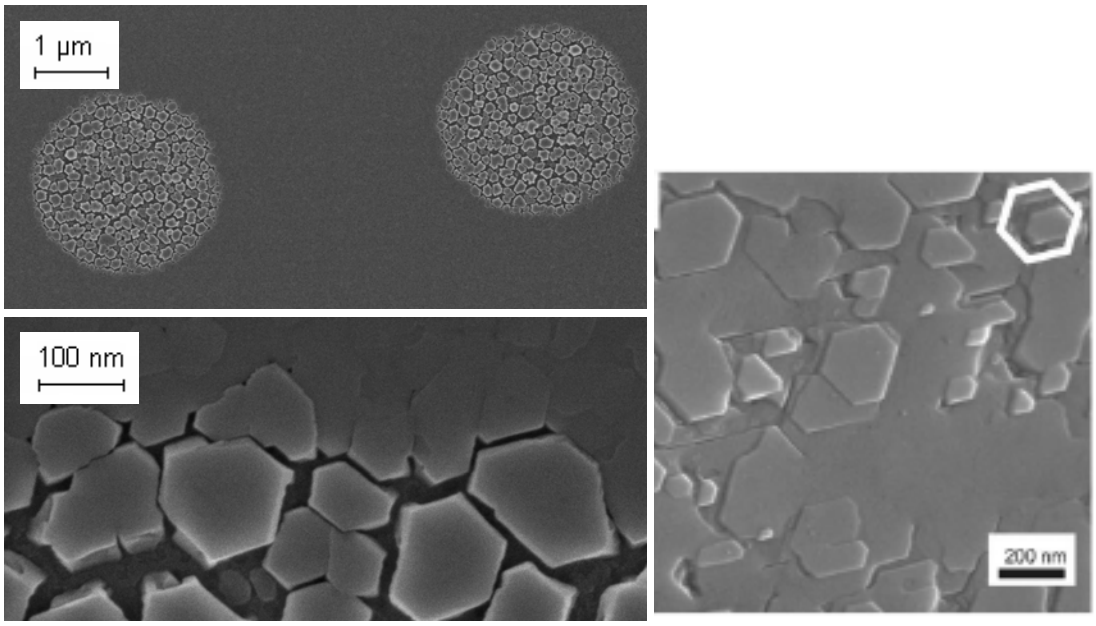

(a) **(b)**

Figure 5.5 – SEM images of (a) ~100 nm thick InN layer showing exaggerated partial coalescence. (b) 70 nm thick InN layer after the partial coalescence stage [37].

Yamguchi et al. [111] grew In-rich InN which resulted in excess In on the surface, followed by a continuous supply of nitrogen which transformed the excess In on the surface into InN, an identical approach as our MME growth technique. RHEED intensity followed the same pattern for GaN grown by MME; a decreasing RHEED intensity signal with In-rich conditions, followed by an increased signal with the nitrogen-plasma treatment. In their work, the shortest duty cycle used was 120 seconds In-rich conditions / 120 seconds of the nitrogen-plasma treatment and the longest duty cycle was 400 seconds / 475 seconds. The duty cycle used by Yamguchi is significantly larger than

what was presented in this work. Successful growth of InN with the MME technique will require an extensive study with extended shutter close times and a nucleation buffer study. At this time a complete MME InN study is beyond the scope of this work and will be included in the future work section of Chapter 8. The current inability to grow InN using the MME technique prevents an investigation into Mg-doped InN grown by MME and will be left for the future work section of Chapter 8.

5.2 Summary

This chapter presented results from Mg-doped InN using the MME growth technique. Successful growth of InN with the MME technique will require an extensive study into low temperature InN nucleation layers and InN epilayers with extended shutter close times. Short modulation times of less than 4 seconds, resulted in accumulation of In droplets and InN films grown on top of the droplets. The droplets subsequently dried out, causing the InN film to collapse and therefore, prevented an investigation into Mg-doped InN.

CHAPTER 6: $In_xGa_{1-x}N$ Solar Cell

This chapter will use all of the knowledge of InN, $In_xGa_{1-x}N$, and p-GaN growth and combine them to create an $In_xGa_{1-x}N$ heterojunction solar cell. $In_xGa_{1-x}N$ is a unique semiconductor that can span the bandgap range from 0.68 to 3.4 eV, which correlates to nearly 90% of the solar spectrum. Using a bandgap modeling program, SiLENSe, proposed device structures were modeled under zero bias and the optimal designs were grown and fabricated. Theoretical dark current-voltage curves are then compared to experimental curves in an attempt to elucidate theoretical/experimental device discrepancies.

6.1. SiLENSe

Simulator for Light Emitters based on Nitride Semiconductors (SiLENSe) software was created by Semiconductor Technology Research, Inc. to develop and model light emitting diodes. The software was used to model the band diagrams of our initial device designs and then create modified designs, shown in Figure 6.1 and Figure 6.2, respectively. Ideally Figure 6.1(a) is the optimal structure with a p-type buried layer, resulting in the electrons as minority carriers in the device. However, p-type material is riddled with defects, making it an undesirable layer to grow on. Therefore, p-type material must be the top-most layer making the III-N solar cell a n-type base, hole minority carrier device. Figure 6.1(b) – (d) use an n-type buried $In_xGa_{1-x}N$ with different capping layers used to achieve an optimal ohmic contact to the p-type material.

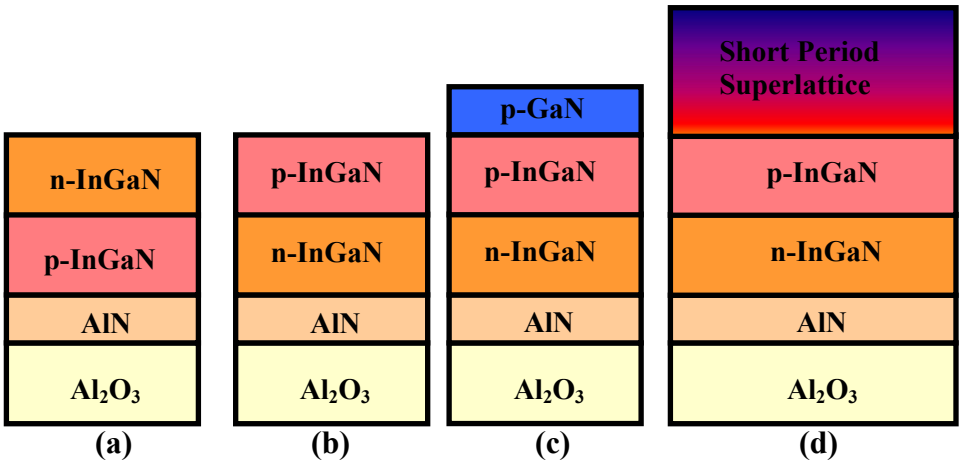

Figure 6.1 – $In_xGa_{1-x}N$ homojunction solar cell designs: (a) p-type buried layer, (b) n-type buried layer, (c) n-type buried with a p-GaN capping layer, and (d) n-type buried layer with a short period superlattice capping layer.

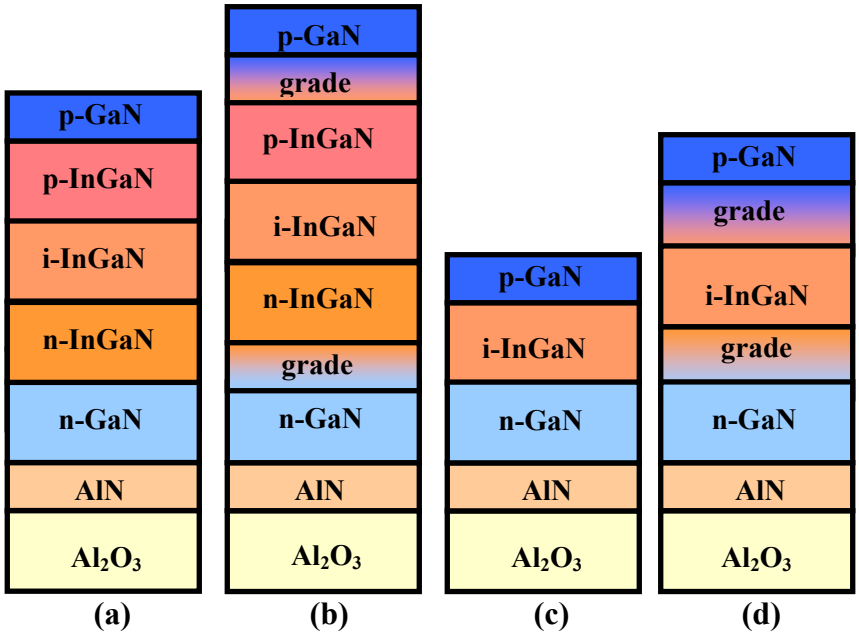

Figure 6.2 – $In_xGa_{1-x}N$ heterojunction solar cell designs: (a) n-GaN and n-$In_xGa_{1-x}N$ buried layer, (b) similar to (a) with grading between GaN and $In_xGa_{1-x}N$ layers, (c) n-i-p with n-GaN buried contact layer, and (d) similar to (c) with grading between GaN and $In_xGa_{1-x}N$ layers.

Previous attempts at heterojunction p-$In_xGa_{1-x}N$/n-GaN solar cells have proven fruitless because the $In_xGa_{1-x}N$:Mg contact resistance is in the 1000 Ω range, where as GaN:Si contact resistance was in the 1 Ω range. Optimally, the $In_xGa_{1-x}N$ solar cell would utilize transparent ohmic contacts such as, a p-GaN capping layer or a short period

superlattice (SPS) capping layer achieving the required transparency and allowing for high quality ohmic contacts. Representative device structures of the p-GaN and SPS capping layer are shown in Figure 6.1(c) and (d), respectively.

The SPS structure will act to increase current flow in the highly resistive p-type material, a limiting factor in GaN based devices. Kozodoy et al. [112] state that polarization effects from highly conductive p-type AlGaN/GaN superlattices creates a periodic oscillation of energy bands, which enhances the ionization of deep acceptors and leads to the accumulation of carriers in sheets. Therefore, increasing the room temperature hole concentration by ten times. Sheu et al. [113] found that Si-doped n^+-$In_xGa_{1-x}N$ /GaN SPS can achieve a lower operation voltage and a smaller series resistance. However, as was proven in Chapter 4, this research has achieved degenerately doped Mg-doped GaN with the highest recorded hole concentration (at time of publication) of 4.26×10^{19} cm^{-3}, resistivity, and mobility equal to 0.5 Ω-cm and 0.28 cm^2/Vs, respectively. Therefore, the SPS capping layer is unnecessary and will not be explored in this research.

6.1.1. Band Diagrams

Figure 6.3 shows the associated band diagrams at zero bias for the structures in Figure 6.1. Figure 6.3(c) is a n-p device including the AlN buffer used in all samples grown on Al_2O_3. The large spike located at 120 nm is related to the band discontinuity between the AlN and $In_xGa_{1-x}N$, because of this polarization discontinuity induced large spike, the AlN layer cannot be used as the base contact layer. The devices grown in this study have a ~ 2μm thick n-GaN contact base layer. Figure 6.3(d) corresponds to the

structure shown in Figure 6.1(c). The spike in this figure located at 400 nm is also related to polarization discontinuity between the $In_xGa_{1-x}N$ and GaN.

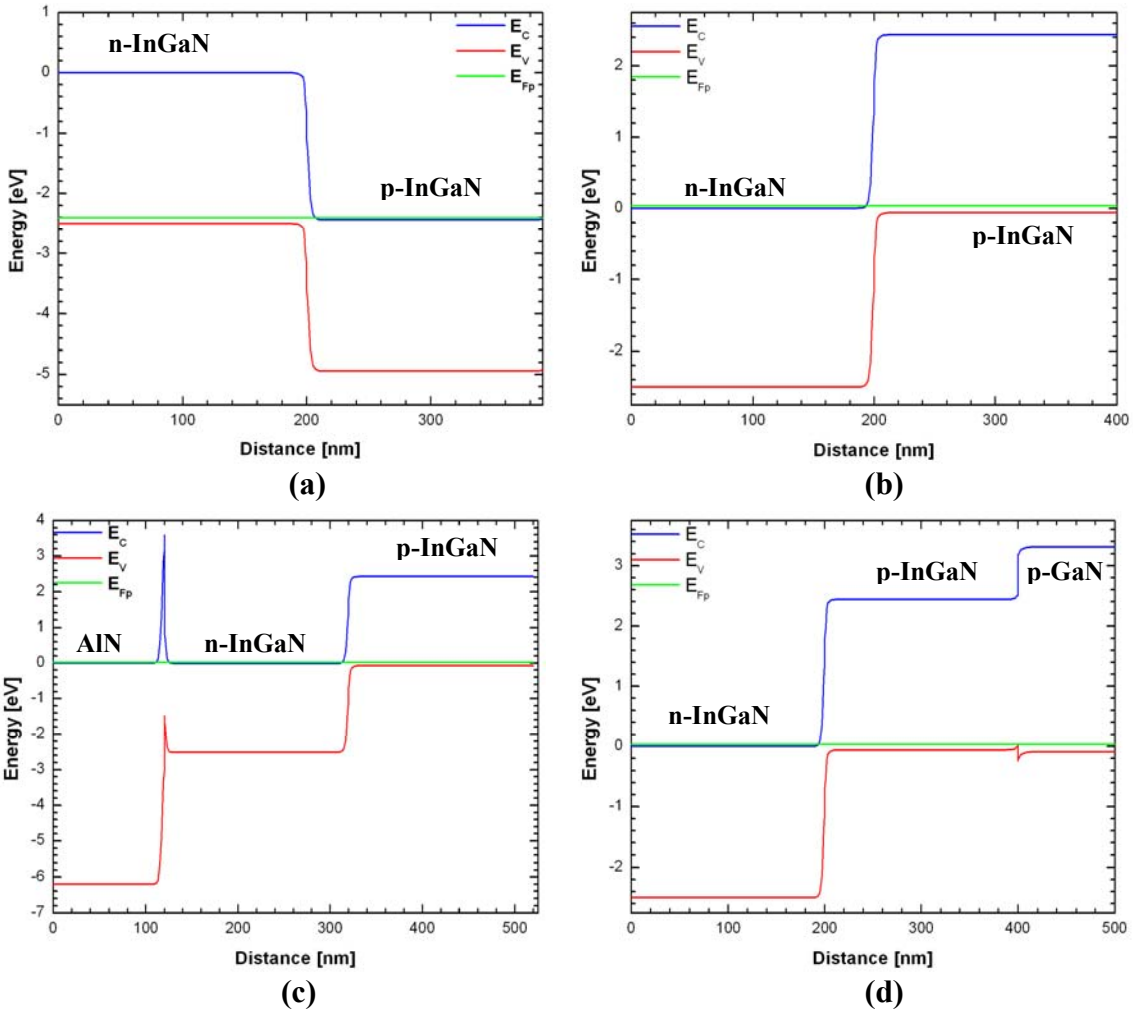

Figure 6.3 – Simulated band diagrams corresponding to the band structures in Figure 6.1. (a) p-type buried layer, (b) n-type buried layer, (c) n-type buried layer including the AlN buffer layer showing the discontinuity between AlN and $In_xGa_{1-x}N$, and (d) n-type buried with a p-GaN capping layer.

Based on band diagrams in Figure 6.3, band engineering was introduced, where a compositional grade with controlled doping is established between the GaN and $In_xGa_{1-x}N$ layers to remove the polarization discontinuity spike. SiLENSe code is capable of modeling graded-composition heterostructures, an important feature for bandgap engineering principles [114]. Figure 6.4 shows the device structures of the new

heterojunction device designs: (a) abrupt transitions between layers and (b) compositionally graded doped layers.

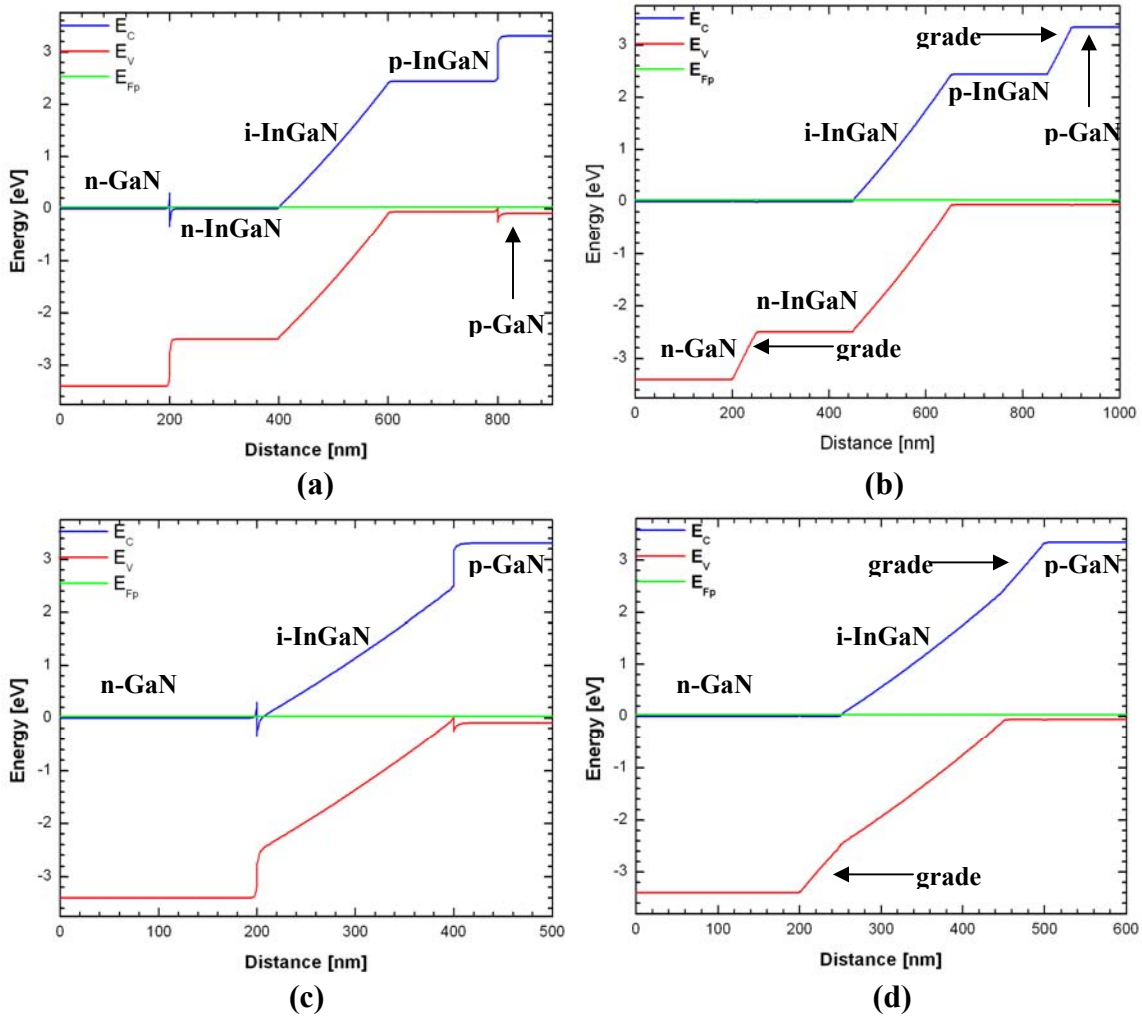

Figure 6.4 – Simulated band diagrams corresponding to the band structures in Figure 6.2. (a) n-GaN and n-$In_xGa_{1-x}N$ buried layer, (b) similar to (a) with grading between GaN and $In_xGa_{1-x}N$ layers, (c) n-i-p with n-GaN buried contact layer, and (d) similar to (c) with grading between GaN and $In_xGa_{1-x}N$ layers.

The SiLENSe bandgap model of a device with a grade between the GaN base and emitter shows a smooth transition and a Fermi level that is flat. Conversely, removing the grade creates large polarization discontinuities resulting in large spikes in the bands where holes and electrons will become trapped and limit the performance of the device. Therefore, the difference between in I-V curves of the fabricated devices with graded

transitions and abrupt transitions should prove the importance of graded transitions. It should be noted that the lack of graded junction may be the reason for a lack of photovoltaic output from our original devices.

Also, while modeling the band diagrams, it was discovered that n-$In_xGa_{1-x}N$ and p-$In_xGa_{1-x}N$ layers were unnecessary. Compensated $In_xGa_{1-x}N$ (i- $In_xGa_{1-x}N$) between the n-GaN and p-GaN layers was sufficient to create a broad depletion region and significantly reduced the growth time, which will be an advantageous feature in commercialization. Figure 6.4(c) and (d) show device structures with the compensated layer with abrupt transitions and with graded layers, respectively. In Figure 6.4(a) and (c) there are polarity discontunities at the GaN and $In_xGa_{1-x}N$ transitions and are eliminated in (b) and (d) with a compositional controlled doped grade.

Note that the SiLENSe band diagram simulations did not model the actual device thicknesses. The bending of the bands is related to the thickness of the layer, but for clarity the thickness was reduced to accentuate distinct features between the layers. However, the band bending does impact the depletion volume, provided that the $In_xGa_{1-x}N$ is sufficiently resistive. The band diagrams are used for demonstration purposes only.

6.1.2 SiLENSe Parameters

SiLENSe allows users to input all material properties, from the alloy percentage, the donor and acceptor concentration, the mobility, and the layer thickness.

Table 6.1 shows the typical material parameters used in the SiLENSe modeling. SiLENSe models the donor and acceptor concentration as a single band in the band diagram, similar to the diagram in Figure 6.5(a). Chapter 4 discussed in detail the 20× improvement in hole concentration for Mg-doped GaN. Initial temperature dependent Hall measurements found that the high hole concentration samples had a lower activation energy of ~0.06 – 0.08 eV [103] compared to a typical acceptor activation energy for Mg in GaN of ~ 0.170 eV [90]. This lowering of the activation energy and doping dependent behavior indicates the onset of the Mott-Insulator transition where the acceptor – acceptor interaction results in a band of states as opposed to a singular level. Figure 6.5(b) depicts this Mott-Insulator transition with a band of acceptors.

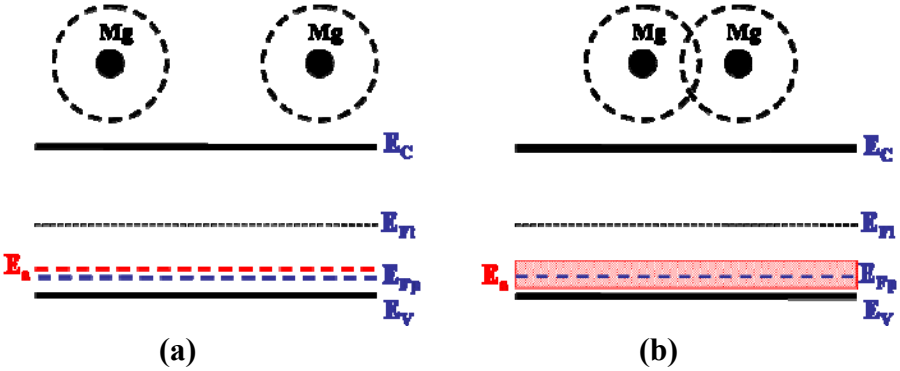

Figure 6.5 – Diagram of the Bohr Radius of an atom (a) depicted as a single acceptor level and (b) reaching the Mott-Insulator transition, creating a band of acceptor levels.

To achieve a high hole concentration emitter, the SiLENSe acceptor level was varied from 1×10^{16} to 1×10^{21} cm^{-3} resulting in the Mg-emitter having hole concentrations from ~ 8×10^{15} to 5×10^{19} cm^{-3}, respectively. Therefore, given the numerical limitation of SiLENSe only modeling a deep single energy acceptor, the acceptor values in SiLENSe were, set to the unrealistically high value of 1×10^{21} for the p-type emitter, equivalent to the experimentally determined hole concentration of ~$1 \times 10^{19} cm^{-3}$.

Table 6.1 – Representative parameters used for SiLENSe modeling.

		Layer Left Side				Layer Right Side			
		In%	Ga%	Donors [cm^{-3}]	Acceptors [cm^{-3}]	In%	Ga%	Donors [cm^{-3}]	Acceptors [cm^{-3}]
Figure 6.3									
(a)	InGaN:Mg base	0.25	0.75	1.0E+15	1.0E+19	0.25	0.75	1.0E+15	1.0E+19
	InGaN:Si emitter	0.25	0.75	5.0E+19	1.0E+15	0.25	0.75	5.0E+19	1.0E+15
(b)	InGaN:Si base	0.25	0.75	5.0E+19	1.0E+15	0.25	0.75	5.0E+19	1.0E+15
	InGaN:Mg emitter	0.25	0.75	1.0E+15	1.0E+19	0.25	0.75	1.0E+15	1.0E+19
(c)	AlN buffer*	0	0	5.0E+19	1.0E+15	0	0	5.0E+19	1.0E+15
	InGaN:Si emitter	0.25	0.75	5.0E+19	1.0E+15	0.25	0.75	5.2E+02	1.0E+15
	InGaN:Mg emitter	0.25	0.75	1.0E+15	1.0E+19	0.25	0.75	1.0E+15	1.0E+19
(d)	InGaN:Si base	0.25	0.75	5.0E+19	1.0E+15	0.25	0.75	5.0E+19	1.0E+15
	InGaN:Mg emitter	0.25	0.75	1.0E+15	1.0E+19	0.25	0.75	1.0E+15	1.0E+19
	GaN:Mg cap	0	1	1.0E+15	1.0E+19	0	1	1.0E+15	1.0E+19
Figure 6.4									
(a)	GaN:Si base	0	1	5.0E+19	1.0E+15	0	1	5.0E+19	1.0E+15
	InGaN:Si	0.25	0.75	5.0E+19	1.0E+15	0.25	0.75	5.0E+19	1.0E+15
	UID InGaN	0.25	0.75	1.0E+16	1.0E+14	0.25	0.75	1.0E+16	1.0E+14
	InGaN:Mg emitter	0.25	0.75	1.0E+15	1.0E+19	0.25	0.75	1.0E+15	1.0E+19
	GaN: Mg cap	0	1	1.0E+15	1.0E+19	0	1	1.0E+15	1.0E+19
(b)	GaN:Si base	0	1	5.0E+19	1.0E+15	0	1	5.0E+19	1.0E+15
	InGaN:Si grade	0	1	5.0E+19	1.0E+15	0.25	0.75	5.0E+19	1.0E+15
	InGaN:Si	0.25	0.75	5.0E+19	1.0E+15	0.25	0.75	5.0E+19	1.0E+15
	UID InGaN	0.25	0.75	1.0E+16	1.0E+14	0.25	0.75	1.0E+16	1.0E+14
	InGaN:Mg emitter	0.25	0.75	1.0E+15	1.0E+19	0.25	0.75	1.0E+15	1.0E+19
	InGaN:Mg grade	0.25	0.75	1.0E+15	1.0E+19	0	1	1.0E+15	1.0E+19
	GaN:Mg cap	0	1	1.0E+15	1.0E+19	0	1	1.0E+15	1.0E+19
(c)	GaN:Si base	0	1	5.0E+19	1.0E+15	0	1	5.0E+19	1.0E+15
	UID InGaN	0.25	0.75	1.0E+16	1.0E+14	0.25	0.75	1.0E+16	1.0E+14
	$GaN:Mg emitter	0	1	1.0E+15	1.0E+19	0	1	1.0E+15	1.0E+19
(d)	GaN:Si base	0	1	5.0E+19	1.0E+15	0	1	5.0E+19	1.0E+15
	InGaN:Si grade	0	1	5.0E+19	1.0E+15	0.25	0.75	5.0E+19	1.0E+15
	UID InGaN	0.25	0.75	1.0E+16	1.0E+14	0.25	0.75	1.0E+16	1.0E+14
	InGaN:Mg grade	0.25	0.75	1.0E+15	1.0E+19	0	1	1.0E+15	1.0E+19
	$GaN:Mg emitter	0	1	1.0E+15	1.0E+19	0	1	1.0E+15	1.0E+19

*AlN layer set Al % equal to one on the left and right side.

$In the later sections the acceptor doping was varied.

6.1.3 Dark Current-Voltage Simulations

The SiLENSe software is intended for modeling band diagrams and characteristics of LEDs. SiLENSe provides exhaustive information about complex physical processes responsible for the operation of LEDs based on wide bandgap wurtzite materials and hybrid structures [114]. SiLENSe was not intended for modeling the output characteristics of a solar cell. It does not have the capability of modeling the photocurrent generated under illumination. However, SiLENSe can be used to model the dark current-voltage (I-V) characteristics of a solar cell. Most solar cells resemble a diode in the dark, creating a current that flows across the device under an applied voltage. The simulated dark I-V curve will be compared with the test results as a measure of the device performance.

Four devices were fabricated with structures similar to Figure 6.2(c) and (d). Chapter 6.2 will discuss the growth parameters of the fabricated devices. Figure 6.6 and Figure 6.7 show the simulated results based on the device in Figure 6.2(c), this device has abrupt transitions between the n-GaN/i-$In_xGa_{1-x}N$ and i-$In_xGa_{1-x}N$/p-GaN. The dark I-V curves and corresponding band diagrams are shown with respect to various acceptor concentrations for the p-GaN emitter.

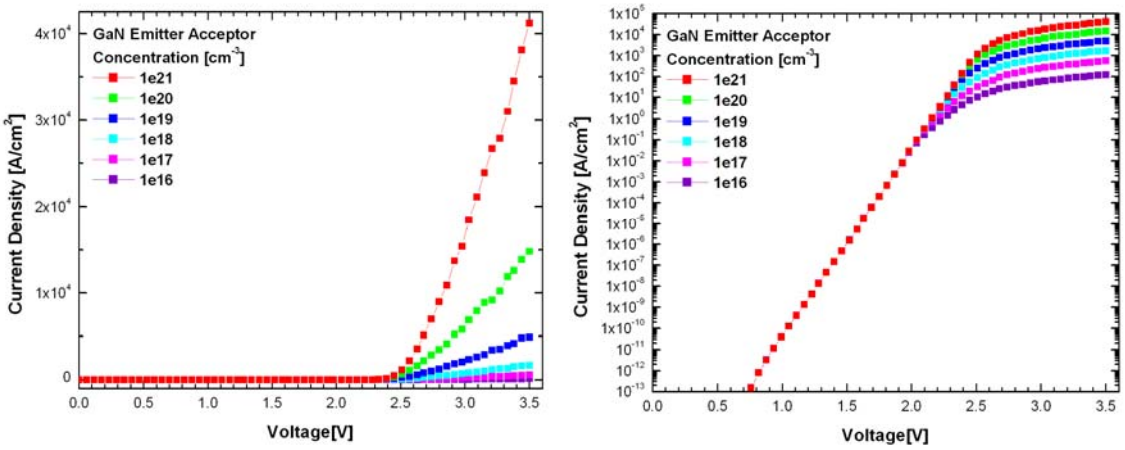

Figure 6.6 – Dark I-V curve of Figure 6.2(c), a p-GaN/UID-$In_xGa_{1-x}N$/n-GaN solar cell with various targeted p-GaN hole concentrations: (a) linear scale and (b) logarithmic scale.

The series resistance of the device and the diode ideality factor can be identified when the dark I-V curve is plotted on a semi-logarithmic graph as shown in Figure 6.6(b). The series resistance is associated with bulk material resistance and the resistance of metal contacts. The ideality factor typically ranges from 1 to 2. An ideality factor greater than 1 reduces the fill factor of the solar cell and in heterojunction solar cells, an ideality factor greater than 2, indicates that there is tunneling of carriers [2]. Note, that the SiLENSe modeling did not model defects at the interface, therefore the exact origin of the carrier tunneling is unknown. For the device with abrupt transitions, the series resistance varied between ~ 1.99×10^{-5} – 7.4×10^{-3} Ω-cm^2 for decreasing hole concentration and the ideality factor was found to be ~ 1.9.

Figure 6.7 shows the simulated band diagram of the p-GaN/i-$In_xGaN_{1-x}N$/n-GaN solar cell. As the acceptor concentration is reduced from 1×10^{21} cm^{-3} to 1×10^{16} cm^{-3} the material becomes more intrinsic as evidenced in the downward shift in the GaN conduction and valence band. Evidence of intrinsic material is most pronounced in the 1

$\times 10^{16}$ cm^{-3} curve, where the p-GaN region is not flat. Optimal performance of the device requires larger acceptor concentration in the p-GaN emitter.

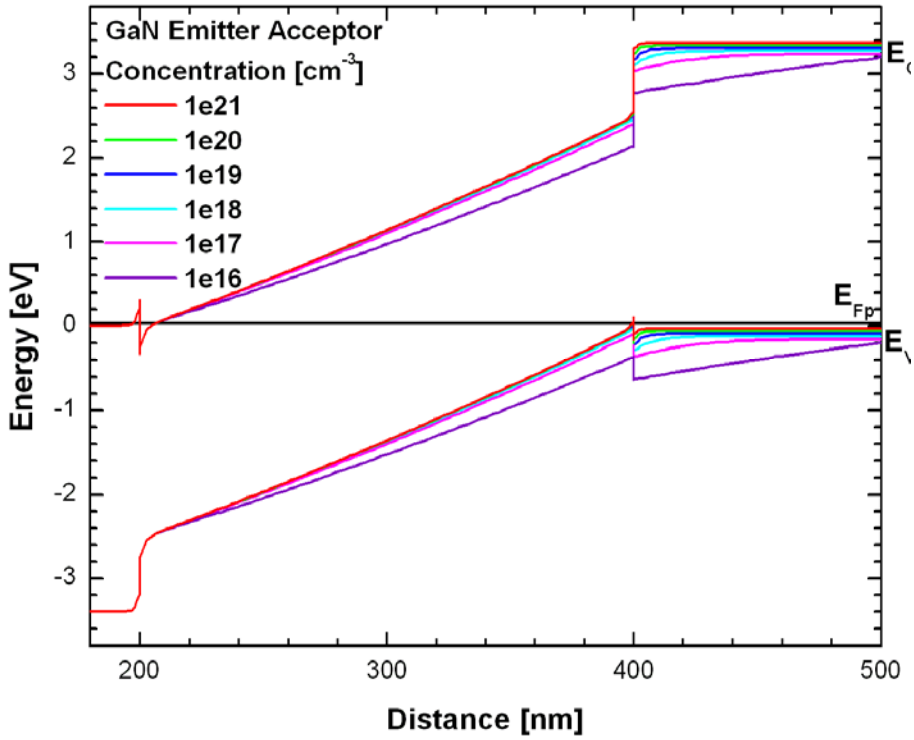

Figure 6.7 – Simulated band diagram of Figure 6.2(c), a p-GaN/i-$In_xGa_{1-x}N$/n-GaN solar cell with various doping concentrations in the p-GaN emitter.

Figure 6.8 show similar results for Figure 6.2(d) where graded junctions were introduced between the n-GaN and p-GaN contact layers. The sample with the graded junction had series resistance that varied between ~ 2.1×10^{-5} – 1.1×10^{-2} Ω-cm^2 for decreasing hole concentration and ideality factor of ~ 1.9. The band diagram with various hole concentration in the p-GaN emitter, shows minimal change indicating that this graded junction cell design is less sensitive to changes in material properties.

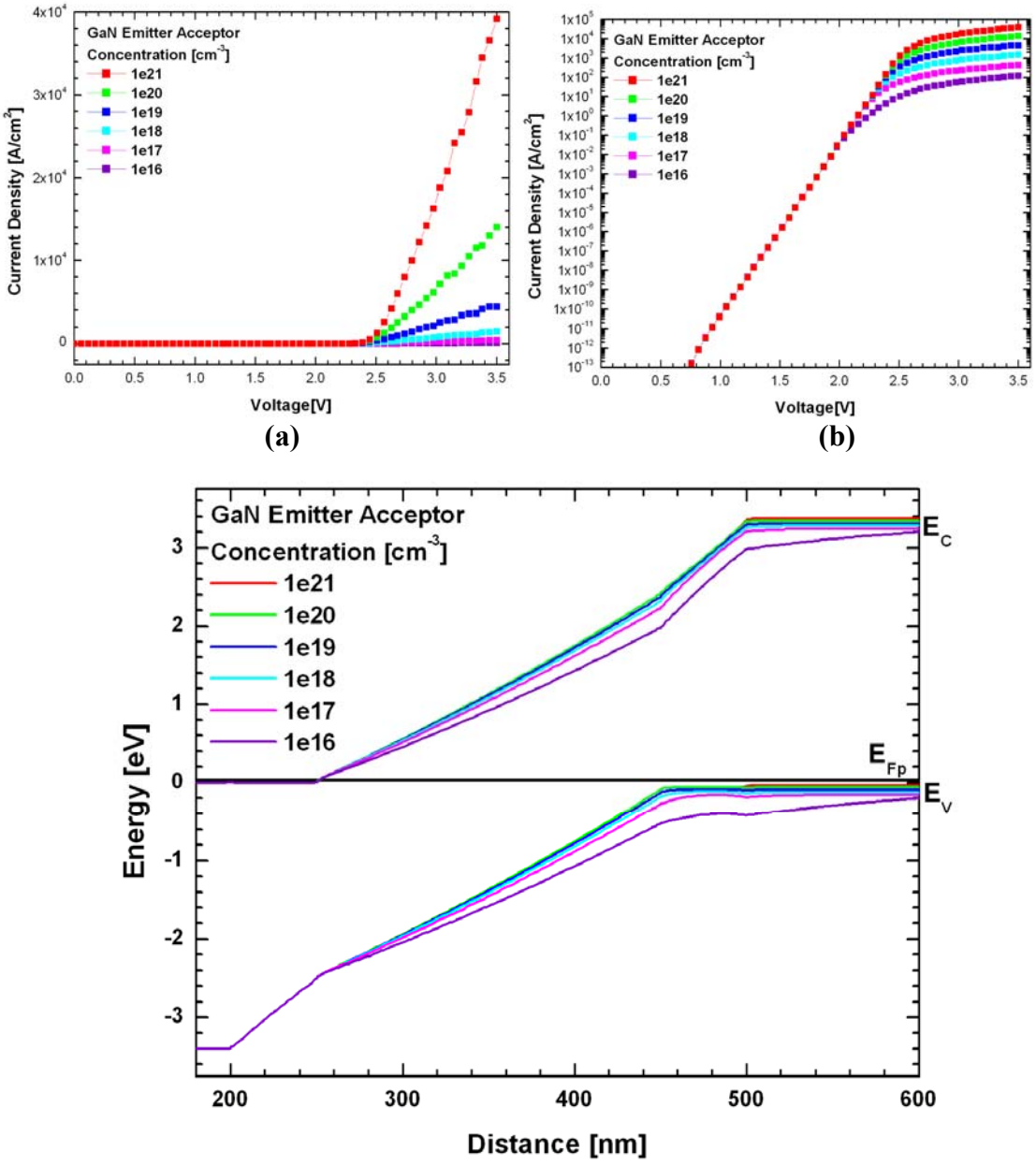

Figure 6.8 – Dark I-V curve of Figure 6.2(d), a p-GaN/grade/i-$In_xGa_{1-x}N$/grade/n-GaN solar cell on a (a) linear scale and (b) logarithmic scale. (c) Simulated band diagram of Figure 6.2(d), with various doping concentrations in the p-GaN emitter.

The simulated dark I-V curves will be compared with the fabricated device results. Deviations from the modeled results will be used to determine the root cause of any device failures.

6.2. Growth Conditions

Four, two-inch Al_2O_3 samples were used in this study. The Al_2O_3 samples were loaded into the growth chamber and then nitrided for 30 minutes with a substrate temperature of 300 °C. All layers used a plasma power of 350 W, a nitrogen flow rate of 1.3 sccm, and Mg-doped layers used a Veeco corrosive series cracker with the cracker bulk and tip were maintained at 300 °C and 900 °C, respectively.

The AlN buffer was grown at a constant substrate temperature of 700 °C with an Al flux of 4.9×10^{-7} torr BEP, and used the MME technique with 10 sec open / 10 sec closed duty cycle.

The GaN:Si was grown following the results presented in Chapter 4.2; constant substrate temperature of 600 °C with Ga flux of $8.5 \times 10^{-7} – 1.0 \times 10^{-6}$ torr BEP, Si cell temperature of 1220 °C, and used the MME technique with 10 sec open / 10 sec closed duty cycle.

The i-$In_xGa_{1-x}N$ was grown with a constant substrate temperature of 400 °C, with Ga flux of $3.5 – 5.0 \times 10^{-7}$ torr BEP, In flux of $1.57 – 2.0 \times 10^{-7}$ torr BEP, and used the MME technique with 10 sec open / 10 sec closed duty cycle. The film was compensated with Mg with the valve position set open at 60 mils.

The GaN:Mg was grown following the results presented in Chapter 4.1; constant substrate temperature of 500 °C with Ga flux of $5.0 – 7.5 \times 10^{-7}$ torr BEP, the valve position set open at 120 mils, and used the MME technique with 5 sec open / 10 sec closed duty cycle.

The grades used between the n-GaN/i-$In_xGa_{1-x}N$ and i-$In_xGa_{1-x}N$/p-GaN were limited by the Eurotherm temperature control system. The effusion cells have one decimal place

degree of freedom, whereas the substrate temperature controller was set to two decimal places. As such the slowest ramp rate for the effusion cells was 0.1 °C/sec and was set for the Ga and In effusion cell for both device grades. The effusion cell ramp rate determined the ramp rate for the substrate temperature. The substrate ramp rate was determined by the substrate temperature difference between each layer divided by the total time of the Ga/In effusion cell ramp. As an example, grading between the n-GaN/i-$In_xGa_{1-x}N$ required a Ga cell temperature change of 50 °C with the ramp rate of 0.1 °C/sec, therefore total time was 500 seconds. The substrate temperature difference was 200 °C, 200 °C divided by 500 seconds results in a ramp rate of 0.4 °C/sec. The MME technique was maintained throughout the grade with 10 sec open / 10 sec closed duty cycle.

Figure 6.9 shows the XRD ω-2θ of the four samples. The black and red curves targeted 20% In with optimal growth conditions and with grades between the GaN and i-$In_xGa_{1-x}N$ layers. The green and blue curves targeted 12% In with graded transitions and with abrupt transitions, respectively. The rest of this chapter will refer to the samples by their sample number N2799, N2821, N2819, N2820 for the black, red, green, and blue curve, respectively.

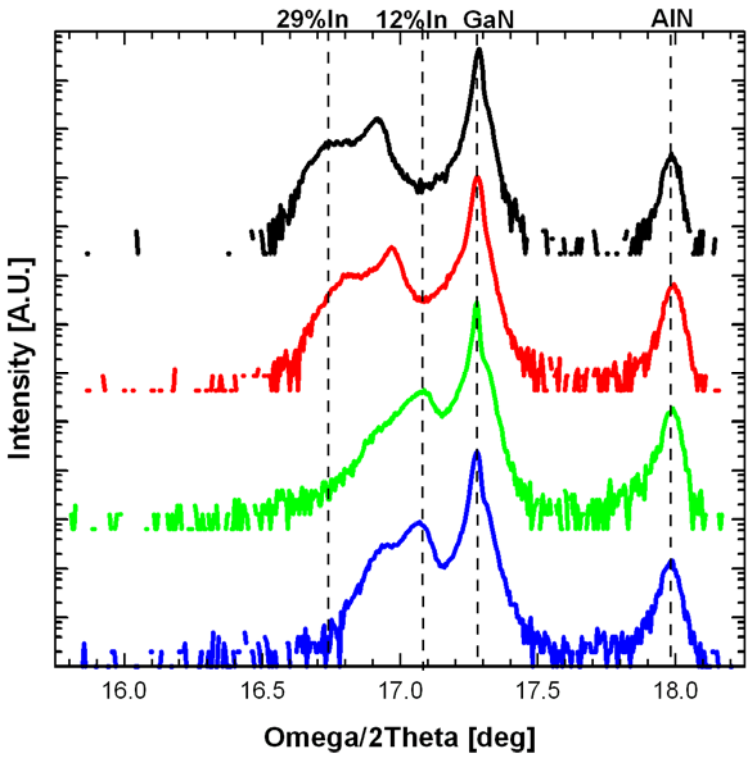

Figure 6.9 – XRD results from the devices that were fabricated. The black, red, and green curves had compositional grades with controlled doping. The black (N2799) and red (N2821) curves used optimal growth conditions. The green (N2819) and blue (N2820) curves used identical growth conditions with the blue curve having abrupt transitions between the GaN and $In_xGa_{1-x}N$ layers.

Previously, phase separation was presented as either compositional or structural. Also, presented was the elimination of compositional phase separation by increasing the growth rate. The $In_xGa_{1-x}N$ grown for the solar cell devices had a growth rate of ~ 0.67 μm/hr; fast enough to grow without compositional phase separation. Unfortunately, the samples did show phase separation in the XRD ω-2θ as shown in Figure 6.9 Chapter 7 will explore in more detail which phase separation, compositional or structural can be attributed to the lower angle shoulders.

6.3. Fabrication Results

6.3.1. Mask Layout

The mask set used was developed at Georgia Institute of Technology based on device sizes dictated by DARPA and the Very High Efficiency Solar Cell (VHESC) program. The mask has 16 solar cell devices with interdigitated fingers with various test structures in a 1" area. The 16 solar cell devices range in area from, 0.18×0.18 cm^2, 0.18×0.35 cm^2, and 0.35×0.35 cm^2, with p-type spreading metal on all the devices except half of the 0.18×0.18 cm^2. The interdigitated fingers were either 5 μm or 10 μm wide and the n-type trench was either 15 μm or 30 μm wide. Figure 6.10(a) shows a screen capture of the mask layout used for the solar cell structure in the fabrication and testing. Figure 6.10(b) shows a specific device with area 0.18×0.35 cm^2, 10 μm wide interdigitated fingers, and 90 μm spacing between the interdigitated fingers. The grey color represents the mesa structure, the red color represents the p-type metal, the dark blue color represents the n-type contact, and the light blue color (easily seen in the bus bar in the lower right hand corner) represents the n-type trench. The spreading metal for the p-type contact was not included for clarity. The mask also has various diagnostic structures including transfer length measurement (TLM), metal resistance measurement, hall measurement and capacitance voltage measurement structures.

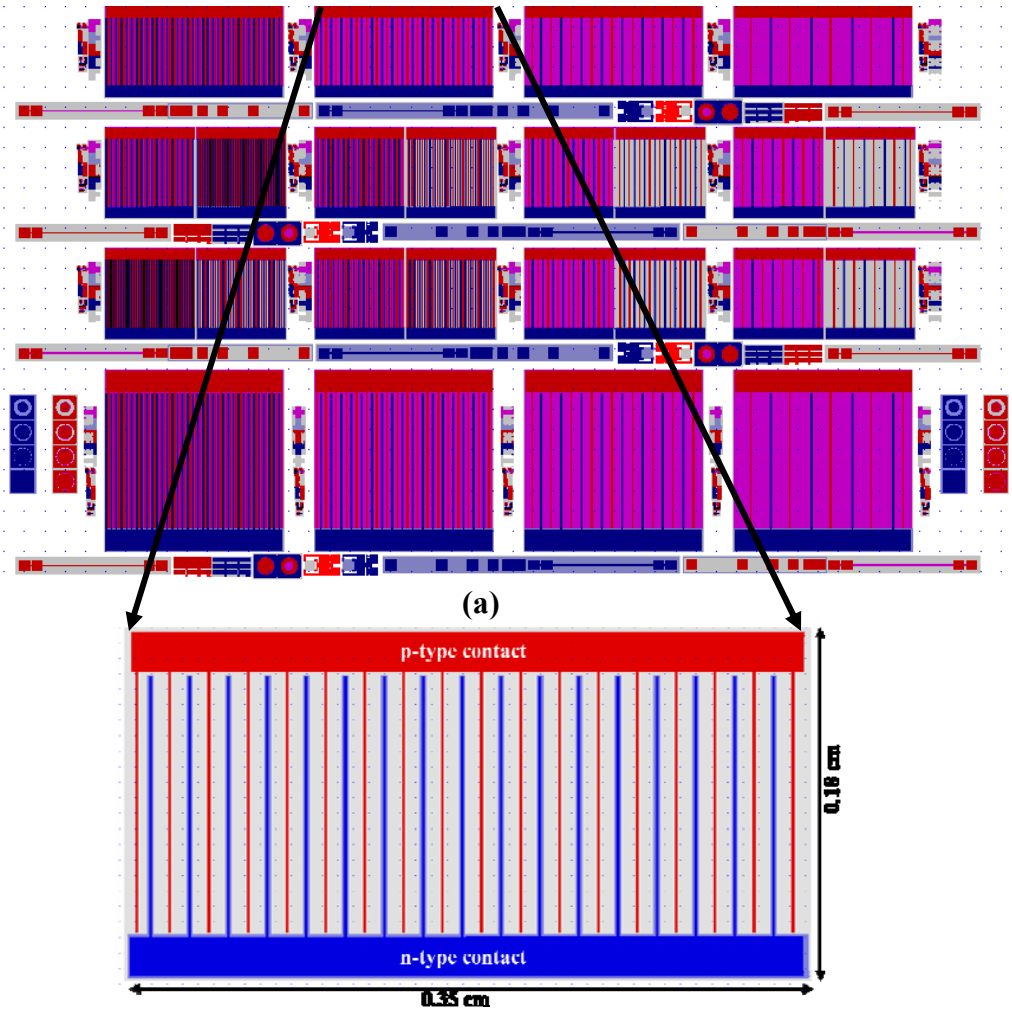

Figure 6.10 – Screen capture of the (a) mask layout and (b) grid contact used in the fabricated devices.

6.3.2. Plasma Etching Optimization

Appendix D outlines the optimized fabrication process that was developed. During the optimization process it was determined that the previous GaN inductively coupled plasma (ICP) etch recipes attacked the trench sidewalls, as shown in the SEM images in Figure 6.11(a). Based on an ICP etch study on GaN, AlN, and InN films as a function of BCl_3/Cl_2 flow ratios, cathode RF-power, and ICP-source power by Shul et al. [115], multiple recipes were tested with varying the cathode RF-power (RF1) from 20 – 250 W

and maintaining a constant ICP-source power (RF2) at 500 W. Shul et al. state that the ICP-generated BCl_3/Cl_2 plasma yields a highly versatile GaN etch process with superior selectivities compared to individual BCl_3 and Cl_2 chemistries. Increased RF1 results in more efficient breaking of the III-N bonds and sputter desorption of the etch products at higher ion energies. Table 6.2 includes the initial and optimized GaN etch recipes.

Table 6.2 – Inductively coupled plasma GaN etch recipes.

	Cl2 [sccm]	BCl_3 [sccm]	Ar [sccm]	H_2 [sccm]	RF1 [W]	RF2 [W]
Old recipe	22.5	0.0	4.0	2.5	25	500
Optimized recipe	32.0	8.0	5.0	0.0	70	500

The optimized GaN trench etch results are shown in the SEM images in Figure 6.11(b) and (c) using a combination of thick SiO_2 layer and photoresist mask.

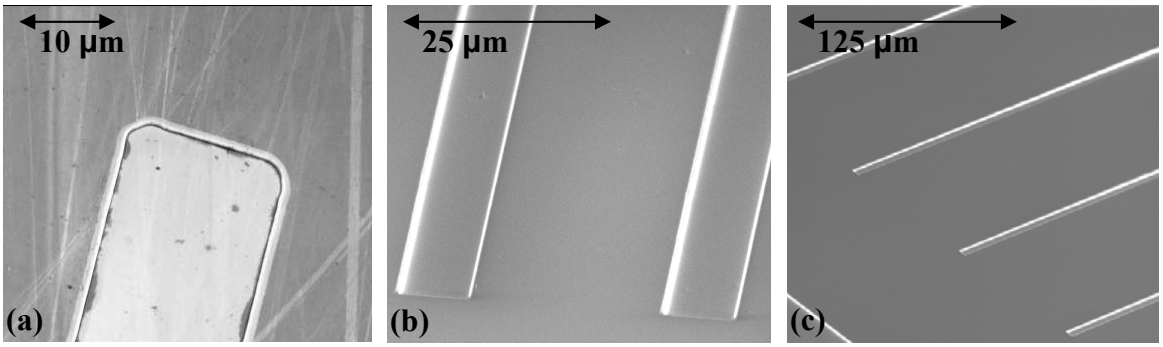

Figure 6.11 – SEM images of (a) original GaN trench etch, (b) and (c) optimized GaN trench etch.

Additionally, because of the trench length, ~ 3 mm, misalignment of the trench metal could create a short in the device. A thin conformal SiO_2 was added to the process steps directly after the trench etch. The thin SiO_2 is then etched back to open the bottom of the trench for contact metallization. This etch requires no lithography step, because the thickness of the SiO_2 is ~ 5× larger on the sidewalls as compared to the top of the trench,

see Appendix D, Figure D. 1(f) – (h) for an illustration. Figure 6.11 shows the SEM images of the optimized GaN etch with the thin SiO_2 sidewalls.

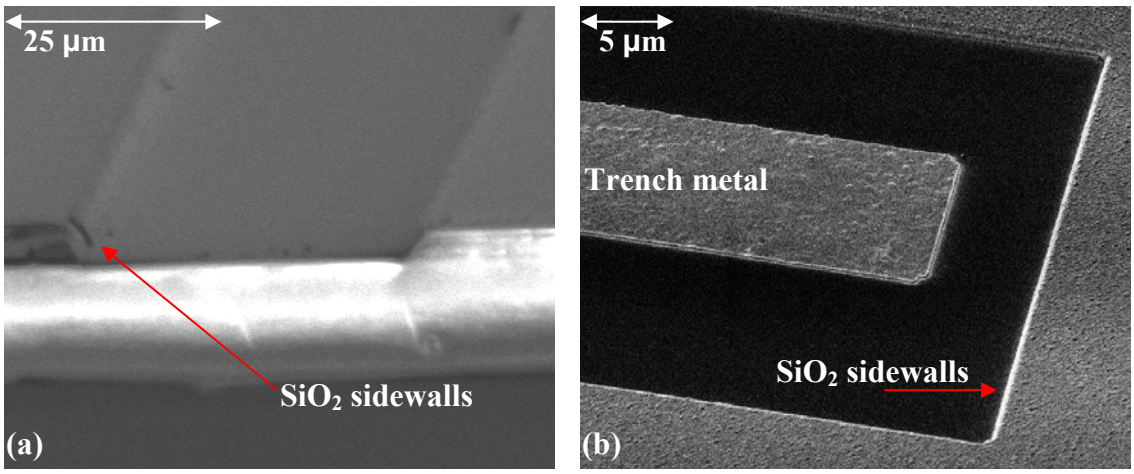

Figure 6.12 – Optimized GaN trench etch with SiO_2 sidewall passivation.

It was also determined that a leakage path exists along the trench sidewall in the absences of the thin SiO_2. Figure 6.13(a) shows I-V curves of an $In_xGa_{1-x}N$ device without the thin SiO_2, showing that there is a current path along the side of the trench. For comparison, and I-V was measured between two equally spaced metal pads located at the bottom of the trench. This resulted in noisy output, shown in, Figure 6.13(b), indicating that there is no current path between the two pads and confirming that there is a current leakage path along the trench sidewall. Pande et al. reported on the use of an insulating barrier over the edges of the grain boundaries in polycrystalline GaAs solar cells [116]. GaAs solar cells had very leaky reverse characteristics, which resulted in low open-circuit voltage. The authors deposited a thick layer of anodic oxide over the edge of the grain boundary, resulting in reduction of the leakage current of the diode by a factor of 10^5 – 10^6. Therefore, the thin sidewall SiO_2 should also passivate the sidewall and eliminate current leakage path along the trench sidewalls.

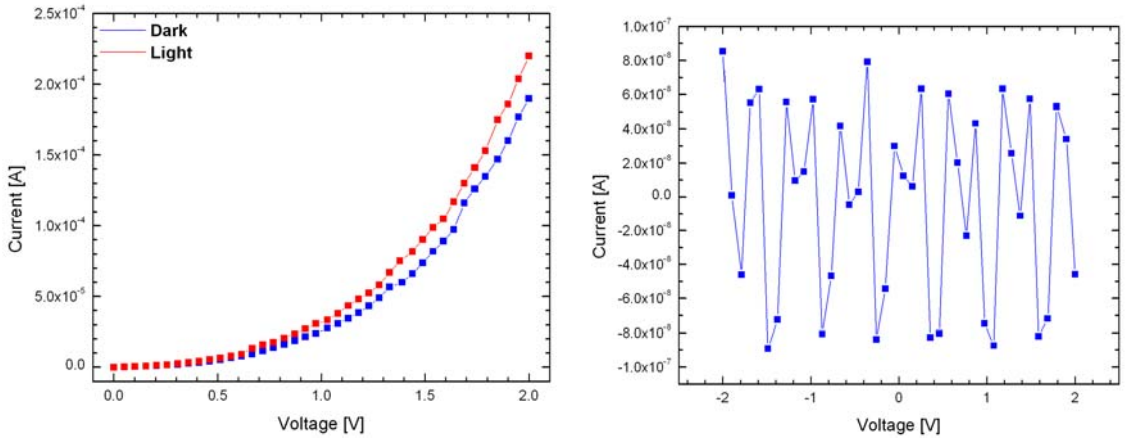

(a) **(b)**

Figure 6.13 – I-V curve showing (a) current leakage path along the top and bottom of the trench and (b) open connection between two equally spaced metal pads located at the bottom of the trench.

6.4. Device Results

Samples N2799, N2819, N2820, and N2821 were fabricated following the steps outlined in Appendix C. All the devices were tested before the final p-type ohmic anneal. As stated in Chapter 1, the measurements were conducted in-house with four-point measurements with a Keithley 2410 source meter. The light measurements used a SoLux lamp, operating at 4.0 A and 11.0 V replicating natural daylight. Figure 6.14 shows the results of the tested devices. Figure 6.14(a) and (b) targeting 20% In incorporation with graded transitions. Figure 6.14(c) and (d) targeted 12% In incorporation with graded transitions and with abrupt transitions, respectively.

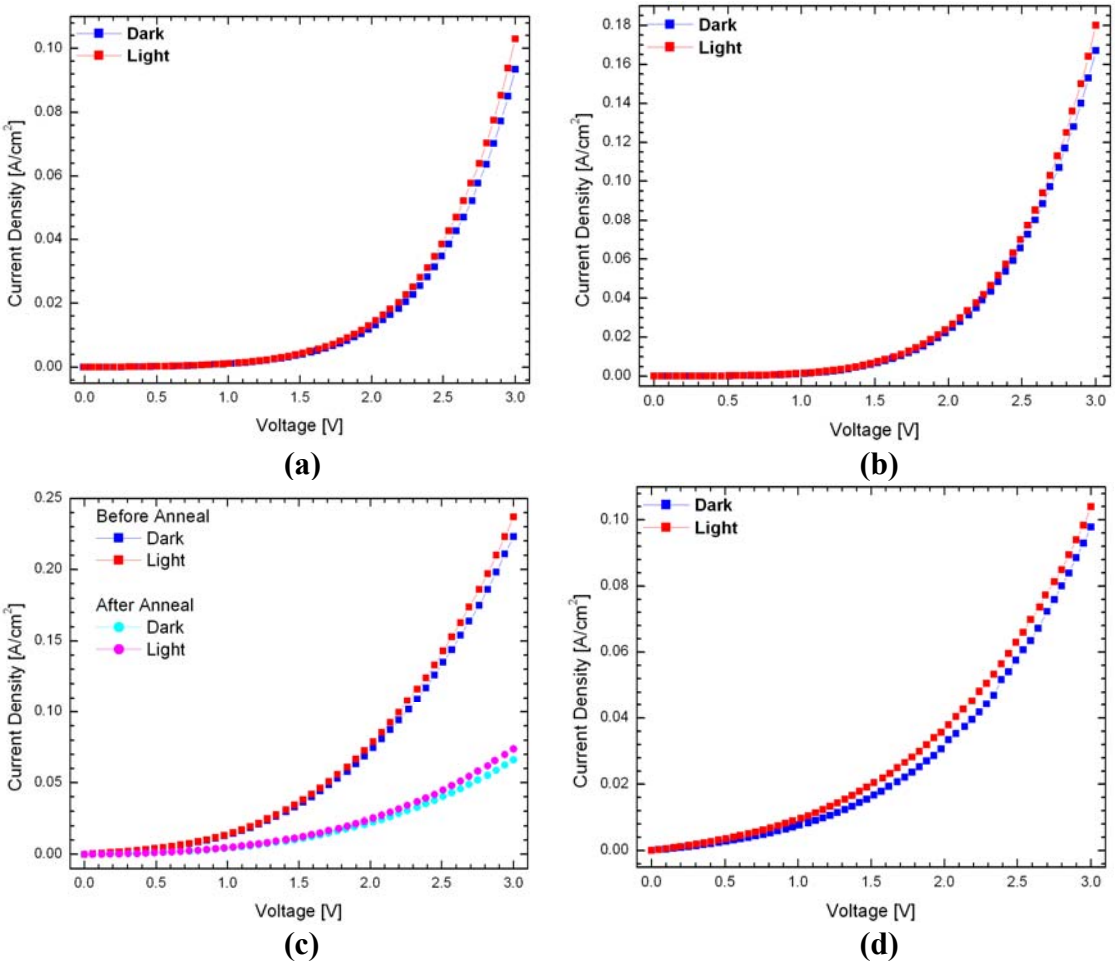

Figure 6.14 – Measured I-V curves on (a) N2799, (b) N2821, (c) N2819 with before and after the sample was annealed, and (d) N2820.

The I-V results show that all the devices have no photovoltaic effect. Sample N2819 was annealed following step 8.4 in Appendix D, after initial measurements. The results are shown in Figure 6.14(c) denoted by circles. The device performance is significantly reduced. The current density at 3.0 V was approximately 0.25 A/cm^2 before the annealing step and approximately 0.07 A/cm^2 after the annealing step. This result indicates that annealing the sample results in device deterioration and no improvement, as expected in the alloying of the ohmic contact metal.

Comparing the modeled I-V curve from SiLENSe with the actual device I-V curves, Figure 6.15 shows the device dark I-V results (solid circles) with the SiLENSe results for

a sample with graded junctions (open triangles) and abrupt junctions (solid triangles). The device results and the modeled results are significantly different; indicating that the model is either too simplified or that there is an interaction between the layers that was unaccounted for. The dark I-V curves of the fabricated devices are dominated by series resistance; therefore we are not able to determine the diode ideality factor. The series resistance from the dark I-V curves ranged from 0.6 - 24 Ω-cm^2 for all 5 samples. These values are significantly larger than the SiLENSe modeled values. The following section will discuss in detail multiple device failure analysis tests used to determine the root cause for the lack of photovoltaic response.

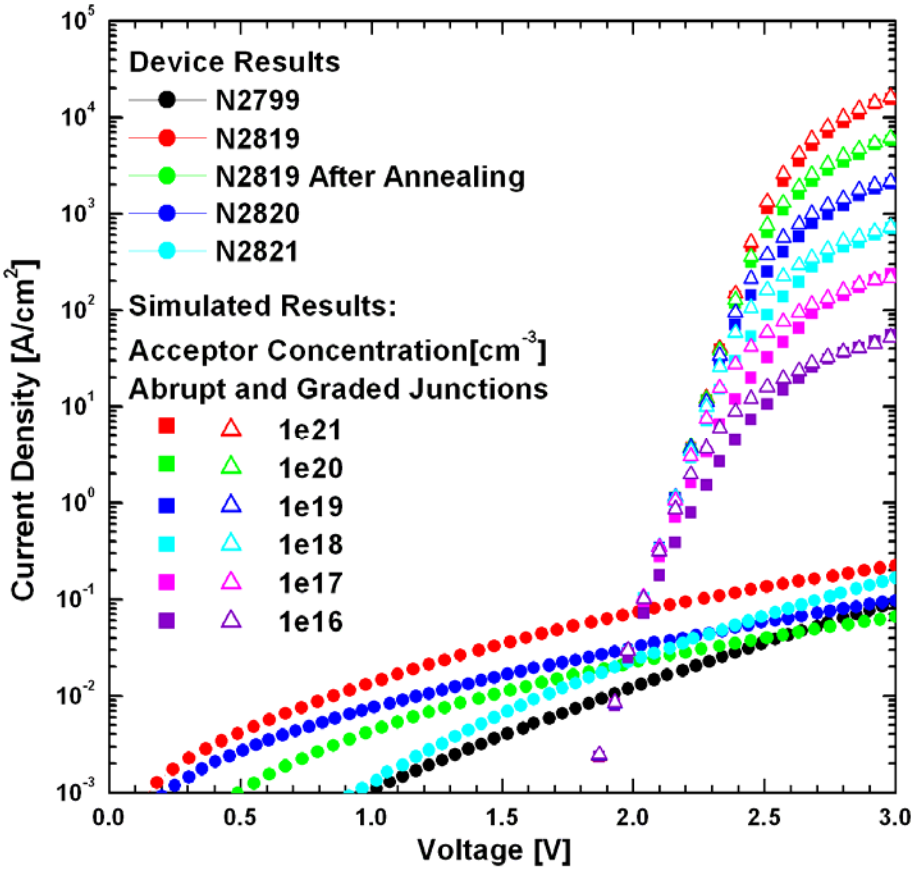

Figure 6.15 – Dark I-V curves of the fabricated devices (solid circles) and SiLENSe simulated results with abrupt junctions (solid squares) and with graded junctions (open triangles) for various hole concentrations in the p-GaN emitter.

6.5. Summary

This chapter presented device modeling simulations from SiLENSe including dark I-V curves that were compared with the fabricated device results. SiLENSe modeling determined that i-$In_xGa_{1-x}N$ is sufficient as compared to n- and p-$In_xGa_{1-x}N$ layers and that the devices required graded transitions between the i-$In_xGa_{1-x}N$ and the GaN emitter and base. The fabrication process was optimized with a new ICP etch recipe resulting in linear, vertical, passivated trench as evidenced in SEM images.

The combination of the SiLENSe modeling results, optimized etch recipe, and individual growth techniques presented in the previous chapters, four solar cells were grown and fabricated. Unfortunately, the devices did not show any photovoltaic effect, leading to a thorough device failure investigation. The next chapter will discuss the failure analysis.

CHAPTER 7: Failure Analysis

Upon discovery that the devices have no photovoltaic effect, the devices were thoroughly tested to determine the root cause of the failure. It was proven that the individual layers, n-GaN and p-GaN have outstanding individual electrical properties as measured by Hall effect measurements. Therefore, the devices may have experienced unexpected interactions when grown in series. Fortunately, the fabrication mask set has multiple analysis structures: simple diode structures, linear transfer length method (TLM) pads, circle TLM pads, resistor structures, and Hall effect structures. The linear TLM structures on the n- and p-type material determined the sheet and contact resistance, as well as the specific contact resistivity. Hall effect measurements were conducted on i-$In_xGa_{1-x}N$ to determine the resistivity which in turn dictates the depletion volume in the device. Additionally, XRD ω-2θ and pole-figures were completed to determine the crystal quality.

7.1. Hall Effect Measurements on i-$In_xGa_{1-x}N$

Chapter 3 discussed the propensity of InN and high In incorporation $In_xGa_{1-x}N$ to be strongly compensated. An unintentionally doped (UID) $In_xGa_{1-x}N$ sample, with 20% In incorporation, was found to be n-type with electron concentration of 8.4×10^{18} cm^{-3}, resistivity of 0.26 Ω-cm, and mobility of 2.9 cm^2/Vs. This large unintentionally doped electron concentration will reduce the depletion volume. It has been estimated that the reduction in electron density, will result in increased photocurrent and an associated increase in the open circuit voltage and fill factor.

Minute amounts of Mg were added to the $In_xGa_{1-x}N$ to compensate the electron concentration. A Mg flux of 3.5×10^{-10} torr BEP, resulted in mixed conductivity (which occurs when the mobility is too small, resulting in an immeasurable Hall voltage) and a resistivity of 1.4 Ω-cm. Additionally, a Mg flux of 3.8×10^{-10} torr BEP, also resulted in mixed conductivity and a resistivity of 4.1 Ω-cm. Figure 7.1 shows the complete results from the undoped and compensated $In_xGa_{1-x}N$ films.

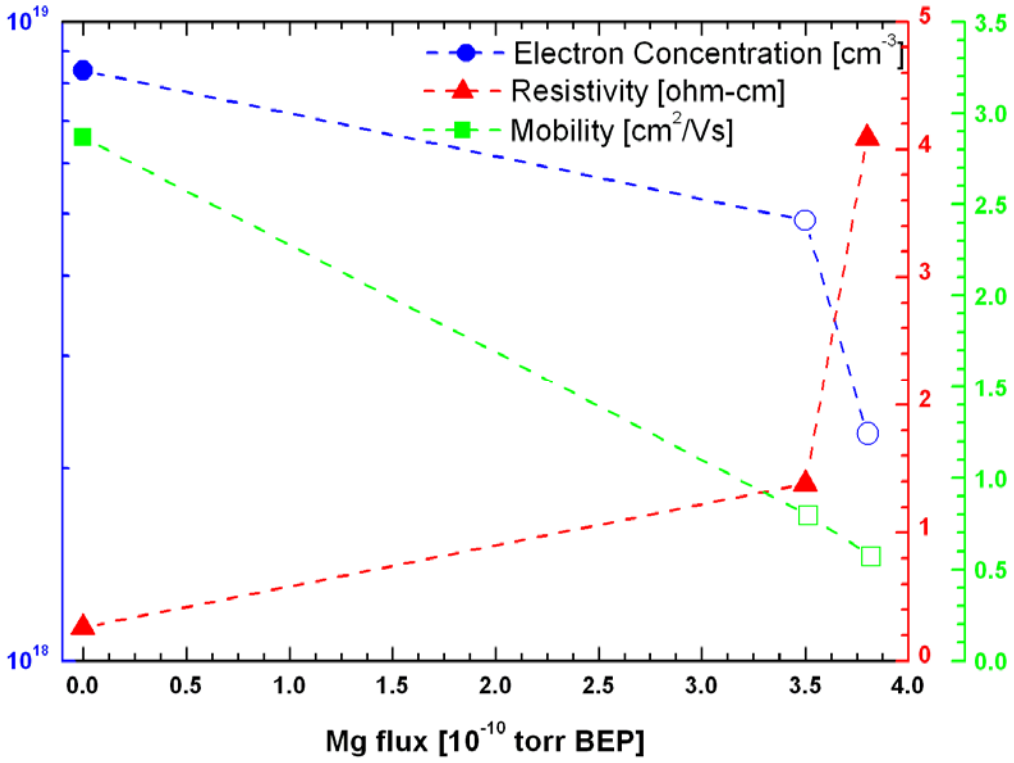

Figure 7.1 – Electrical characteristics of i-$In_xGa_{1-x}N$ using MME for different Mg fluxes. The open circles indicate the samples with mixed conductivity.

The solar cell devices were doped with a Mg flux of 3.8×10^{-10} torr BEP in the i-$In_xGa_{1-x}N$ layers, resulting in mixed conductivity with a concentration estimated as ~ 2×10^{18} cm^{-3}, which is significantly larger than the targeted compensated values (~10^{16} cm^{-3}) used in the SiLENSe models. Recall that the depletion volume is related to the carrier concentration in the i-region, as the i-region carrier concentration increases the depletion

volume decreases. EPHs generated in the depletion region will be swept across the junction by an electric field and produce photocurrent. EHPs generated more than a diffusion length away from the depletion region will recombine and not contribute to the photocurrent. A decreased depletion volume will have fewer EHPs that are swept across the junction and in turn have a reduced photocurrent.

Figure 7.2 shows the SiLENSe band diagram of an n-GaN/i-$In_xGa_{1-x}N$/p-GaN device with the carrier concentration in the i-region of 10^{16} cm^{-3} (dotted line), 10^{17} cm^{-3} (dashed line) and 10^{18} cm^{-3} (solid line). The size of the depletion volume decreases with increasing carrier concentration in the i-region. The i-$In_xGa_{1-x}N$ in the devices had a carrier concentration of ~10^{18} cm^{-3} in the i-region, therefore this region was not completely compensated resulting in a minuscule depletion volume and is one cause of the poor I-V curves presented in Figure 6.14.

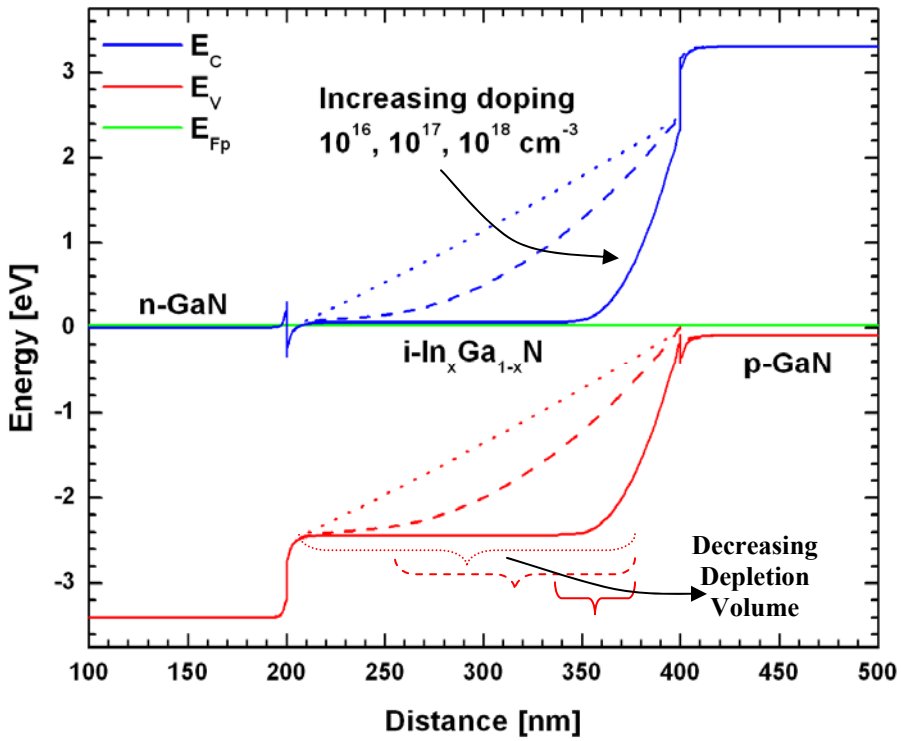

Figure 7.2 – Simulated band diagram of Figure 6.2(c), with various doping concentrations in the i-$I_xGa_{1-x}N$.

7.2. Pole-Figure

Chapter 3.3 discussed in detail the formation of zinc-blende phase material with Mg doping in $In_xGa_{1-x}N$ material. The samples used in that study had Mg fluxes in excess of 1×10^{-8} torr BEP and mixed zinc-blende/wurtzite material was found irrespective of In incorporation. The solar cell devices used Mg compensated i-$In_xGa_{1-x}N$ layer with a Mg flux of 3.8×10^{-10} torr BEP, more than 2 orders of magnitude less than flux used to create mixed zinc-blende/wurtzite material. The Mg flux used in the i-$In_xGa_{1-x}N$ device layer is similar to the study in Chapter 3.4, where there was no evidence of zinc-blende material. As such, the device structures should have no evidence of zinc-blende material.

An XRD pole-figure was conducted on the devices (N2799, N2819, N2820 and N2821) and found zinc-blende material at $\psi = 29$ °, as evidenced in a representative scan of N2799, shown in Figure 7.3(c). The peaks labeled I, II, III, and V are associated with the mixture of wurtzite {20-21} $In_xGa_{1-x}N$ and the Al_2O_3 substrate peak, wurtzite {11-22} $In_xGa_{1-x}N$, zinc-blende {311} III-N, and the {21-34} Al_2O_3 substrate peak, respectively. The intensity of the wurtzite $In_xGa_{1-x}N$ peaks are significantly larger than the zinc-blende $In_xGa_{1-x}N$ peaks, indicating that the device layers are predominately wurtzite.

Figure 7.3(a) and (b) investigated the calibrated III-N epilayers: Mg-doped $In_xGa_{1-x}N/AlN/Al_2O_3$ and p-$GaN/AlN/Al_2O_3$, finding no evidence of zinc-blende material. The peaks found in the Figure 7.3(a) are related to the mixture of wurtzite {20-21} $In_xGa_{1-x}N$ and the Al_2O_3 substrate peaks, the wurtzite {11-22} $In_xGa_{1-x}N$ peaks, the {21-34} Al_2O_3 substrate peaks, labeled I, II, and V, respectively. The only peaks found in Figure 7.3(b) are related to the mixture of wurtzite {20-21} GaN with the Al_2O_3 substrate peak, and wurtzite {11-22} GaN, labeled VI and VII, respectively. Note that the corresponding

Hall results and FWHM ω-scans for the sample in Figure 7.3(b) are shown in Figure 4.4 for a Ga flux of 7.0×10^{-7} torr BEP.

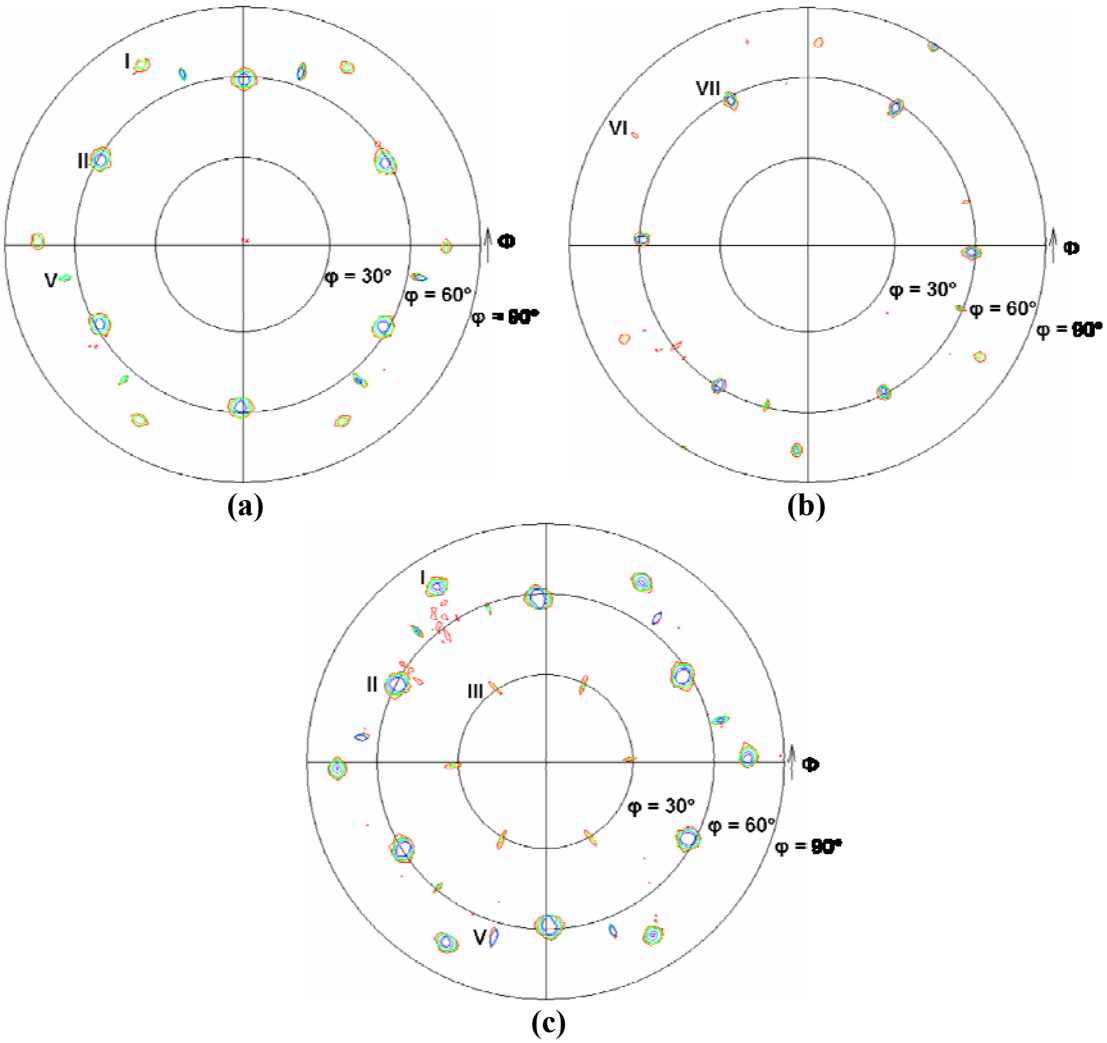

Figure 7.3 – Pole-figure of (a) i-$In_xGa_{1-x}N$/AlN/Al_2O_3, (b) p-GaN with hole concentration equal to 1×10^{19} cm^{-3}, and (c) N2799 p-GaN/grade/i-$In_xGa_{1-x}N$/grade/n-GaN solar cell. The labeled peaks are: I – the mixture of wurtzite {20-21} $In_xGa_{1-x}N$ and the Al_2O_3 substrate peaks, II – wurtzite {11-22} $In_xGa_{1-x}N$ peaks, III – zinc-blende {311} III-N peaks, V – the {21-34} Al_2O_3 substrate peaks, VI – the mixture of wurtzite {20-21} GaN and the Al_2O_3 substrate peaks, and VII – wurtzite {11-22} GaN peaks. ϕ is the angle relative to the normal surface.

The calibrated samples did not have evidence of zinc-blende material, therefore it is likely that the there is an interaction at the interface between the i-$In_xGa_{1-x}N$ and the p-GaN, creating zinc-blende material. Figure 7.4 shows an ω-2θ scan optimized on the {11-29} Al_2O_3 reflection to determine which epilayer, i-$In_xGa_{1-x}N$ or p-GaN is zinc-

blende. The dotted lines indicate the position of the {311} zinc-blende GaN, the {10-13} wurtzite AlN, and the {10-13} wurtzite GaN. The highlighted area is the ω-2θ sampling window used in the pole-figures.

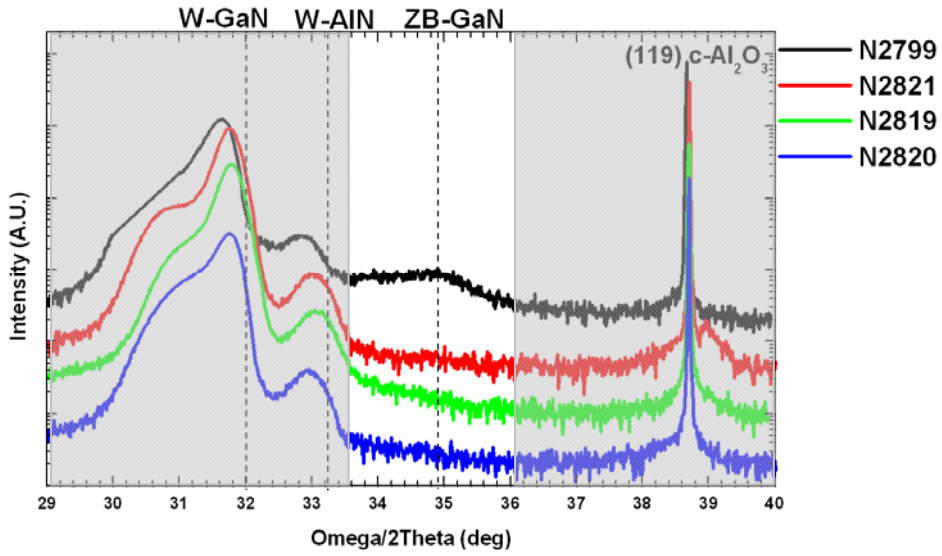

Figure 7.4 – XRD ω-2θ scan optimized on the {11-29} Al_2O_3 peak for solar cell devices. The dotted lines indicate the position of {311} zinc-blende GaN, the {10-13} wurtzite AlN, and {10-13} wurtzite GaN. The ω-2θ window region was the sample space used in the pole-figure in Figure 7.3(c).

Sample N2799, has a broad {311} zinc-blende GaN peak located at ω = 34.90 °, indicating that both i-$In_xGa_{1-x}N$ and GaN are mixed zinc-blende and wurtzite. The other devices show minimal zinc-blende $In_xGa_{1-x}N$, which correlates with the low intensity zinc-blende peaks found in the pole-figures and show no evidence of zinc-blende GaN. Therefore, the zinc-blende material originated in the i-$In_xGa_{1-x}N$ and in sample N2799 the zinc-blende structure propagated into the p-GaN.

The presence of zinc-blende material in the solar cell devices and the lack of zinc-blende material in the i-$In_xGa_{1-x}N$ and p-GaN calibration samples could have been a cause for the lack of photovoltaic response in the devices. The zinc-blende "defect" in the wurtzite material act similarly to quantum wells in the active region restricting the

flow of carriers through the depletion volume and would be evidenced in an increased ideality factor. Unfortunately, the dark I-V curves are dominated by series resistance as was shown in Figure 6.15, so the ideality factor cannot be extracted.

The I-V curves shown in Figure 6.14 and the results presented in the following sections, indicated that the major device failure was the reduced hole concentration in the p-GaN emitter and not the formation of zinc-blende material. Chapter 8 will discuss future research to eliminate the interaction between the i-$In_xGa_{1-x}N$ and p-GaN.

7.3. Transfer Length Method

The TLM is used to determine the quality and characteristics of the metal-semiconductor contact. The metal contacts must supply the required device current. It should also have a voltage drop across the contact that is small compared to the voltage drop across the active device region [117]. The metal contacts are either referred to as Schottky or Ohmic based on a distinctly non-linear or linear I-V characteristic, respectively. An Ohmic contact is desirable. The TLM test measures the total resistance between successive metal-semiconductor pads and plotted versus the spacing between pads. The TLM structures in the mask set had square pads with 200 μm height and width and pad spacings of 25 μm, 100 μm, 200 μm, 400 μm, and 800 μm. Figure 7.5(a) shows an example TLM structure and the associated results plotted as total resistance versus contact spacing.

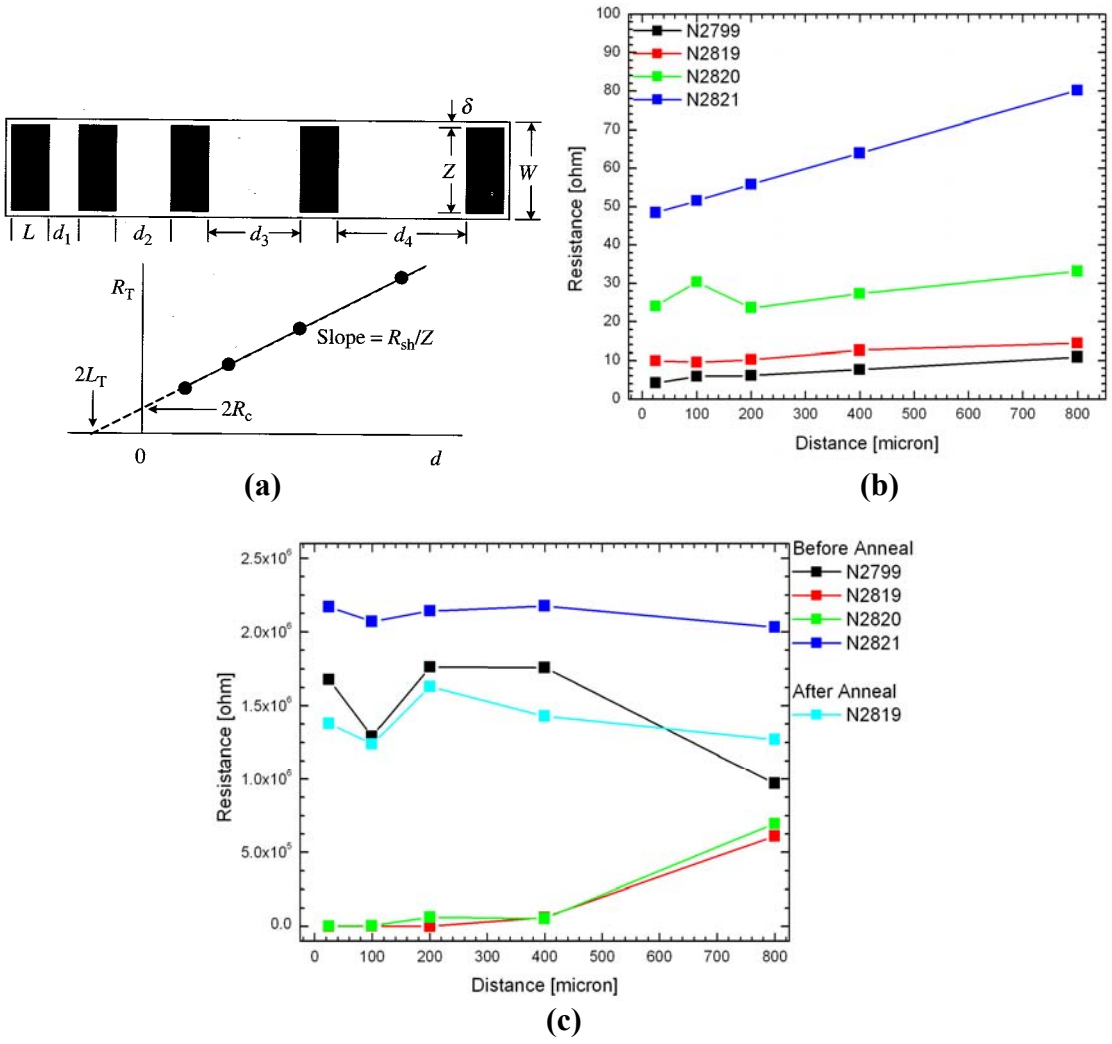

Figure 7.5 – (a) Diagram of TLM test structure and a plot of the total resistance as a function of the contact spacing [117]. TLM results for the four fabricated device (b) n-type metal-semiconductor contact and (c) p-type metal-semiconductor contact.

Figure 7.5(b) and (c) show the TLM results for the n-type metal-semiconductor and p-type metal-semiconductor contact. The n-type metal used was Ti/Al/Ti/Au and the p-type metal used was Ni/Au. The n-type results are linear, indicating that the contact is ohmic. The values for the sheet resistance, the contact resistance and the specific contact resistivity for the n-type metal-semiconductor are summarized in Table 7.1. The results for the p-type metal-semiconductor contacts are non-linear and the total resistance varies

from the ohm range to the mega-ohm range, indicating that the contact is Schottky in nature.

Table 7.1 – n-type metal-semiconductor TLM data extracted from the results in Figure 7.5(b).

			Sheet Resistance [Ω/]	Contact Resistance [Ω]	Specific Contact Resistivity [Ω-cm^2]	Transfer Length [m]
	slope	intercept	R_{Sh} = slope × pad height	R_C = intercept/2	$\rho = (L_T)^2 \times R_{sh}$	$2L_T$
N2799	7983.01	4.51306	1.6	2.26	1.28E-03	5.65E-04
N2819	6562.13	9.35555	1.31	4.68	6.66E-03	1.43E-03
N2820	9259.4	24.8559	1.85	12.43	3.33E-02	2.68E-03
N2821	40921.3	47.493	8.18	23.75	2.75E-02	1.16E-03

7.4. Series Resistance Analysis

In the previous chapter the series resistance was determined for the two SiLENSe modeled devices (one with graded transitions and one with abrupt transitions), as well as for the fabricated devices. Also mentioned, SiLENSe models the acceptor levels as a single level, however the high hole concentration Mg-doped GaN has banding of the acceptor level. To achieve the high hole concentration emitter, the SiLENSe acceptor level was varied from 1×10^{16} to 1×10^{21} cm^{-3} resulting in the Mg-emitter having hole concentrations from ~ 8×10^{15} to 5×10^{19} cm^{-3}, respectively.

Using the SiLENSe simulated I-V curves; the series resistance was determined and plotted with respect to the acceptor concentration, as shown in Figure 7.6(a). The series resistance exponentially decays with increasing acceptor concentration and does not vary significantly between the structures with graded junctions and abrupt junctions. The series resistance from the fabricated devices is shown in Figure 7.6(b) as a single level.

Note the fabricated devices are color coded to match with I-V results in Figure 6.15. The series resistance for the fabricated devices is significantly larger than the SiLENSe models, indicating that the fabricated devices do not have high hole concentration Mg-doped GaN emitters as expected. It is likely that significant calibration shifts occurred when going from the 1 × 1 cm calibration samples to the 2" diameter device samples.

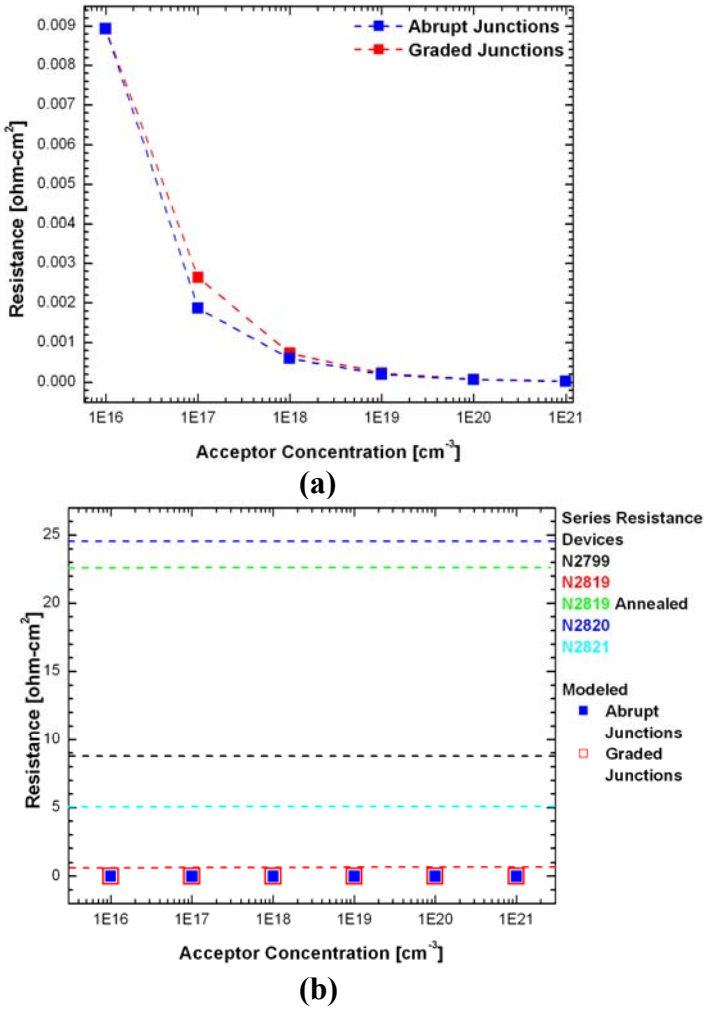

Figure 7.6 – Series resistance versus acceptor concentration from (a) the SiLENSe simulations and (b) the series resistance levels from the measured devices with the SiLENSe simulations.

7.5. Device Annealing

The fabrication process flow presented in Appendix D, mentions annealing the p-type metal to alloy the metals together, creating a better ohmic contact. The success of GaN based devices is the ability to achieve ohmic contacts to p-type material. As was presented in Chapter 4, great strides have been made increasing the level of p-type doping, but achieving low resistivity ohmic contacts still remains a challenge. Typically, the p-type contacts are annealed at temperatures between 400 and 750 °C, resulting in contact resistivities near 1×10^{-2} Ω-cm^2 [118].

Figure 6.14(c) shows the I-V results for sample N2819 before and after annealing. The I-V curve after annealing is significantly worse than before annealing, signifying that the annealing step deteriorated the $In_xGa_{1-x}N$ epitaxial material or reduced the Mg-doped GaN hole concentration, or degrade the p-type metal contacts. Figure 7.7 shows the ω-2θ XRD scan from before the annealing (red curve) and after annealing (blue curve). Note that the before annealing scan was taken on the bare wafer before any fabrication steps and the after annealing scan was taken across the fabricated device. The XRD shows minimal deterioration of the material after annealing and is not the cause of worse I-V results in Figure 6.14(c). Chapter 4 proved that annealing the sample did not impact the p-GaN hole concentration (see Table 4.2), therefore annealing the sample negatively impacted the p-type metal and is the cause of the degraded I-V results. Based on the I-V, TLM, and XRD results the Mg-doped GaN emitter did not achieve the high hole concentration in the solar cell structure as compared to the epitaxial Mg-doped GaN calibration samples.

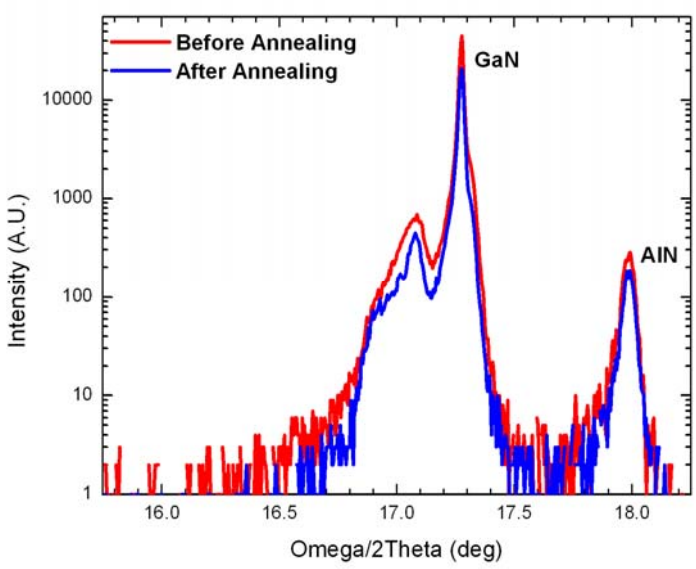

Figure 7.7 – XRD results from before the device (N2819) was fabricated (red curve) and after fabrication, including an annealing step (blue curve). This sample corresponds to the green curve in Figure 6.9.

7.6. Summary

This chapter presented failure analysis results to determine the lack of photovoltaic response in the $In_xGa_{1-x}N/GaN$ heterojunction solar cells. Failure analysis included XRD ω-2θ scans and pole-figure measurements, TLM measurements, and I-V analysis. The failure analysis results lead to the conclusion that the mixture of zinc-blende material originated in the i-$In_xGa_{1-x}N$, the i-$In_xGa_{1-x}N$ was insufficiently compensated, and the hole concentration in the p-GaN is less than optimal, resulting in highly resistive films. The insufficient hole concentration in the p-GaN emitter had the largest negative impact on the devices. The following chapter will discuss the future direction and the additional work necessary to achieve an $In_xGaN_{1-x}N/GaN$ heterojunction solar cell.

CHAPTER 8: Conclusion and Future Work

8.1 Conclusion

The research presented in this thesis has focused on the development of growth parameters for a heterojunction $In_xGa_{1-x}N$/GaN solar cell. $In_xGa_{1-x}N$ solar cells are an exciting material because the alloy has a bandgap that completely spans the visible spectrum, which current solar cells are unable to do. Photovoltaic devices with a bandgap greater than 2.0 eV are attractive because over half the available power in the solar spectrum is above the photon energy of 2.0 eV. The ability of $In_xGa_{1-x}N$ materials to optimally span the solar spectrum offers a tantalizing solution for high-efficiency photovoltaics. $In_xGa_{1-x}N$ solar cells have an added advantage that they have high open circuit voltages. A high voltage solar cell suffers less from series resistance losses when connected in series in a module.

Initial work included the growth of InN on (111)-oriented, Ga-doped germanium substrates and c-plane Al_2O_3 substrates proving that InN has a narrow bandgap, evidenced by a strong PL peak with energy of 0.69 eV. It was also determined that oxygen incorporation affects the crystalline structure of InN, but does not impact the bandgap. It was previously thought that oxygen incorporation was the cause of the higher measured bandgap value of InN.

Using high growth rates, $In_xGa_{1-x}N$ films with In compositions ranging from 1 to 32 % have been grown by MBE with negligible phase separation according to XRD analysis. Transmission data determined that the absorption coefficient of $In_xGa_{1-x}N$ at 2.4 eV was calculated as $\alpha \cong 2 \times 10^5$ cm^{-1} near the band edge. This absorption coefficient

results in an optimal solar cell thickness of less than a micron, resulting in increased material throughput.

A doping growth technique was developed by effectively establishing the periodic buildup and depletion process of Ga atoms, which facilitates the incorporation of Mg dopants into Ga substitutional sites while suppressing the formation of compensating defects. MME has been shown to be a feasible, repeatable, beneficial, and powerful technique capable of growing p-type GaN with nearly 20× improvement in hole concentrations compared to literature standards. Mg-doped GaN with hole concentrations as high as 4.26×10^{19} cm^{-3} and resistivity of 0.5 Ω-cm were achieved at a substrate temperature of 600 °C. The demonstrated capability of high hole concentrations in p-type GaN will expedite the development of future nitride based electronic and optical devices where carrier concentration is correlated with light output.

Device modeling simulations from SiLENSe determined that a single i-$In_xGa_{1-x}N$ layer is sufficient as compared to multiple n- and p-$In_xGa_{1-x}N$ layers, again increasing material throughput. Additionally, the devices require graded transitions between the i-$In_xGa_{1-x}N$ and the GaN emitter and base, otherwise the devices suffer from a strong discontinuity. The fabrication process was optimized with a new ICP etch recipe based on BCl_3/Cl_2 chemistry, resulting in linear, vertical, passivated trench as evidenced in SEM images.

The combination of the SiLENSe modeling results, optimized etch recipe, and individual growth techniques presented in the previous chapters, four solar cells were grown and fabricated. Unfortunately, the devices did not show any photovoltaic effect, leading to a thorough device failure investigation. The failure analysis results lead to the

conclusion that the hole concentration obtained in the smalled calibration samples was not obtained in the larger device wafers, resulting in solar cell devices that are highly resistive and have no photovoltaic response. The following section outlines the future work for a successful heterojunction $In_xGa_{1-x}N$/GaN solar cell.

8.2 Future Work

This thesis presented information about MBE growth of InN and $In_xGa_{x-1}N$ for photovoltaic applications. The properties of the individual layers were shown to have outstanding qualities, but when combined in series shown no photovoltaic response. The future work section will outline steps to improve the solar cell design, leading to photovoltaic response from a MBE grown $In_xGa_{1-x}N$ solar cell.

- **Investigation of p-GaN/ i-$In_xGa_{1-x}N$ Epilayers**

As was presented in Chapter 6, the i-$In_xGa_{1-x}N$ and p-GaN epilayers were only wurtzite as evidenced by XRD pole-figure measurements, but the device structures that included the serial growth of p-GaN/i-$In_xGa_{1-x}N$/n-GaN showed zinc-blende and wurtzite material. Phase separation of the individual i-$In_xGa_{1-x}N$ show no phase separation of the material as substantiated by XRD ω-2θ measurements. The phase separation of the device structures indicates an interaction between the p-GaN and i-$In_xGa_{1-x}N$. A study can be completed were the epitaxial growth of a p-GaN/i-$In_xGa_{1-x}N$/AlN/Al_2O_3 is investigated with XRD and cross-sectional TEM. XRD ω-2θ scans and pole-figures can determine the crystalline structure.

- **Epitaxial Growth Optimization**

In this work the epitaxial layers were optimized on 1 × 1 cm Al_2O_3 substrate pieces because of limited substrates and timely backside metallization. The fabricated devices used 1 × 1 cm Al_2O_3 substrate epilayer calibrations and directly transferred that to 2" Al_2O_3 substrates. The substrate heater is capable of uniform heating for a 3" wafer. However, as verified by the reduced hole concentration for the p-GaN emitter, the

heating of the 2" wafer varied, compared to the 1 × 1 cm pieces. The epilayers can be calibrated on 2" wafers. Additionally, in this work, the i-$In_xGa_{1-x}N$ and p-GaN were grown at substrate temperatures of 400 and 500 °C, respectively. Optimally both layers should be grown at the same substrate temperature, which should improve the interface between the i-$In_xGa_{1-x}N$ and p-GaN.

- **Investigation into Ohmic Contacts Metals for p-GaN**

The highest hole concentration for Mg-doped GaN of 4.26×10^{19} cm^{-3} and resistivity of 0.5 Ω-cm presented in this work, should have an optimal ohmic metal contact. Previously, a complete study into p-GaN contact metal was limited by the ability to p-type dope GaN and sample quantity. As was presented in Chapter 4, we have the ability to repeatably grow Mg-doped GaN with hole concentrations greater than 1×10^{19} cm^{-3}, eliminating the sample limitation. The ohmic alloy can be used in the solar cell fabrication to reduce the high contact resistance evidenced in p-type TLM results in Chapter 7.

- **MME of InN and Mg-doped InN.**

Chapter 5 presented the unsuccessful results of a MME growth of InN with shutter cycles of a few seconds. Yamguchi et al. [111] used a similar technique to MME with great success with shuttering cycles greater than 2 minute. A study can be conducted where the MME cycle is increased from a few seconds to a few minutes. The longer shutter cycle, will give the excess In on the surface the ability to incorporate before the next shutter open cycle, resulting in complete coalescences of the film. Once the growth parameters of MME InN have been established, Mg can be included in a similar manner

as the Mg-doped GaN study. Additionally, MME growth of InN provides a new dimension for $In_xGa_{1-x}N$ growth, digital $In_xGa_{1-x}N$. Traditional $In_xGa_{1-x}N$ growth is completed by opening the Ga and In shutters together at a specific calibrated flux. Digital growth is similar to multiple quantum well devices where the metal shutters are opened and closed individually, resulting in numerous GaN/InN layers. Each layer is only a few angstroms thick, so the overall device is complimentary to an $In_xGa_{1-x}N$ layer. The film composition is determined by the thickness of the GaN and InN layers. For example, $In_{0.05}Ga_{0.95}N$ requires layer thicknesses of ~ 5.6 Å and $In_{0.25}Ga_{0.75}N$ requires layer thicknesses of ~ 6.7 Å. The only required calibration for digital growth is the growth rate of the individual layers. Figure 8.1 shows the screen capture of the digital device growth program.

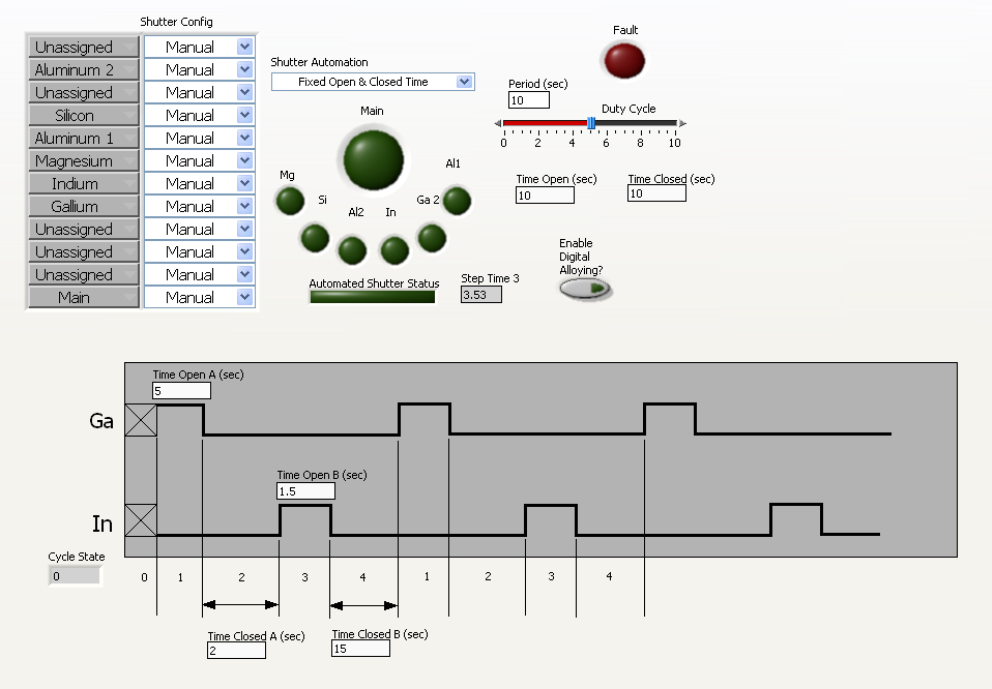

Figure 8.1– Screen capture of digital device growth program.

- **Tandem $In_xGa_{1-x}N$ solar cells**

Assuming the above future work tasks have been completed and a successful heterojunction $In_xGa_{1-x}N$ has been established, a tandem $In_xGa_{1-x}N$ solar cell can be attempted. The high hole concentration Mg-doped GaN is degenerately doped and is a requirement for the production of tunnel junctions used in tandem interconnected devices. In a tunnel junction the semiconductor material is heavily doped, such that the valence band and conduction bands to line up allowing an electron in the n-type material to tunnel without energy loss into the hole in the adjacent valence band. Therefore, current flows with minimal loss of energy across the interface creating an ohmic interconnection, as if the two cells were wired in series. The degenerately doped GaN makes tandem $In_xGa_{1-x}N$ solar cells tangible.

APPENDIX A: Basics of Solar Cells

A solar cell performs two functions: photogeneration of charge carriers in a light-absorbing material and separation of the charge carriers to a conductive contact. Each semiconductor material has a bandgap, a fundamental property of the material that is defined as the energy gap between the top of the valence band and the bottom of the conduction band. Electrons are able to move from one band to another band. It is in this region that light-generated carriers create the photovoltaic effect. Incident photons with energy equal to the bandgap of the material can create mobile electron-hole pairs (EHP) in (or that diffuse to) the depletion region, where they will be swept across the junction by an electric field and produce photocurrent. Incident photons with energy less than the bandgap pass directly through the device; therefore the semiconductor appears transparent. Finally, incident photons with energy much greater than the bandgap are absorbed, but all the excess energy above the bandgap is dissipated as heat in the semiconductor.

Charge carrier movement can occur by two modes: diffusion or drift. In diffusion, the carriers flow from regions of high carrier concentrations to regions of low carrier concentrations. Conversely, an internal electric field drives the carriers, causing drift current. This mode is the dominant current flow mode in thin film solar cells, where as diffusion is much more important in thicker solar cells. Figure A.1 shows the band diagram of a simple p-n diode under forward bias and during photogeneration. At equilibrium the Fermi level remains flat and the amount of drift and diffusion current is equal. Traditional diodes are forward biased, where voltage is applied externally. As

seen in Figure A.1(a) under forward bias, the diffusion current dominates and current flows from the p-region to the n-region.

In the photogenerated case, voltage is generated internally from the internal electric field sweeping the EHP across the junction. Figure A.1(b) shows that drift current dominates and current flows from the n-region to the p-region, creating photocurrent. Every EHP generated in the depletion region and EHP generated within a diffusion length away from the depletion region will add to the photocurrent. It should be noted that the photocurrent is in the reverse bias direction. Therefore, the net solar cell current is also in the reverse bias direction, which results in net power being produced.

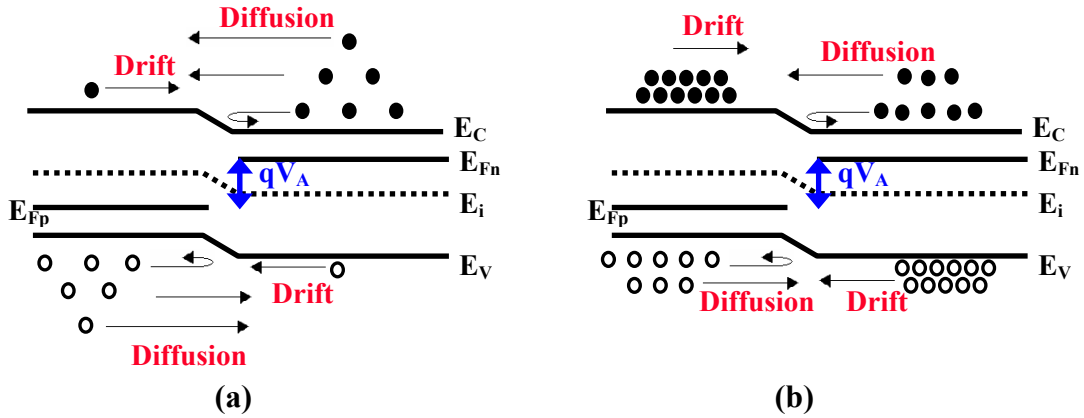

Figure A.1 – Band diagram of p-n diode in: (a) forward bias and (b) photogeneration.

As stated previously, the ability of the solar cell to create current is dominated by the generation and recombination of carriers in the device. If the incident light on the solar cell is removed, the light-generated EHP will decay back to their equilibrium values. Therefore, the photogenerated EHP are in excess of the total EHP when the device is in the dark. This process is referred to as recombination and can occur in three modes: radiative, Auger, and trap recombination [1, 119]. The different recombination rates can occur in parallel and are summed together for a total recombination rate.

In radiative recombination, an electron occupying a higher energy state than at equilibrium transitions to an empty lower-energy state. The excess energy released during this process is converted into light. Auger recombination occurs when an electron recombining with a hole imparts its excess energy to a second electron instead of emitting light. The second electron then relaxes back to the original energy by emitting phonons. Auger recombination is usually found in regions of highly doped material or in devices with excessively high current densities, such as concentration high performance solar cells. Trap recombination is related to defects in the material. Defects in the material create traps in the bandgap where an electron can relax from the conduction band to a defect level and then relax to the valence band. This process annihilates holes. Trap recombination can also occur on the surface of the material and is exacerbated by rough surfaces such commonly found during fabrication.

A solar cell is electrically modeled by a diode-equivalent circuit as shown in Figure A.2, with an optical generated current (I_L), a diode in parallel with series resistance (r_S), and shunt resistance (r_{sh}).

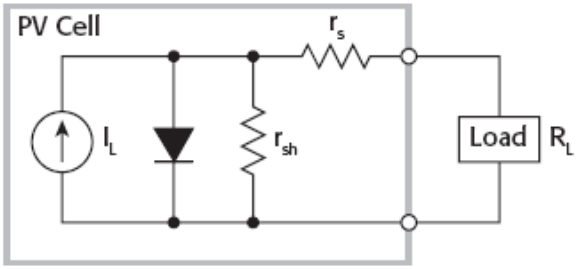

Figure A.2 – Idealized equivalent electrical circuit of a photovoltaic cell [120].

Using the ideal diode law and measuring the current across R_L

$$I = I_{SC} - I_O\{\exp\frac{qV^1}{nkT} - 1\} - \frac{V^1}{r_{sh}}. \quad (1)$$

I_{SC} is the short circuit current or the photogenerated current. The voltage across the diode is defined as

$$V^1 = V + Ir_S \text{ .} \quad (2)$$

The series resistance, r_s, includes the bulk resistance of the semiconductor, the resistance of the metal contacts, and sheet resistance. The shunt resistance, r_{sh}, is caused by lattice defects in the depletion region and leakage current around the edges of the device.

The performance of a solar cell is defined by the current-voltage characteristics in dark and illuminated conditions. The short circuit current of the device is found when the voltage drop across the junction is zero. If the series resistance is zero, then the short circuit current is equal to the photocurrent. The open circuit voltage is found when the junction current is zero and is determined by the absorption and light-generation process and how efficiently the charge carriers reach the depletion region.

The short circuit current and open circuit voltage are also affected by the bandgap. If the bandgap of the material decreases, more photons have enough energy to create additional EHP, which causes I_{SC} to increase and V_{OC} to decrease. Additionally, if the solar cell has a large series resistance and low shunt resistances, I_{SC} and V_{OC} will decrease. Therefore, the semiconductor material needs to have few defects and electrical contact with the device needs to be minimal.

The performance of the solar cell is determined by the output power. Figure A.3 shows a typical current-voltage curve of a solar cell in illuminated conditions.

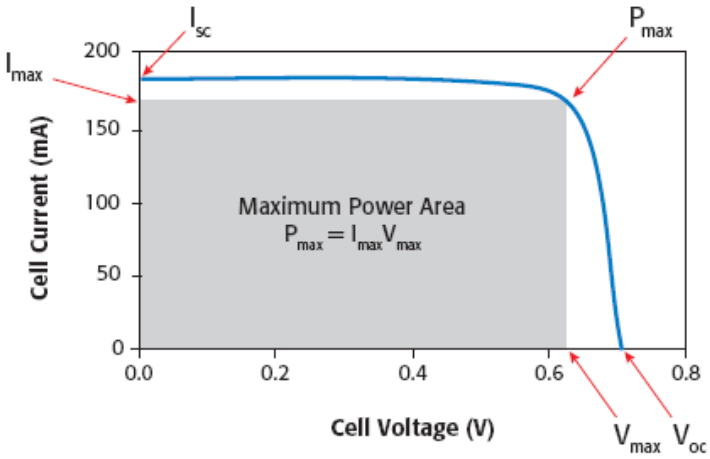

Figure A.3 – Current-voltage characteristics of a solar cell when illuminated with the short circuit current, open circuit voltage, and current-voltage that result in the maximum power output for the device [120].

I_{SC} and V_{OC} represent the upper limits of the device as measured in a laboratory setting. The maximum area under the curve, which in turn relates to the maximum power of the device, is represented by I_m and V_m. A figure of merit for solar cells is the fill factor (FF), measuring how "square" the current-voltage curve is. It is mathematically defined as

$$FF = \frac{V_m I_m}{V_{OC} I_{SC}}. \tag{3}$$

Ideally, a large FF is desirable for high-efficient solar cells. Typical values of fill factors range from 0.7 to 0.9. Large arrays of solar cells, ones found on commercial buildings, will have a FF equal to 0.5, because of losses from the series connection of the individual cells.

Along with FF, the energy-conversion efficiency (η) is another solar cell figure of merit:

$$\eta = \frac{V_M I_M}{P_{in}} = \frac{FF V_{OC} I_{SC}}{P_{in}}. \tag{4}$$

P_{in} is the total power of incident light on the solar cell. Primarily, the efficiency of a device is determined by the mobility and lifetime of the minority charge carriers and surface recombination velocities.

Figure A.4(a) shows another I-V curve of a typical solar cell with the cell under illumination and in the dark. Note that the light-generated current has been superimposed upon the normal rectifying current-voltage characteristics of a diode, resulting in a region in the fourth quadrant where electrical power can be extracted from the device.

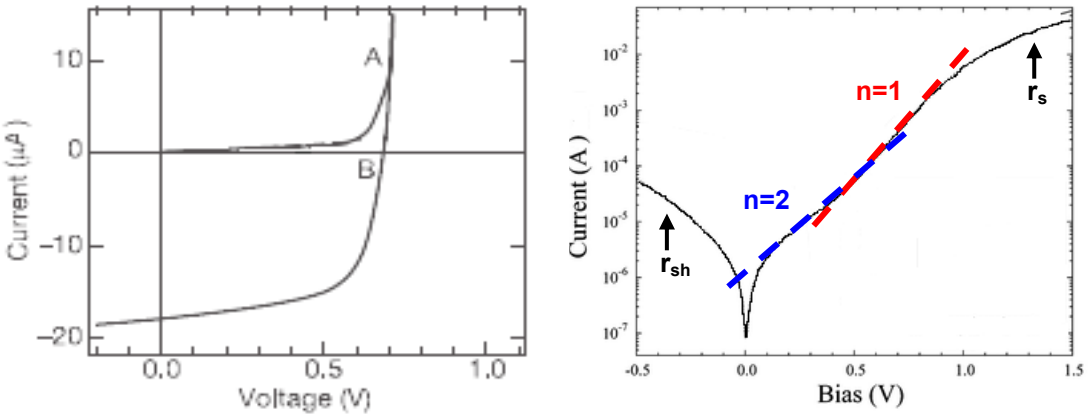

Figure A.4 – Typical current-voltage curves of a solar cell in: (a) a linear graph with dark and illuminated measurements represented as A and B, respectively [121] and (b) a semi-logarithmic of the dark measurement showing series and shunt resistance and diode ideality factor, n = 1 or 2 [122].

When the dark curve is plotted on a semi-logarithmic graph as shown in Figure A. 4(b), the series and shunt resistance of the device can be determined. Additionally, the slope of the graph can determine the diode ideality factor used in Equation (1), where $1 > n > 2$. An ideality factor greater than 1 reduces the fill factor of the solar cell and in heterojunction solar cells, an ideality factor greater than 2, signifies that there is recombination of carriers in the depletion region.

Again, series resistance is associated with bulk material resistance and the resistance of metal contacts. The shunt resistance can be attributed to lattice defects in the depletion

region or leakage currents around the edge of the cells. All of the above discussions relate the performance of the solar cell to the material properties of the semiconductor.

An added technique to increase the output of the solar cell is the use of an anti-reflection (AR) coating, where the goal is to increase the amount of light coupled into the device. The coating should have excellent surface passivation qualities, is typically deposited using thermal evaporators or plasma-enhanced chemical vapor deposition (PECVD), and is several hundred nanometers thick. The AR coating should also have a refractive index that corresponds to the material system while maintaining transparency.

APPENDIX B: Sample Preparation

B.1 Germanium Substrates

(111)-oriented epi-ready Ga-doped Ge substrates were used for initial InN growths. The samples were chemically cleaned to remove all organics, maintaining the high purity growth environment. Degreasing the samples included five minutes etch of agitation in an ultrasonic bath with trichloroethylene (TCE), acetone, and methanol, followed by de-ionized (DI) water rinse and nitrogen gun blow dried. The samples were then mounted on a Veeco uniblock sample holder with custom molybdenum (Mo) spring plates and retaining rings. Finally, the samples were loaded into the introductory chamber of the MBE system and outgassed for one hour at 300 °C.

B.2 Al_2O_3 substrates

B.2.1 Cleaning

c-plane Al_2O_3 samples were initially cleaned following the procedure outlined for Germanium substrates. Work conducted by Burnham [99] found a more effective method of cleaning with a hot piranha etch. Hot piranha etch consists of a 4:1 mixture of H_2SO_4:H_2O_2 heated to approximately 90 °C. This method was used for all Al_2O_3 samples and HVPE GaN templates, followed by a rigorous DI water rinse and nitrogen gun blow dried. Additionally, the cleaned samples were mounted on a Veeco uniblock sample holder with custom Mo spring plates and pyrolytic boron nitride (PBN) retaining rings and loaded into the introductory chamber of the MBE system to be outgassed for one hour at 300 °C.

B.2.2 Backside Metallization

The Al_2O_3 substrates are transparent and require backside metallization. Using a Kurt J. Lesker PVD RF Sputterer, ~ 2 μm tantalum (Ta) metal was deposited on the rough side of the Al_2O_3. The deposition conditions include: Ar gas at 6 mtorr, RF power = 300 W, and base pressure of ~ 4×10^{-6} torr. This procedure was also used for HVPE GaN templates.

B.2.3 Nitridation and AlN Buffer

Al_2O_3 substrates have a significant lattice mismatch between GaN and $In_xGa_{1-x}N$. Nitridation of the Al_2O_3 substrate reduces this lattice mismatch. The nitridation process forms an AlN layer on the Al_2O_3 substrate by assisting the O-to-N anion exchange, converting the substrate surface from Al_2O to AlN as described by Namkoong [123]. The nitridation process was conducted for 30 minutes at a substrate temperature of 300 °C, RF power = 350 W, nitrogen flow rate of 1.3 sccm, and base pressure maintained at 1.2×10^{-5} torr.

Following the nitridation, an AlN buffer layer was grown to ensure Al polar material. The AlN buffer was grown using a combined technique developed by Namkoong and Burnham [94, 123], where the Al shutter is modulated with a fixed duty cycle and at a substrate temperature of 700 °C. The Al flux was 4.9×10^{-7} torr, RF power = 350 W, nitrogen flow rate of 1.3 sccm, leading to a growth rate of ~ 700 nm/hr, with a target film thickness of 120 nm.

APPENDIX C: Pole-Figure Measurements

Chapter 3 introduced pole-figure measurements with six-fold symmetric peaks that were deformed in ψ when compared with the expected zinc-blende ψ position. Additional ω-2θ scan were done to determine the reflection associated with the deformed ψ. The following outlines the procedure to determine if the shifted ψ is related to zinc-blende or wurtzite materials for wurtzite III-N films.

The scans in Figure 3.10 and Figure 7.3 used a ¼ slit on the incident optics and an open rocking curve for the detector optics.

1. The {11-29} Al_2O_3 Position

1.1. Optimize the system in the normal manner for the {0006} Al_2O_3 peak and set the sample offsets.

1.2. Move to the {11-29} Al_2O_3 position.

1.3. Set ψ ≅ 32 °.

1.4. Run a 360 ° Φ-scan.

1.4.1. Move to the highest intensity peak.

1.4.2. The scan should have six distinct peaks associated with the Al_2O_3 substrate.

1.5. Run a 6 ° ψ-scan.

1.5.1. Move to the highest intensity.

1.6. Run a 12+ ° ω-2θ scan.

1.6.1. Peaks at ω ≅ 32 ° are related to wurtzite {10-13} reflections for III-N films.

1.6.2. Peaks at ω ≅ 35 ° are related to zinc-blende {311} reflections for III-N films.

1.6.3. Verify the reflection and 2θ position with the material data cards provided in PCPDFWIN.

APPENDIX D: Solar Cell Fabrication Process Flow

The following procedure was used for fabricating solar cell devices using five masks provided by HTA Photomask Inc. Samples were degreased with trichloroethylene (TCE), actone, methanol, rinsed with de-ionized (DI) water, and dried with a nitrogen spray gun before any lithography or deposition step.

1. Mesa: Cell Mesa mask

1.1. Lithography

1.1.1. Clariant AZ 5214 photoresist (PR) was spun on the sample, 500 rpm for 5 seconds to spread the PR, followed by 3000 rpm for 30 seconds resulting in PR thickness of ~1.6 μm.

1.2. Sample is soft baked in a 95 °C oven on a hot block for 90 seconds.

1.3. Alignment and exposure

1.3.1. Positive process

1.3.1.1. Exposure energy = 120 mJ/cm^2. Measure lamp intensity with 365 nm detector to determine exposure time.

1.4. Develop –

1.4.1. Shipley 354 developer for 30 seconds with slight agitation.

1.4.2. DI water rinse. PR integrity was verified optically and with an alpha step profilometer.

1.5. Hard bake the PR before any Inductively Coupled Plasma (ICP) etching steps – in 95 °C oven on a hot block for 30 minutes.

1.6. Mount sample with cool grease on 4" Si carrier wafer.

1.7. Inductively Coupled Plasma (ICP) etching

1.7.1. Run CleanO2 recipe for one hour before using the system.

1.7.1.1. Ar = 5 sccm, O_2 = 60 sccm, 20 mtorr, RF1 = 100 W, RF2 = 800 W for 10 minutes

1.7.1.2. Ar = 5 sccm, O_2 = 60 sccm, RF1 = 20 W, RF2 = 800 W for 50 minutes

1.7.2. GaN etching:

1.7.2.1. Cl_2 = 32 sccm, BCl_3 = 8 sccm, Ar = 5 sccm, 5 mtorr, RF1 = 70 W, RF2 = 500W, etch rate is ~ 350 nm/min.

1.8. Acetone clean samples and verify thickness of the mesa with alpha step profilometer.

2. Thick SiO_2 deposition:

2.1. Run clean recipe on Plasma Enhanced Chemical Vapor Deposition (PECVD).

2.2. Deposit ~1 μm of SiO_2

2.2.1. 300 °C, SiH_4 = 400 sccm, N_2O = 900 sccm, 900 mtorr, RF = 25 W, deposition rate is ~ 50 nm/min.

3. Base contact etching: Recessed Contact mask

3.1. Lithography –

3.1.1. Clariant AZ 5214 PR was spun on the sample, 500 rpm for 5 seconds to spread the PR, followed by 3000 rpm for 30 seconds resulting in PR thickness of ~1.6 μm.

3.2. Sample is soft baked in a 95 °C oven on a hot block for 90 seconds.

3.3. Alignment and exposure

3.3.1. Negative process –

3.3.1.1. Exposure energy = 80 mJ/cm^2. Measure lamp intensity with 365 nm detector to determine exposure time.

3.4. Sample is soft baked in a 120 °C oven on a hot block for 90 seconds.

3.5. Flood expose samples –

3.5.1. Exposure energy = 200 mJ/cm^2. Measure lamp intensity with 365 nm detector to determine exposure time.

3.6. Develop – Shipley 354 developer for 30 seconds with slight agitation. DI water rinse. PR integrity was verified optically and with an alpha step profilometer.

3.7. Mount sample with cool grease on 4" Si carrier wafer.

3.8. ICP etching

3.8.1. *Follow procedure outlined in 1.7.1*

3.8.2. SiO_2 etching:

3.8.2.1. Ar = 15 sccm, O_2 = 3.0 sccm, CF_4 = 10.0 sccm, C_4F_6 = 10.0 sccm, RF1 = 400 W, RF2 = 100 W, etch rate ~ 50 nm/min.

3.9. Acetone clean samples and verify thickness of the SiO_2 trench with alpha step profilometer.

3.10. ICP etching to etch $In_xGa_{1-x}N$ trenches

3.10.1. *Follow procedure outlined in 1.7.1*

3.10.1.1. It is imperative to run the CleanO2 recipe between etching SiO_2 and GaN. The SiO_2 etch chemistry and GaN etch chemistry will interact and leave particles that are virtually impossible to remove.

3.10.2. *Follow procedure outlined in 1.7.2*

3.11. Verify thickness of the trench with alpha step profilometer.

3.12. BOE etch SiO_2

3.12.1. Etch rate ~ 600 nm/min

3.13. Alpha step profilometer to verify the depth of the $In_xGa_{1-x}N$ trenches.

4. Thin SiO_2 deposition:

4.1. Repeat step 2.1

4.2. Deposit ~200nm of SiO_2

5. Etch thin SiO_2:

5.1. Repeat steps 1.7.1 and 3.8.2.

5.2. Alpha step profilometer to verify thickness of the trench.

6. Base metal: Recessed Trench mask

6.1. Repeat steps 3.1 – 3.6

6.2. E-beam deposition of Si/Ti/Al/Ti/Au with thicknesses of 10/250/1000/450/2000 Å at a base pressure of ~2×10^{-6} torr.

6.3. Acetone soak for metal liftoff.

7. Spreading metal: Top Spreading mask

7.1. Repeat steps 3.1 – 3.6

7.2. E-beam deposition of Ni/Au with thicknesses of 50/50 Å at a base pressure of ~2×10^{-6} torr.

7.3. Acetone soak for metal liftoff.

8. Emitter metal: Top Contact mask

8.1. Repeat steps 3.1 – 3.6

8.2. E-beam deposition of Ni/Au with thicknesses of 250/2500 Å at a base pressure of ~2×10^{-6} torr.

8.3. Acetone soak for metal liftoff.

8.4. Anneal samples in mini annealer for 3 minutes at 550 °C with O_2.

Figure D. 1 is a schematic of the fabrication process. Figure D. 1(a) is the initial device material, (b) is the mesa structure as described in step 1. (c) shows the deposition of the thick oxide described in step 2. Step 3 is depicted in (d) – (f) with (d) showing the plasma etching of the thick oxide, (e) shows the plasma etching of the $In_xGa_{1-x}N$ film, and (f) shows the removal of the thick oxide with BOE. (g) shows the deposition of the thin oxide described in step 4. Step 5 is depicted in (h), showing the plasma etching of the thin oxide. Steps 6 – 8 are depicted in (i) – (k), respectively, showing the deposition of the contact metal. Figure D. 1 (l) is the final device and (m) is an image of a fabricated sample. The images are not to scale, but have been exaggerated for clarity.

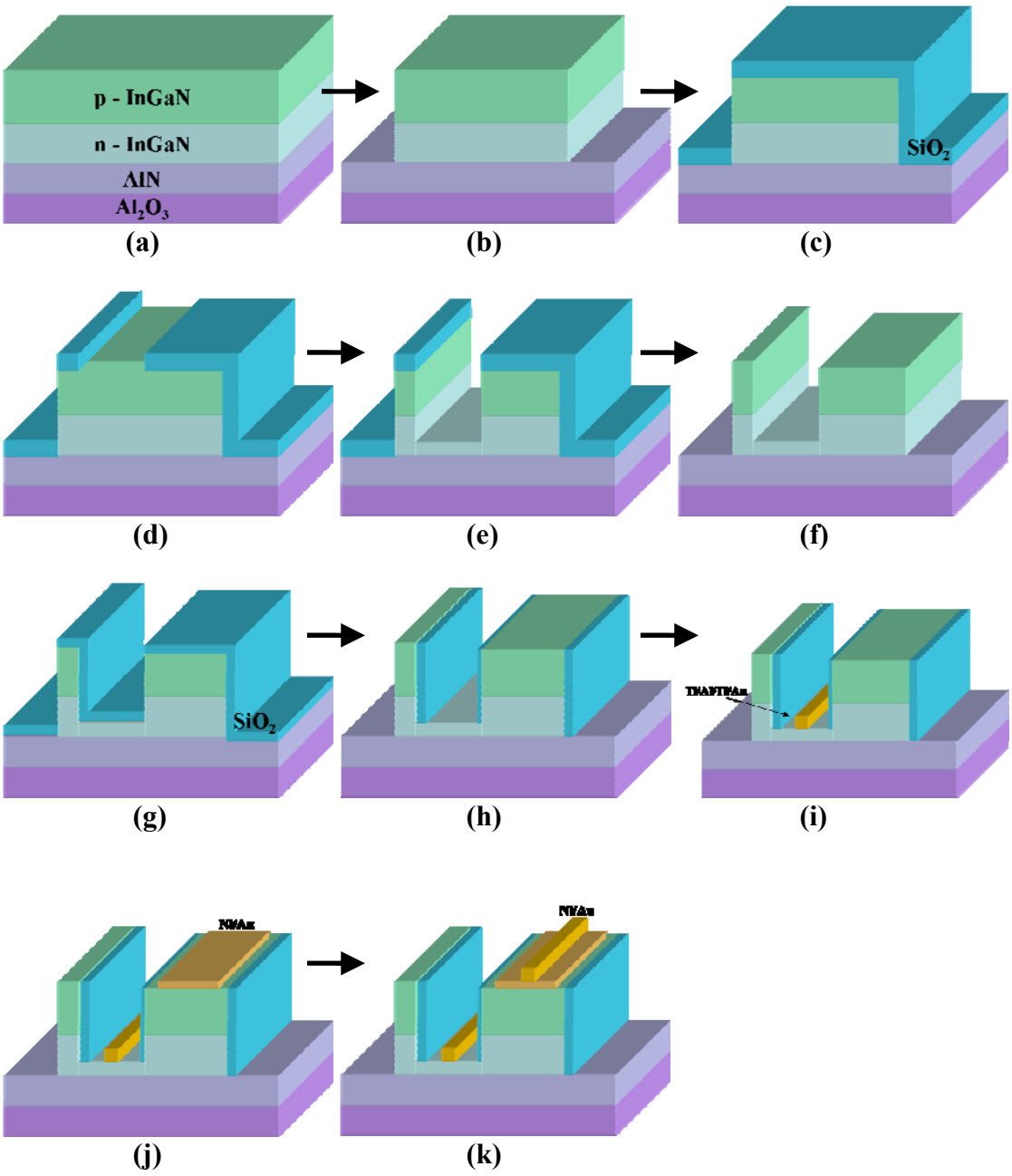
p - InGaN
n - InGaN
AlN
Al_2O_3
SiO_2
(a)
(b)
(c)
(d)
(e)
(f)
SiO_2
(g)
(h)
(i)
(j)
(k)

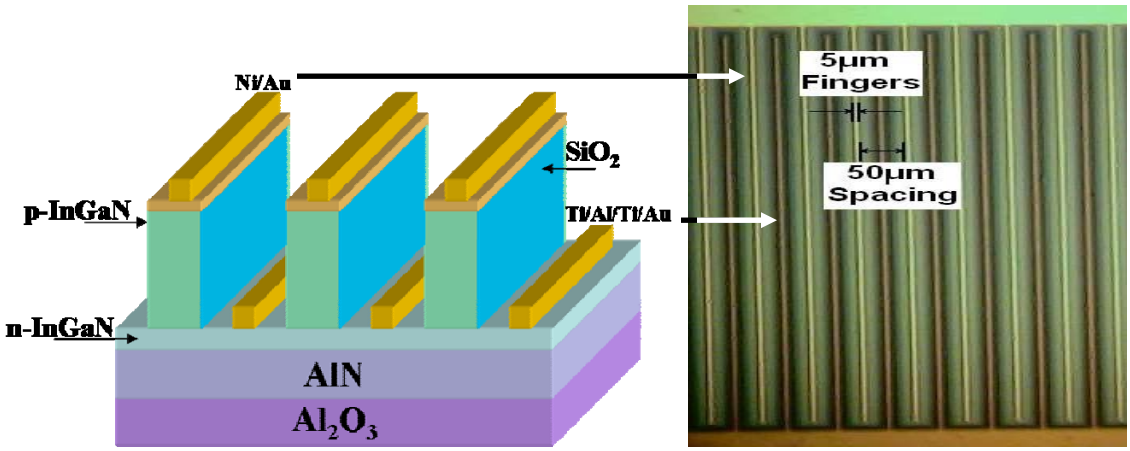

(l) (m)

Figure D. 1 – Schematic of fabrication process: (a) initial material, (b) mesa structure, (c) thick SiO_2 deposition, (d) Plasma etching of thick SiO_2, (e) $In_xGa_{1-x}N$ etching, (f) BOE etching of SiO_2, (g) thin SiO_2 deposition, (h) Plasma etching of thin SiO_2, (i) n-type metal deposition, (j) spreading metal deposition, (k) p-type metal deposition, (l) final structure, and (m) image of fabricated device.

REFERENCES

[1] H.J. Möller, Semiconductors for Solar Cell, Artch House, Inc. Norwood, MA (1993).

[2] J. Nelson, *The Physics of Solar Cell*, Imperial College Press, (2003).

[3] R.R. King, D.C. Law, K.M Edmondson, C.M. Fetzer, G.S. Kinsey, H. Yoon, R.A. Sherif, and N.H. Karam, "40% Efficient Metamorphic GaInP/GaInAs/Ge Multijunction Solar Cells," Appl. Phys. Lett., 90 (2007) 183516.

[4] J.F. Geisz, D.J. Friedman, J.S. Ward, A. Duda, W.J. Olavarria, T.E. Moriarty, J.T. Kiehl, M.J. Romero, A.G. Norman, and K.M. Jones, "40.8% Efficient Inverted Triple-Junction Solar Cell with Two Independently Metamorphic Junctions," Appl. Phys. Lett., 93 (2008) 123505.

[5] National Renewable Energy Laboratory, downloaded from http://en.wikipedia.org/wiki/Image:PVeff%28rev110707%29d.jpg on January 15, 2008.

[6] *Terrestrial Photovoltaic Measurement Procedures*, ERDA/NASA Report 1022-77/16, 1977.

[7] American Society for Testing and Materials Terrestrial Reference Spectra, downloaded from http://www.planet.laptopy-radom.info/info-Solar_radiation on January 15, 2008.

[8] Photovoltaics CDROM, downloaded from http://pvcdrom.pveducation.org on September 2, 2008.

[9] D.J. Friedman, S.R. Kurtz, and J.F. Geisz, "Analysis of the GaInP/GaAs/1-eV/Ge Cell and Related Structures for Terrestrial Concentrator Applications," Proceedings of the 29th Photovoltaic Specialists Conference, New Orleans, Louisiana (IEEE, New York, 2002) 856.

[10] Q.Z. Liu and S.S. Lau, "A Review of the Metal-GaN Contact Technology," Solid State Electron. 42 (1998) 677.

[11] M.S. Shur, "GaN Based Transistors for High Power Applications," Solid State Electron., 42 (1998) 2131.

[12] J.C. Zopler, "A Review of Junction Field Effect Transistors for High-Temperature and High-Power Electronics," Solid State Electron., 42 (1998) 2153.

[13] K. Osamura, K. Nakajima, Y. Murakami, P.H. Shingu, and A. Ohtsuki, "Fundamental Absorption Edge in GaN, InN and Their Alloys," Solid State Comm., 11 (1972) 617.

[14] K.L. Westra, R.P.W. Lawson, and M.J. Brett, "The Effects on Oxygen Contamination on the Properties of Reactively Sputtered Indium Nitride Films," J. Vac. Sci. Technol. A 6 (1988) 1730.

[15] K. Ikuta, Y. Inoue, and O. Takai, "Optical and Electrical Properties of InN Thin Films Grown on ZnO/α-Al_2O_3 by RF Reactive Magnetron Sputtering," Thin Solid Films 344 (1998) 49.

[16] V.Yu. Davydov, A.A. Klochikhin, R.P. Seisyan, V.V. Emtsev, S.V. Ivanov, F. Bechstedt, J. Furthmuller, H. Harima, A.V. Mudryi, J. Aderhold, O. Semchinova, and J. Graul, "Absorption and Emission of Hexagonal InN. Evidence of Narrow Fundamental Band Gap," Phys. Stat. Sol. B, 229 (2002) R1.

[17] J. Wu, W. Walukiewicz, K.M. Yu, J.W. Ager III, E.E. Haller, H. Lu, W.J. Schaff, Y. Saito, and Y. Nanishi, "Unusual Properties of the Fundamental Band Gap of InN," Appl. Phys. Lett., 80 (2002) 3967.

[18] S. Strite and H. Morkov, "GaN, AlN, and InN: A Review," J. Vac. Sci. Technol. B 10 (1992) 1237.

[19] T.L. Tansley and C.P. Foley, "Optical Band Gap of Indium Nitride," J. Appl. Phys. 59 (1986) 3241.

[20] V.Yu. Davydov, A.A. Klochikhin, V.V. Emtsev, D.A. Kurdyukov, S.V. Ivanov, V.A. Vekshin, F. Bechstedt, J. Furthmüller, J. Aderhold, J. Graul, A.V. Mudryi, H. Harima, A. Hashimoto, A. Yamamoto, and E.E. Haller, "Band Gap of Hexagonal InN and InGaN Alloys," Phys. Stat. Sol. B 234 (2002) 787.

[21] J. Wu, W. Walenkiewicz, W. Shan, K.M. Yu, J.W. Ager III, E.E. Haller, H. Lu, and W.J. Schaff, "Effects of the Narrow Band Gap on the Properties of InN," Phys. Rev. B 66 (2002) 201403.

[22] A.G. Bhuiyan, A. Hashimoto, and A. Yamamoto, "Indium Nitride: A Review on Growth, Characterization, and Properties," J. Appl. Phys., 94 (2003) 2779.

[23] A. Yamamoto, T. Tanaka, K. Koide, and A. Hashimoto, "Improved Electrical Properties for Metalorganic Vapour phase Epitaxial InN Films," Phys. Stat. Sol. A 194 (2002) 510.

[24] Ulm University downloaded from http://www-opto.e-technik.uni-ulm.de/lehre/cs/index.html on January 15, 2008.

[25] J. Wu, W. Walukiewicz, K.M. Yu, J.W. Ager III, E.E. Haller, H.Lu, and W.J. Schaff, "Small Band Gap Bowing in $In_{1-x}G_xN$ Alloy," Appl. Phys. Lett. 80 (2002) 4741.

[26] I. Vurgaftman and J.R. Meyer, "Band Parameters for Nitrogen-Containing Semiconductor," Appl. Phys. Rev. 94 (2003) 3675.

[27] V.A. Elyukhin and S.A. Nikishin, "Internal Strain Energy of $A^3{}_xB^3{}_{1-x}N$ Ternary Solid Solutions of Cubic Modification," Semicond. Sci. Technol. 11 (1996) 917.

[28] I. Ho and G.B. Stringfellow, "Solid Phase Immiscibility in GaInN," Appl. Phys. Lett. 69 (1996) 2701

[29] I. Ho and G.B. Stringfellow, Mater. Res. Soc. Symp. Proc. 449 (1997) 871.

[30] A. Tabata, L.K. Teles, L.M.R. Scolfaro, J.R. Leite, A. Kharchenko, T. Frey, D.J. As, D. Schikora, K, Lischka, J. Furthmuller, and F. Bechstedt, "Phase Separation Suppression in InGaN Epitaxial Layers due to Biaxial Strain, " Appl. Phys. Lett. 80 (2002) 769.

[31] A. Zunger, *Handbook of Crystal Growth*, edited by D.T.J. Hurle, Elsevier, New York, 1994, Vol. 3, pg. 998.

[32] S.Y. Karpov, "Suppression of Phase Separation in InGaN due to Elastic Strain," MRS Internet J. Nitride Semicon. Res. 3 (1998) 16.

[33] F. Bernardini and V. Fiorentini, "Spontaneous versus Piezoelectric Polarization in III-V Nitrides: Conceptual Aspects and Practical Consequences," Phys. Stat. Sol. B 216 (1999) 391.

[34] F.Bernardini and V. Fiorentini, "Nonlinear Macroscopic Polarization in III-V Nitride Alloys," Phys. Rev. B, 64 (2001) 085207-1.

[35] O. Ambacher, J. Smart, J.R. Shealy, N.G. Weimann, K. Chu, M. Murphy, W.J. Schaff, L.F. Eastman, R. Dimitrov, L. Wittmer, M. Stutzmann, W. Rieger, and J. Hilsenbeck, "Two-dimensional Electron Gases Induced by Spontaneous and Piezoelectric Polarization Charges in N- and Ga-face AlGaN/GaN Heterostructures," J. Appl. Phys. 85 (1999) 3222.

[36] T.D. Veal, P.D.C. King, P.H. Jefferson, L.F.J. Piper, C.F. McConville, H. Lu, W.J. Schaff, P.A. Anderson, S.M. Durbin, D. Muto, H. Naoi, and Y. Nanishi, "In

Adlayers on c-place InN Surfaces: A Polarity-Dependent Study by X-ray Photoemission Spectroscopy," Phys. Rev. 76 (2007) 075313.

[37] V. Lebedev et al., "Coalescence Aspects of III-Nitride Epitaxy," J. Appl. Phys., 101 (2007) 054906.

[38] C.S. Gallinat, G. Koblmuller, J.S. Brown, S. Bernardis, J.S. Speck, G.D. Chern, E.D. Readinger, H. Shen, and M. Wraback, "In-polar InN Grown by Plasma-Assisted Molecular Beam Epitaxy," Appl. Phys. Lett., 89 (2006) 032109.

[39] J.W. Kim, Y.H. Hwang, J.H. Cho, and H.K. Kim, "Critical Thickness of AlN Thin Films Grown on Al_2O_3 (0001)," Jpn. J. Appl. Phys. 40 (2001) 4677.

[40] C. Kim, I.K. Robinson, J. Myoung, K. Shim, M.C. Yoo, and K. Kim, "Critical Thickness of GaN Thin Films on Sapphire (0001)," Appl. Phys. Lett., 69 (1996) 2358.

[41] M.J. Reed, N.A. El-Masry, C.A. Parker, J.C. Roberts, and S.M. Bedair, "Critical Layer Thickness Determination of GaN/InGaN/GaN Double Heterostructures," Appl. Phys. Lett. 77 (2000) 4121.

[42] A.Y. Cho, M.B. Panish, and I. Hayashi, "Molecular Beam Epitaxy of GaAs, $Al_xGa_{1-x}As$ and GaP," 3rd Int. Symp. on Gallium Arsenide and Related Compounds, The Institute of Physics, Conference Series, 9 (1970) 18.

[43] J.E. Davey and T. Pankey, "Epitaxial GaAs Films Deposited by Vacuum Evaporation," J. Appl. Phys., 39 (1968) 1941.

[44] H. Shelton and A.Y. Cho, "Evaporative Lifetimes of Copper, Chromium, Beryllium, Nickel, Iron, and Titanium on Tungsten and Oxygenated Tungsten," J. Appl. Phys, 37 (1966) 3544.

[45] J.R. Arthur Jr, "Interaction of Ga and As_2 Molecular Beams with GaAs Surfaces," J. Appl. Phys., 39 (1968) 4032.

[46] F. Rinaldi, "Basics of Molecular Beam Epitaxy (MBE)," downloaded from http://www-opto.e-technik.uni-ulm.de/forschung/jahresbericht/2002/ar2002_fr.pdf on January 15, 2008.

[47] S. Burnham, G. Namkoong, and W.A. Doolittle, "Closed-loop MBE Growth of Droplet-Free GaN with Very Metal Rich Conditions Using Metal Modulated Epitaxy with Mg and In," Phys. Stat. Sol. C, 6 (2008) 1855.

[48] H. Lu, W.J. Schaff, J. Hwang, H. Wu, G. Koley, and L.F. Eastman, "Effect of an AlN Buffer Layer on the Epitaxial Growth of InN by Molecular Beam Epitaxy," Appl. Phys. Lett. 79 (2001) 1489.

[49] A. Yamamoto, M. Tsujino, M. Ohkubo, and A. Hashimoto, "Nitridation Effects of Substrate Surface on the Metalorganic Chemical Vapor Deposition Growth of InN on Si and α-Al_2O_3 Substrates," J. Crystal Growth 137 (1994) 415.

[50] R.F. Pierret, *Semiconductor Device Fundamentals*, Addison-Wesley Publishing Company, Inc., (1996).

[51] L. Chernyak, A. Osinsky, G. Nootz, A. Schulte, J. Jasinski, M. Benamara, Z. Liliental-Weber, D.C. Look, and R.J. Molnar, "Electron Beam and Optical Depth Profiling of Quasibulk GaN," Appl. Phys. Lett. 77 (2001) 2695.

[52] H. He, T. Sekine, T. Kobayashi, and K. Kimoto, "Phase Transformation of Germanium Nitride (Ge_3N_4) Under Shock Wave Compression," J. Appl. Phys. 90 (2001) 4403.

[53] I. Chambouleyron and A.R. Zanatta, "Nitrogen in Germanium," J. Appl. Phys. 84 (1998) 1.

[54] R.W. Olesinski, N. Kanani, and G.J. Abbaschian, "Germanium-Indium," *Binary Alloy Phase Diagrams*, edited by T.B. Massalski, American Society for Metals, Ohio, Vol. 2, pg. 1217.

[55] E. Trybus, G. Namkoong, W. Henderson, W.A. Doolittle, R. Liu, J. Mei, F. Ponce, M. Cheung, F. Chen, M. Furis, and A. Cartwright, "Growth of InN on Ge Substrate by Molecular Beam Epitaxy," J. Crystal Growth 279 (2005) 311.

[56] V.V. Mamutin, V.A. Vekshin, V.Yu. Davydov, V.V. Ratnikov, T.V. Shubina, S.V. Ivanov, P.S. Kopev, M. Karlsteen, U. Söderwall, and M. Willander, "MBE Growth of Hexagonal InN Films on Sapphire with Different Initial Growth Stages," Phys. Stat. Sol. A 176 (1999) 247.

[57] T.D. Veal, I. Mahboob, F.J. Piper, C.F. McConville, h. Lu, and W.J. Schaff, "Indium Nitride: Evidence of Electron Accumulation," J. Vac. Sci. Technol. B 4 (2004) 2175.

[58] I. Mahboob, T.D. Veal, C.F. McConville, H. Lu, and W.J. Schaff, "Intrinsic Electron Accumulation at Clean InN Surfaces," Phys. Rev. Lett. 92 (2004) 036804.

[59] K.A. Rickert, A.B. Ellis, F.J. Himpsel, H.Lu, W.J. Schaff, J.M. Redwings, F. Dwikusuma, and T.F. Kuech, "X-ray Photoemission Spectroscopic Investigation

of Surface Treatments, Metal Deposition, and Electron Accumulation on InN," Appl. Phys. Lett. 82 (2003) 3254.

[60] T. Yodo, Y. Kitayama, K. Miyaki, H. Yona, Y. Harada, K.E. Prince, and K.S.A. Butcher, "Visible Emission near 1.9 – 2.2 eV for Hexagonal InN Films Grown by Electron Cyclotron Resonance Plasma-Assisted Molecular-Beam Epitaxy," J. Crystal Growth 269 (2004) 145.

[61] M. Yoshimoto, H. Yamamoto, W. Huang, H. Harima, J. Saraie, A. Chayahara, and Y. Horino, "Widening of Optical Bandgap of Polycrystalline InN with a Few Percent Incorporation of Oxygen," Appl. Phys. Lett. 83 (2003) 3480.

[62] E. Kurimoto, M. Hangyo, H. Harima, M. Yashimoto, T. Yamaguchi, T. Araki, Y. Nanishi, and K. Kisoda, "Spectroscopic Observation of Oxidation Process in InN," Appl. Phys. Lett. 84 (2004) 212.

[63] N. Kristianpoller, A. Rehavi, A. Shmilevich, D. Weiss, and R. Chen, "Radiation Effects in Pure and Doped Al_2O_3 Crystals," Nucl. Instrum. Methods Phys. Res. B 141 (1998) 343.

[64] I. Hamberg and C.G. Granqvist, "Evaporated Sn-doped In_2O_3 Films: Basic Optical Properties and Applications to Energy-Efficient Windows," J. Appl. Phys. 60 (1986) R123.

[65] E. Trybus, G. Namkoong, W. Henderson, S. Burnham, W.A. Doolittle, M. Cheung, and A. Cartwright, "InN: A Material with Photovoltaic Promise and Challenges," J. Cryst. Growth 279 (2005) 311.

[66] O. Jani, C. Honsberg, Y. Huang, J.O. Song, I. Ferguson, G. Namkoong, E. Trybus, W.A. Doolittle, and S. Kurtz, "Design, Growth, Fabrication and Characterization of High-Band Gap InGaN/GaN Solar Cell," Proceedings IEEE 4th World Conference on Photovoltaic Energy Conversion, 1 (2006) 20.

[67] Y. Nanishi, Y. Saito, and T. Yamaguchi, "RF-Molecular Beam Epitaxy Growth and Properties of InN and Related Alloys," Jpn. J. Appl. Phys. 42 5A (2003) 2550.

[68] T.L. Tansley and R.J. Egan, "Optical and Electronic Properties of the Nitrides of Indium, Gallium, and Aluminum and the Influence of Native Defects," Wide Band Gap Semi. Symp. (1992) 395.

[69] H. Lu, W.J. Schaff, L.F. Eastman, and C.E. Stutz, "Surface Charge Accumulation of InN Films Grown by Molecular-Beam Epitaxy," Appl. Phys. Lett., 82 (2003) 1736.

[70] R.E. Jones, K.M. Yu, S.X. Li, W. Walukiewicz, J.W. Ager, E.E. Haller, H.Lu, and W.J. Schaff, "Evidence for p-type Doping of InN," Phys. Rev. Lett. 96 (2006) 125505.

[71] P.D.C. King, T.D. Veal, H. Lu, P.H. Jefferson, S.A. Hatfield, W.J. Schaff, and C.F. McConville, "Surface Electronic Properties of n- and p-type InGaN Alloys," Phys. Stat. Sol. B 245 (2008) 881.

[72] P.D.C. King, T.D. Veal, P.H. Jefferson, C.F. McConville, H. Lu, and W.J. Schaff, "Variation of Band Bending at the Surface of Mg-doped InGaN: Evidence of p-type Conductivity Across the Composition Range," Phys. Rev. B 75 (2007) 115312.

[73] K. Kumakura, T. Makimoto, and N. Kobayashi, "Efficient Hole Generation Above 10^{19} cm^{-3} in Mg-doped InGaN/GaN Superlattices at Room Temperature," Jpn. J. Appl. Phys., 39 (2000) L195.

[74] C.A. Chang, T.Y. Tang, P.H. Chang, N.C. Chen, and C.T. Liang, "Magnesium Doping of In-rich InGaN," Jpn. J. Appl. Phys., 46 (2007) 2840.

[75] G. Namkoong, W.A. Doolittle, A.S. Brown, M. Losurdo, P. Capezzuto, and G. Bruno, "Role of Sapphire Nitridation Temperature on GaN Growth by Plasma Assisted Molecular Beam Epitaxy: Part I. Impact of the Nitridation Chemistry on Material Characteristics," J. Appl. Phys., 91 (2002) 2499.

[76] M. Losurdo, P. Capezzuto, G. Bruno, G. Namkoong, W.A. Doolittle, and A.S. Brown, "Role of Sapphire Nitridation Temperature on GaN Growth by Plasma Assisted Molecular Beam Epitaxy: Part II. Interplay Between Chemistry and Structure of Layers," J. Appl. Phys., 91 (2002) 2508.

[78] M.E. Lin, G. Xue, G.L. Zhou, J.E. Greene, and H. Morkoc, "p-type Zinc-blende GaN on GaN Substrates," Appl. Phys. Lett. 63 (1993) 932.

[79] T. Araki, T. Minami, and Y. Nanishi, "Microstructures of Cubic and Hexagonal GaN Grown on (0001) Sapphire by ECR-MBE with Various Electrical Biases," Phys. Stat. Sol. A. 176 (1999) 487.

[80] A. Munkholm, C. Thompson, C.M. Foster, J.A. Eastman, O. Auciello, G.B. Stephenson, P. Fini, S.P. Den Baars, and J.S. Speck, "Determination of the Cubic to Hexagonal Fraction in GaN Nucleation Layers Using Grazing Incidence X-ray Scattering," Appl. Phys. Lett. 72 (1998) 2972.

[81] T. Kitamura, X.Q. Shen, M. Sugiyama, H. Nakanishi, M. Shimizu, and H. Okumura, "Generation of Cubic Phase in Molecular-Beam-Epitaxy-Grown Hexagonal InGaN Epilayers on InN," Jpn. J. Appl. Phys. 45 (2006) 57.

[82] E. Sarigiannidou, E. Monroy, M. Hermann, T. Andreev, P. Holliger, S. Monnoye, H. Mank, B. Daudin, and M. Eickhoff, "Phase Transition by Mg Doping of N-Face Polarity GaN," Phys. Stat. Sol. C. 2, No. 7 (2005) 2217.

[83] S.D. Burnham, G. Namkoong, D.C. Look, B. Clafin, and W.A. Doolittle, "Reproducible Increased Mg Incorporation and Large Hole Concentration in GaN Using Metal Modulated Epitaxy," J. Appl. Phys. 104 (2008) 024902.

[84] A.V. Kuznetsov, E.V. Rakova, S.S. Lee, and P.J. Chong, "Influence of Moisture and Oxygen on the Formation of Cubic Phase GaN in Halide Vapor Phase Epitaxial Growth," J. Cryst. Growth 167 (1996) 458.

[85] T.M. Schmidt, R.H. Miwa, W. Orellana, and H. Chacham, "Stacking Fault Effects in Mg-doped GaN," Phys. Rev. B 65 (2002) 033205, and reference therein.

[86] Z. Littiental-Weber, M. Benamara, W. Swider, J. Washburn, I. Grzegory, S. Porowski, D.J.H. Lambert, C.J. Eiting, and R.D. Dupuis, "Mg-doped GaN: Similar Defects in Bulk Crystals and Layers Grown on Al2O3 by Metal-Organic Chemical-Vapor Deposition," Appl. Phys. Lett., 75 (1999) 4159.

[87] L.T. Romano, J.E. Northrup, A.J. Ptak, and T.H. Myers, "Faceted Inversion Domain Boundary in GaN Films Doped with Mg," Appl. Phys. Lett., 77 (2000) 2479.

[88] V. Darakchieva, T. Hofmann. M. Schubert, B. Monemar, H. Lu, W.J. Schaff, C.-L. Hsiao, T.-W. Liu, L.-C. Chen, D. Muto, and Y. Nanishi, "New Insight into the Free Carrier Properties of InN," Conference Proceedings of the International Workshop on Nitride Semiconductors, Montreux, Switzerland, October 2008.

[89] W. Gotz, N.M. Johnson, J. Walker, D.P. Bour, and R. A. Street, "Activation of Acceptors in Mg-doped GaN Grown by Metalorganic Chemical vapor Deposition," Appl. Phys. Lett. 68 (1996) 667.

[90] T.D. Moustakas and R.J. Molnar, "Growth and Doping of GaN Films by ECR-assisted MBE," Mat. Res. Soc. Symp. Proc., 281 (1993) 753.

[91] W. Kim, A. Salvador, A.E. Botchkarev, O. Aktas, S.N. Mohammad, and H. Morcoc, "Mg-doped p-type GaN Grown by Molecular Beam Epitaxy," Appl. Phys. Lett. 69 (1996) 559.

[92] S. D. Burnham, W. A. Doolittle, G. Namkoong, and W. Henderson, "Mg Doped GaN Using a Valved, Thermally Energetic Source: Enhanced Incorporation, Control and Quantitative Optimization," Materials Research Society proceeding, 798 (2003) 479.

[93] S. D. Burnham and W. A. Doolittle, "*In situ* Growth Regime Characterization of AlN Using Reflection High Energy Electron Diffraction," J. of Vacuum Science & Technology B, 24 (2006) 2100.

[94] S. D. Burnham, G. Namkoong, K.-K. Lee, and W. A. Doolittle, "Reproducible Reflection High Energy Electron Energy Diffraction Signatures for Improvement of AlN Using *in situ* Growth Regime Characterization," J. Vac. Sci. and Tech. B, 25 (2007) 1009.

[95] B. Heying, R. Averbeck, L.F. Chen, E. Haus, H. Riechert, and J.S. Speck, "Control of GaN Surface Morphologies Using Plasma-Assisted Molecular Beam Epitaxy," J. Appl. Phys. 88 (2000) 1856.

[96] A. Bhatacharyya, W.Li, J.Cabalu, T.D. Moustakas, D.J. Smith, and R.L. Hervig, "Efficient p-type Doping of GaN Films by Plasma-Assisted Molecular Beam Epitaxy," Appl. Phys. Lett., 85 (2004) 4956.

[97] M. McLaurin, T.E. Mates, F. Wu, and J.S. Speck, "Molecular-beam Epitaxy of p-type m-plane GaN," J. Appl. Phys., 100 (2006) 063707.

[98] J. Simon and D. Jena, "Effect of Growth Conditions on the Conductivity of Mg Doped p-type GaN by Molecular Beam Epitaxy," Phys. Stat. Sol. A, 5 (2008) 1074.

[99] S.D. Burnham, "Improved Understanding and Control of Magnesium-Doped Gallium Nitride by Plasma Assisted Molecular Beam Epitaxy," PhD. Thesis, Georgia Institute of Technology, 2007.

[100] S.D. Burnham, G. Namkoong, W. Henderson, and W.A. Doolittle, "Mg Doped GaN Using a Valved, Thermally Energetic Source: Enhanced Incorporation, and Control," J. Crystal Growth, 279 (2005) 26.

[101] Y. Ohba and A. Hatano, "A Study on Strong Memory Effects for Mg Doping in GaN Metalorganic Chemical Vapor Deposition," J. Crystal Growth, 145 (1994) 214.

[102] G. Namkoong, E. Trybus, K.K. Lee, M. Moseley, W.A. Doolittle and, D.C. Look, "Metal Modulation Epitaxy Growth for Extremely High Hole Concentrations Above 10^{19} cm^{-3} in GaN," Appl. Phys. Lett., 93 (2008) 172112.

[103] E. Trybus, W.A. Doolittle, M. Moseley, W. Henderson, D. Billingsley, G. Namkoong, and D.C. Look, "Extremely High Hole Concentrations in c-Plane GaN," Conference Proceedings of the International Workshop on Nitride Semiconductors, Montreux, Switzerland, October 2008. Accepted for publication in Phys. Stat. Sol C.

[104] H.M. Ng, D. Doppalapudi, D. Korakakis, R. Singh, and T.D. Moustakas, "MBE Growth and Doping of III-V Nitrides," J. Cryst. Growth, 189/190 (1998) 349.

[105] C.S. Gallinat, G. Koblmuller, J.S. Brown, and J.S. Speck, "A Growth Diagram for Plasma-Assisted Molecular Beam Epitaxy of In-face InN," J. Appl. Phys., 102 (2007) 064907.

[106] T.L. Tansley and R.J. Egan, "Optical and Electronic Properties of the Nitrides of Indium, Gallium, and Aluminum and the Influence of Native Defects," Wide Band Gap Semi. Symp. (1992) 395.

[107] H.Lu, W.J. Schaff, L.F. Eastman, and C.E. Stutz, "Surface Charge Accumulation of InN Grown by Molecular-Beam Epitaxy," Appl. Phys. Lett., 82 (2003) 1736.

[108] T.D. Veal, P.H. Jefferson, L.F.J. Piper, C.F. McConville, T.B. Joyce, P.R. Chalker, L. Considine, H. Lu, and W.J. Schaff, "Transition From Electron Accumulation to Depletion at InGaN Surfaces," Appl. Phys. Lett., 89 (2006) 202110.

[109] H.P. Gillis, J.L. Clemons, and J.P. Chamberlain, "Low-Energy Electron Beam Enhanced Etching of Si(100)-(2×1)," J. Vac. Sci. Technol. B 10(6) (1992) 2729.

[110] H.P. Gillis, M.B. Christopher, K.P. Martin, and D.A. Choutov, "Patterning III-N Semiconductors by Low Energy Electron Enhanced Etching (LE4)," MRS Internet J. Nitride Semicond. Res. 4S1 (1999) G8.2.

[111] T. Yamguchi, D. Muto, T. Araki, N. Maeda, and Y. Nanishi, "Novel InN Growth Method Under In-rich Conditions on GaN/Al2O3 (0001) Templates," Conference Proceedings of the International Workshop on Nitride Semiconductors, Montreux, Switzerland, October 2008.

[112] P. Kozodoy, M. Hansen, S.P. DenBaars, and U.K. Mishra, "Enhanced Mg Doping Efficiency in $Al_{0.2}Ga_{0.8}N$ Superlattices," Appl. Phys. Lett, 74 (1999) 3681.

[113] J.K. Sheu, J.M. Tsai, S.C. Shei, W.C. Lai, T.C. Wen, C.H. Kou, Y.K. Su, S.J. Chang, and G.C. Chi, "Low-Operation Voltage of InGaN/GaN Light-Emitting Diodes With Si-Doped $In_{0.3}Ga_{0.7}N$/GaN Short-Period Superlattice Tunneling Contact Layer," IEEE Electron Device Lett., 22 (2001) 460.

[114] Semiconductor Technology Research, Inc. downloaded from http://www.semitech.us/products/SiLENSe/ on November 7, 2008.

[115] R.J. Shul, L. Zhang, C.G. Willison, J. Han, S.J. Pearton, J. Hong, C.R. Abernathy, and L.F. Lester, "Group-III Nitride Etch Selectivity in BCl3/Cl_2 ICP Plasmas," MRS Internet J. Nitride Semicond. Res. 4S1, G8.1 (1999).

[116] K.P. Pande, Y-S. Hsu, J.M. Borrego, S.K. Ghandhi, "Grain-Boundary Edge Passivation of GaAs Films by Selective Anodization," Appl. Phys. Lett. 33 (1978) 717.

[117] D.K. Schroder, *Semiconductor Material and Device Characterization*, John Wiley & Sons, Inc., (2006).

[118] J.M. DeLucca, H.S. Venugopalan, S.E. Mohney, and R.F. Karlicek, Jr., "Ohmic Contacts Fromed by Electrodeposition and Physical Vapor Deposition on p-GaN," Appl. Phys. Lett., 73 (1998) 3402.

[119] M.A. Green, *Solar Cells – Operating Principles*, Addison-Wesley Publishing Company, Inc., (1996).

[120] Keithley Instruments Inc. Application Note, "#2876 Making I-V and C-V Measurements on Solar/Photovoltaic Cells Using the Model 4200-SCS Semiconductor Characterization System" (2007).

[121] E.W. McFarland and J. Tang, "A Photovoltaic Device Structure Based on Internal Electron Emission," Nature, 421 (2003) 616.

[122] Royal Society of Chemistry, downloaded from http://www.rsc.org/ej/JM/2003/b212621d/b212621d-f6.gif on January 15, 2008.

[123] G. Namkoong, "Molecular Beam Epitaxy Grown III-Nitride Materials for High-Power and High-Temperature Applications: Impact of Nucleation Kinetics on Material and Device Structure Quality," PhD. Thesis, Georgia Institute of Technology, 2003.

VITA

Elaissa Lee Trybus was born in Albuquerque, New Mexico. She graduated from the University of New Mexico in May 2002 with her Bachelor of Science in Electrical Engineering. While attending UNM, Elaissa was a four year member of the varsity Women's swimming and diving team. She was an academic All-American collegiate scholar.

In May of 2004, she received her Master of Science in Electrical and Computer Engineering from Georgia Institute of Technology. She plans to receive her Ph.D degree in May 2009 under the supervision of Dr. W. Alan Doolittle.

Elaissa is an avid reader and while at Georgia Tech she has read over 177 fiction novels, including 24 Pulitzer Prize winning fiction novels. She also is a long time fan of the 2008 Stanley Cup Champions, the Detroit Red Wings.

Referred Journals and Proceedings

- **Elaissa Trybus**, W. Alan Doolittle, Michael Moseley, Walter Henderson, Daniel Billingsley, Gon Namkoong, and David C. Look, "Extremely High Hole Concentrations in c-Plane GaN," Conference Proceedings of the International Workshop on Nitride Semiconductors, Montreux, Switzerland, October 2008.

- Gon Namkoong, **Elaissa Trybus**, Kyoung Keun Lee, Michael Moseley, W. Alan Doolittle, and David C. Look, "Metal Modulation Epitaxy Growth for Extremely High Hole Concentrations Above 10^{19} cm^{-3} in GaN," Applied Physics Letters 93, 172112 (2008).

- **Elaissa Trybus**, Gon Namkoong, Walter Henderson, W. Alan Doolittle, "Systematic Study of High Hole Concentration, Low Temperature Grown Mg-doped GaN," Submitted for peer review September 2008.

- **Elaissa Trybus**, Omkar Jani, Shawn Burnham, Ian Ferguson, Christiana Honsberg, Myles Steiner, and W. Alan Doolittle, "Characteristics of InGaN Designed for Photovoltaic Applications," Conference Proceedings of the 7^{th} International Conference of Nitride Semiconductors, Las Vegas, Nevada, No. 6, pp 1843, Physica Status Solidi C, (2008).

- Omkar Jani, Hongbo Yu, **Elaissa Trybus**, Balakrishnam Jampana, Ian Ferguson, W. Alan Doolittle, and Christiana Honsberg, " Effect of Phase Separation on

Performance of III-V Nitride Solar Cells," Conference Proceedings of the 22nd European Photovoltaic Solar Energy Conference, Milan, Italy, 2007.

- **Elaissa Trybus**, Walter Henderson, Gon Namkoong, and W. Alan Doolittle, "Observation of Cubic Phase Development of Mg-doped InGaN by Molecular Beam Epitaxy," Submitted for peer review September 2007.

- Gon Namkoong, **Elaissa Trybus**, Will Fenwick, Ian Ferguson, W. Alan Doolittle, and Jeff Nause, "Heterojunction p-GaN/InGaN/n-ZnO Light Emitting Diodes using ZnO substrates," Submitted to Applied Physics Letters 2007.

- Omkar Jani, Christiana Honsberg, Yong Huang, June-O Song, Ian Ferguson, Gon Namkoong, **Elaissa Trybus**, Alan Doolittle, Sarah Kurtz, " Design, Growth, Fabrication and Characterization of High-Band Gap InGaN/GaN Solar Cells," IEEE 4th World Conference on Photovoltaic Energy Conversion, Waikoloa, Hawaii, May 7-12, 2006.

- **Elaissa Trybus**, Gon Namkoong, Walter Henderson, Shawn Burnham, W. Alan Doolittle, Maurice Cheung, and Alexander Cartwright, "InN: A material with Photovoltaic Promise and Challenges," vol 288, pp 218, *Journal of Crystal Growth* (2005).

- Christiana Honsberg, Omkar Jani, **Elaissa Trybus**, W. Alan Doolittle, and Ian Ferguson, "Novel High-Efficiency PV Devices based on III-V Nitride Material Systems," Proceeding of the Department of Energy Solar Energy Technologies Program Review, Denver, Colorado, November 7-10, 2005.

- **Elaissa Trybus**, Gon Namkoong, Walter Henderson, W. Alan Doolittle, Rong Liu, Jin Mei, Fernando Ponce, Maurice Cheung, Fei Chen, Madalina Furis, and Alexander Cartwright, "Growth of InN on Ge Substrate by Molecular Beam Epitaxy," vol 279, pp 311, *Journal of Crystal Growth* (2005).

- Gon Namkoong, Shawn Burnham, Kyoung-Keun Lee, **Elaissa Trybus**, W.Alan Doolittle, Maria Losurdo, Pio Capezzuto, Giovanni Bruno, Bill Nemeth, and Jeff Nause, "III-nitrides on oxygen- and zinc-face ZnO substrates," vol 87, pp 184104, *Applied Physics Letters* (2005).

- Christiana Honsberg, Omkar Jani, W. Alan Doolittle, **Elaissa Trybus**, and Ian Ferguson, "InGaN Solar Cells," Proceedings of the Department of Energy Solar Energy Technologies Program Review, Denver, Colorado, October 25-28, 2004, pp 87.

- Christiana Honsberg, Omkar Jani, W. Alan Doolittle, **Elaissa Trybus**, Gon Namkoong, Ian Ferguson, David Nicole, and Adam Payne Journal article titled "InGaN - A New Photovoltaic Material," pending *19th European Photovoltaic Solar Energy Conference*, Paris, 2004.

Conference Presentations

- W. Alan Doolittle, Gon Namkoong, **Elaissa Trybus**, David C. Look, Walter Henderson, and Tae-Yeon Seong, "Extremely High Hole Concentrations in C-Plane GaN," International Workshop on Nitride Semiconductors, Montreux, Switzerland, October 2008.

- Gon Namkoong, **Elaissa Trybus**, W. Alan Doolittle, David C. Look, and Tae-Yeon Seong," Growth and Characterization of GaN with Extremely High Hole Concentration," 214th Electrochemical Society Conference, Honolulu, Hi, October 2008.

- **Elaissa Trybus,** Shawn Burnham, Gon Namkoong, David C. Look, Daniel Billingsley, Michael Moseley, Walter Henderson, and W. Alan Doolittle, "Systematic Study of High Hole Concentration, Low Temperature Grown GaN Approaching the Compensated Region," 50th Electronic Materials Conference, Santa Barbara, CA, June 2008.

- **Elaissa Trybus**, Omkar Jani, Shawn Burnham, Ian Ferguson, Christiana Honsberg, Myles Steiner, and W. Alan Doolittle, "Characteristics of InGaN Designed for Photovoltaic Applications," 7th International Conference of Nitride Semiconductors, Las Vegas, Nevada, September 2007.

- **Elaissa Trybus**, Gon Namkoong, Walter Henderson, W. Alan Doolittle, "Interesting Anomaly in InGaN Growth by Molecular Beam Epitaxy," *Workshop on Compound Semiconductor Materials and Devices*, Savannah, GA, February 2007.

- Daniel Billingsley, David Pritchett, Walter Henderson, **Elaissa Trybus**, Kyoung Keun Lee, and W. Alan Doolittle, "Influence of Surface Nitridation on Gallium Nitride Grown via Ammonia based Metal Organic Molecular Beam Epitaxy," North American Molecular Beam Epitaxy Conference, Durham, NC, October 2006.

- **Elaissa Trybus,** Gon Namkoong, Walter Henderson, Alexander Carver, W. Alan Doolittle, and H.J. Lee, "High-Energy Electron Beam Interactions with Indium Nitride During Growth via MBE," 33rd Conference on the Physics and Chemistry of Semiconductor Interfaces, Cocoa Beach , FL, January 2006.

- **Elaissa Trybus**, W. Alan Doolittle, Walter Henderson, Gon Namkoong, Shawn Burnham, Kyoung Keun Lee, Ian Ferguson, and Christiana Honsberg, "InN: Revolutionary Photovoltaic Material or Just a Revolting Material," *Workshop on Compound Semiconductor Materials and Devices*, Miami, FL, February 2005.